

1982

## Anisotropy in MHD turbulence due to a mean magnetic field

John V. Shebalin

*College of William & Mary - Arts & Sciences*

Follow this and additional works at: <https://scholarworks.wm.edu/etd>



Part of the [Plasma and Beam Physics Commons](#)

---

### Recommended Citation

Shebalin, John V., "Anisotropy in MHD turbulence due to a mean magnetic field" (1982). *Dissertations, Theses, and Masters Projects*. William & Mary. Paper 1539623736.  
<https://dx.doi.org/doi:10.21220/s2-p21x-9v37>

This Dissertation is brought to you for free and open access by the Theses, Dissertations, & Master Projects at W&M ScholarWorks. It has been accepted for inclusion in Dissertations, Theses, and Masters Projects by an authorized administrator of W&M ScholarWorks. For more information, please contact [scholarworks@wm.edu](mailto:scholarworks@wm.edu).

## INFORMATION TO USERS

This reproduction was made from a copy of a document sent to us for microfilming. While the most advanced technology has been used to photograph and reproduce this document, the quality of the reproduction is heavily dependent upon the quality of the material submitted.

The following explanation of techniques is provided to help clarify markings or notations which may appear on this reproduction.

1. The sign or "target" for pages apparently lacking from the document photographed is "Missing Page(s)". If it was possible to obtain the missing page(s) or section, they are spliced into the film along with adjacent pages. This may have necessitated cutting through an image and duplicating adjacent pages to assure complete continuity.
2. When an image on the film is obliterated with a round black mark, it is an indication of either blurred copy because of movement during exposure, duplicate copy, or copyrighted materials that should not have been filmed. For blurred pages, a good image of the page can be found in the adjacent frame. If copyrighted materials were deleted, a target note will appear listing the pages in the adjacent frame.
3. When a map, drawing or chart, etc., is part of the material being photographed, a definite method of "sectioning" the material has been followed. It is customary to begin filming at the upper left hand corner of a large sheet and to continue from left to right in equal sections with small overlaps. If necessary, sectioning is continued again—beginning below the first row and continuing on until complete.
4. For illustrations that cannot be satisfactorily reproduced by xerographic means, photographic prints can be purchased at additional cost and inserted into your xerographic copy. These prints are available upon request from the Dissertations Customer Services Department.
5. Some pages in any document may have indistinct print. In all cases the best available copy has been filmed.

**University  
Microfilms  
International**

300 N. Zeeb Road  
Ann Arbor, MI 48106



8307096

**Shebalin, John Valentine**

**ANISOTROPY IN MHD TURBULENCE DUE TO A MEAN MAGNETIC  
FIELD**

*The College of William and Mary in Virginia*

**Ph.D. 1982**

**University  
Microfilms  
International** 300 N. Zeeb Road, Ann Arbor, MI 48106



**PLEASE NOTE:**

In all cases this material has been filmed in the best possible way from the available copy.  
Problems encountered with this document have been identified here with a check mark ✓.

1. Glossy photographs or pages \_\_\_\_\_
2. Colored illustrations, paper or print \_\_\_\_\_
3. Photographs with dark background \_\_\_\_\_
4. Illustrations are poor copy \_\_\_\_\_
5. Pages with black marks, not original copy \_\_\_\_\_
6. Print shows through as there is text on both sides of page \_\_\_\_\_
7. Indistinct, broken or small print on several pages ✓
8. Print exceeds margin requirements \_\_\_\_\_
9. Tightly bound copy with print lost in spine \_\_\_\_\_
10. Computer printout pages with indistinct print \_\_\_\_\_
11. Page(s) \_\_\_\_\_ lacking when material received, and not available from school or author.
12. Page(s) \_\_\_\_\_ seem to be missing in numbering only as text follows.
13. Two pages numbered \_\_\_\_\_. Text follows.
14. Curling and wrinkled pages \_\_\_\_\_
15. Other \_\_\_\_\_

**University  
Microfilms  
International**



ANISOTROPY IN MHD TURBULENCE  
DUE TO A MEAN MAGNETIC FIELD

---

A Dissertation Presented to  
The Faculty of the Department of Physics  
The College of William and Mary in Virginia

---

In Partial Fulfillment  
of the Requirements for the Degree of  
Doctor of Philosophy

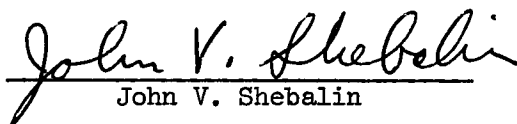
---

by  
John V. Shebalin  
October 1982

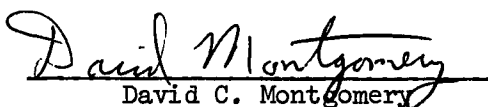


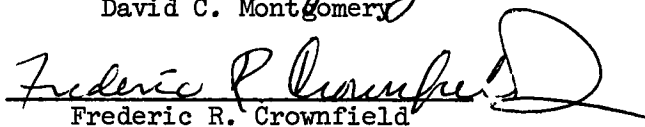
APPROVAL SHEET

This dissertation is submitted in  
partial fulfillment of the requirements  
for the degree of  
Doctor of Philosophy

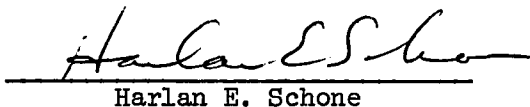
  
John V. Shebalin

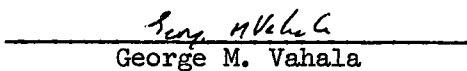
Approved, October 1982

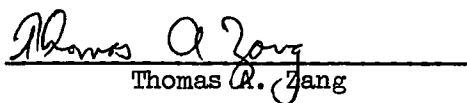
  
David C. Montgomery

  
Frederic R. Crownfield

  
William H. Matthaeus

  
Harlan E. Schone

  
George M. Vahala

  
Thomas A. Zang

## TABLE OF CONTENTS

	Page
ACKNOWLEDGEMENTS . . . . .	iv
ABSTRACT . . . . .	v
I. INTRODUCTION . . . . .	2
II. HISTORICAL SKETCH . . . . .	5
III. EXPERIMENTAL RESULTS . . . . .	10
IV. PRELIMINARY THEORETICAL AND NUMERICAL RESULTS . . . .	26
V. DYNAMICAL EQUATIONS . . . . .	30
VI. COMPUTATIONAL TECHNIQUE . . . . .	34
VII. NON-DISSIPATIVE TESTS . . . . .	36
VIII. APPEARANCE OF ANISOTROPY: EFFECTS OF VISCOSITY, RESISTIVITY AND SPATIAL RESOLUTION . . . . .	44
IX. EFFECTS OF VARIABLE MEAN FIELD STRENGTH . . . . .	58
X. DISCUSSION . . . . .	64
APPENDIX A: ABSOLUTE EQUILIBRIUM ENSEMBLE THEORY . .	67
APPENDIX B: RANDOMNESS AND ERGODICITY IN MHD MODEL TURBULENT SYSTEMS . . . . .	81
REFERENCES . . . . .	101

#### ACKNOWLEDGEMENTS

I would like to thank David Montgomery and William Matthaeus for their guidance, instruction, encouragement and patience during the course of this research. I am grateful to the Oceanic Division of the Westinghouse Electric Corporation for the computer time they provided. I wish to dedicate this work to my wife, Marcia, who shared in my hopes and frustrations during its completion.

## ABSTRACT

The development of anisotropy in an initially isotropic spectrum is studied numerically for two-dimensional magnetohydrodynamic (MHD) turbulence. The anisotropy develops due to the combined effects of an externally imposed dc magnetic field and viscous and resistive dissipation at high wave numbers. The effect is most pronounced at high mechanical and magnetic Reynolds numbers. The anisotropy is greater at the higher wave numbers.

The statistical structure of two-dimensional MHD turbulence is also considered. It is shown that the three known rugged invariants of the isotropic case reduce to two for the anisotropic case. Randomness and ergodicity are also briefly discussed.

ANISOTROPY IN MHD TURBULENCE  
DUE TO A MEAN MAGNETIC FIELD

## I. INTRODUCTION

In the last few decades a systematic theory of magnetohydrodynamic (MHD) turbulence has emerged. This theory has addressed itself to understanding the incoherent, non-linear, random fluctuations of the velocity and magnetic fields (i.e., MHD turbulence) associated with a highly agitated magnetofluid (a magnetofluid being a fluid with a relatively large electrical conductivity, which allows for the existence of electric currents and their corresponding magnetic fields). This theory has become, in view of the random nature of MHD turbulence, largely a statistical one.

The statistical theory of MHD turbulence has primarily been developed utilizing certain symmetry assumptions about the statistics of the fluctuating vector fields, such as isotropy, homogeneity and stationarity. Although these assumptions have proven very useful and lead to a much-reduced mathematical description, we note that in many physical systems MHD turbulence takes place in the presence of an externally imposed mean magnetic field. Since this mean magnetic field cannot be removed by a coordinate transformation (as can a mean velocity field) it is clear that a mean magnetic field introduces an anisotropy, or preferred direction, into the description of the physical system.

In the present work, the structure of MHD turbulence in the presence of the anisotropy induced by a mean dc magnetic field is investigated. Specifically, the time evolution of the turbulent magnetic and

velocity fields of a two-dimensional magneto-fluid is determined numerically, using an incompressible, spectral method MHD code. This procedure yields a recorded time history of the evolving magnetic and velocity fields, allowing diagnostic analyses to be performed which illuminate the nature of anisotropic MHD turbulence. The details and results of this analysis will be discussed in the following chapters.

It would have been preferable to have studied anisotropic MHD turbulence with a three dimensional code rather than a two dimensional one. However, the amount of computing power necessary for such an endeavor is generally not available (because of resource scarcity and expense, and current technological limitations). It will be seen, nevertheless, in comparison with pertinent experimental results, that a two-dimensional model of anisotropic MHD turbulence contains many of the features which appear to be central to the three dimensional case.

The two-dimensional numerical simulations were performed on a Digital Equipment Corporation VAX 11/780, time on which was generously provided by the Oceanic Division, Westinghouse Electric Corporation (at Annapolis, Maryland). The VAX is a virtual-memory machine very similar to the IBM 370/158; benchmark tests have shown that the two-dimensional code used here runs only 9% slower on the VAX than on the IBM 370. For the purposes of the research related to this dissertation, a total of about 600 VAX cpu hours were utilized.

The outline of this work is as follows. In the second chapter a brief historical sketch will be given, in order to provide the context

in which this work is imbedded. In the third chapter, the pertinent experimental papers will be discussed, while in the fourth chapter, important preliminary theoretical and numerical papers will be discussed. The next half dozen chapters will address the current numerical results and will be followed by a concluding chapter. Finally, there will be two appendices on the statistical theory associated with two-dimensional anisotropic MHD turbulence.



## II. HISTORICAL SKETCH

Magnetohydrodynamics and plasma physics, though less than a century old, have had an interesting history, which has been recorded, to various extents, by numerous authors. Two sources of particular note are to be found in the book of Ferraro and Plumpton (1966), Magneto-Fluid Mechanics, and in the article by C. J. H. Watson (1972), "Introduction to Plasma Physics," which appears in Plasma Physics, a collection of articles derived from the Culham Summer School lectures. Another text which is also useful is An Introduction to Plasma Physics, by W. B. Thompson (1962). It is primarily from these sources that the following historical sketch has been drawn.

Although the basic physical principles (and their mathematical expressions) had existed before J. C. Maxwell formulated his equations of electrodynamics, the impetus which gave rise to MHD seems to have occurred around the beginning of the 20th century. In 1899 Bigelow saw in the shapes of coronal plumes a similarity to the structure of the lines of force around a uniformly magnetized sphere. This led him to conjecture that the sun was a giant magnet; Schuster then expanded upon this idea to suggest that every large celestial body was a great magnet. It appears that these speculations may have led the astronomer Hale to look for solar magnetic fields; indeed, in 1908, Hale discovered, through the Zeeman effect, that magnetic fields of several thousand gauss were associated with sun spots. For the first time a celestial body other

than the earth (and a gaseous one at that) had been found to possess a magnetic field.

This discovery led Larmor, in the next few years, to put forth a theory which explained the existence and stability of sun spot magnetic fields in terms of a highly conducting fluid (the solar gas) moving across an initially weak magnetic field and dynamically creating a local, intense and long lived magnetic field. Although the details of Larmor's theory were shown by Cowling in 1934 to be somewhat erroneous, the idea of a self-sustaining "dynamo" proved very useful. Particularly important was the combination of fluid mechanics and electrodynamics to attempt to explain a novel physical phenomena; the field of magnetohydrodynamics was beginning to take form and gain substance.

Concurrent with these theories concerning astrophysical phenomena, laboratory experiments with highly conducting fluids were being conducted. In 1928, Irving Langmuir was working with arc discharge tubes, and invented the term "plasma" to describe the ionized gas he observed in the discharge tube. Although Watson (1972) states, "[Langmuir] called it a 'plasma' because of a fancied resemblance between impurity ions in a plasma and white corpuscles in a blood plasma, an analogy which seems rather far-fetched today," Tonks and Langmuir (1929) give a different origin.

In experimenting with a low pressure mercury arc discharge, Tonks and Langmuir (1929) observed what they called "Plasma-electron oscillations". When the electrons oscillate, the positive ions behave like a rigid jelly with uniform density of positive charge  $n_e$ . Imbedded in this jelly and free to move there is an initially uniform electron

distribution... The word 'plasma' will be used to designate that portion of an arc-type discharge in which the densities of ions and electrons are high but substantially equal." (The Greek work plasma means "something molded or formed," according to the standard dictionary definition.)

In this time period, and in the following decades, there was much theoretical and experimental work begun in plasma physics and MHD. In astrophysics, contributions were made by international researchers such as Alfven, Lundquist, Chandrasekhar, Cowling and others. Among those who performed laboratory experiments were Hartmann and Lehnert, while the plasma pinch effect was first analyzed by Bennet (1934) and Tonks (1939). The first substantial technological applications of these new disciplines were in ionospheric radio wave propagation and in the design of fluorescent lights and mercury arc rectifiers.

Although the plasma pinch effect was seen in the 1930's, and, even earlier in 1928, Atkinson and Hautermans had suggested thermonuclear reactions in hydrogen at high temperatures as a source of the sun's energy, no one appears to have considered combining these two ideas. It was not until World War II began and large groups of scientists came together to work for military purposes, that these ideas coalesced. Then, during the war and afterwards, there was much classified fusion research.

In the 1950's, as this fusion research expanded, there were a growing number of experimental observations of laboratory plasmas. These plasmas were not well-behaved; in fact, they were seen to develop pinches, detached pinches and many other forms of instability. These instabilities did (and still do) plague fusion research work throughout the world.

In the 1950's, the English joined a growing (and still classified) international plasma fusion research community by performing research on the ZETA device at the Culham laboratory at Harwell. In the late 1950's there was some initial optimism concerning "cheap energy" when the ZETA device began producing relatively large neutron fluxes. It turned out that these neutrons, which were mistaken for those produced by a thermonuclear deuterium reaction, were actually produced "anomalously" by a few deuterons accelerated by plasma instabilities.

These plasma instabilities gave not only the English, but also the rest of the international fusion research community a seemingly impenetrable barrier which they tried for many years to surmount. The principal countries involved in (classified) fusion research at this time - The USA, UK, and USSR - eventually recognized the magnitude of the task and declassified their fusion research efforts. "One consequence of this decision was the rich harvest of papers at the 2nd International Conference on the Peaceful Use of Atomic Energy at Geneva in 1958, which perhaps marks the beginning of modern fusion plasma physics" (Watson (1962)).

These instabilities are still a formidable problem for the development of practical fusion reactors. Researchers are still optimistic (because of the enormous benefits a working fusion reactor would provide for mankind) but there is a general recognition that new surprises and problems may lie waiting in the future.

In addition to toroidal plasma research devices such as ZETA and the Macrotron Tokamak at UCLA (both of which will be discussed in more

detail presently) and many other toroidal machines throughout the world, there are other devices for which an understanding of plasma dynamics and instabilities are critical. These devices, whose complete description is beyond the scope of the present work, include plasma focus devices, laser fusion machines, high speed electric switches, MHD generator and propulsion systems, and (currently classified) charged particle beam weapons and so-called rail guns.

In the two and a half decades since plasma fusion research was declassified there has been an enormous amount of research effort, both theoretical and experimental. In the previous paragraph, many experimental areas were mentioned; theoretically, there has been much work in so-called linear theory, particularly in relation to magnetofluid stability. There has also been a growing effort to understand the non-linear dynamics of magnetofluids (e.g., MHD turbulence). It is along this branch of current plasma theory that we extend our research efforts.

### III. EXPERIMENTAL RESULTS

There seem to be very few published results concerning laboratory measurements of MHD turbulence. The reason, of course, is that one must take local measurements of a plasma in order to determine turbulent effects; the insertion of material probes into a hot plasma usually results in their destruction, however. (The longevity of a material probe depends not only on the temperature of the plasma, but also on its density and length of time the high temperature is maintained. A "hot" plasma could be defined as one where the numerical value  $H = (\text{electron density} \times \text{electron temperature} + \text{ion density} \times \text{ion temperature}) \times (\text{mean length of time at high temperature})$  is above that for which, say, a quartz probe is destroyed. The temperature and density values of various plasmas are shown in Figure 1, which comes from Thompson (1962).)

There are alternatives to the insertion of probes into a plasma: measure local properties remotely by the use of laser doppler velocimeters, perhaps; this concept, unfortunately, is not an advanced enough state of development. Another alternative is to place the probes outside the plasma; this procedure, however, yields only large scale structures (which may be useful for gross instability studies) while obscuring the small scale, turbulent structures of interest here. Another, and currently more viable alternative is to work with a "cool" plasma, so that various probes may be inserted without destruction.

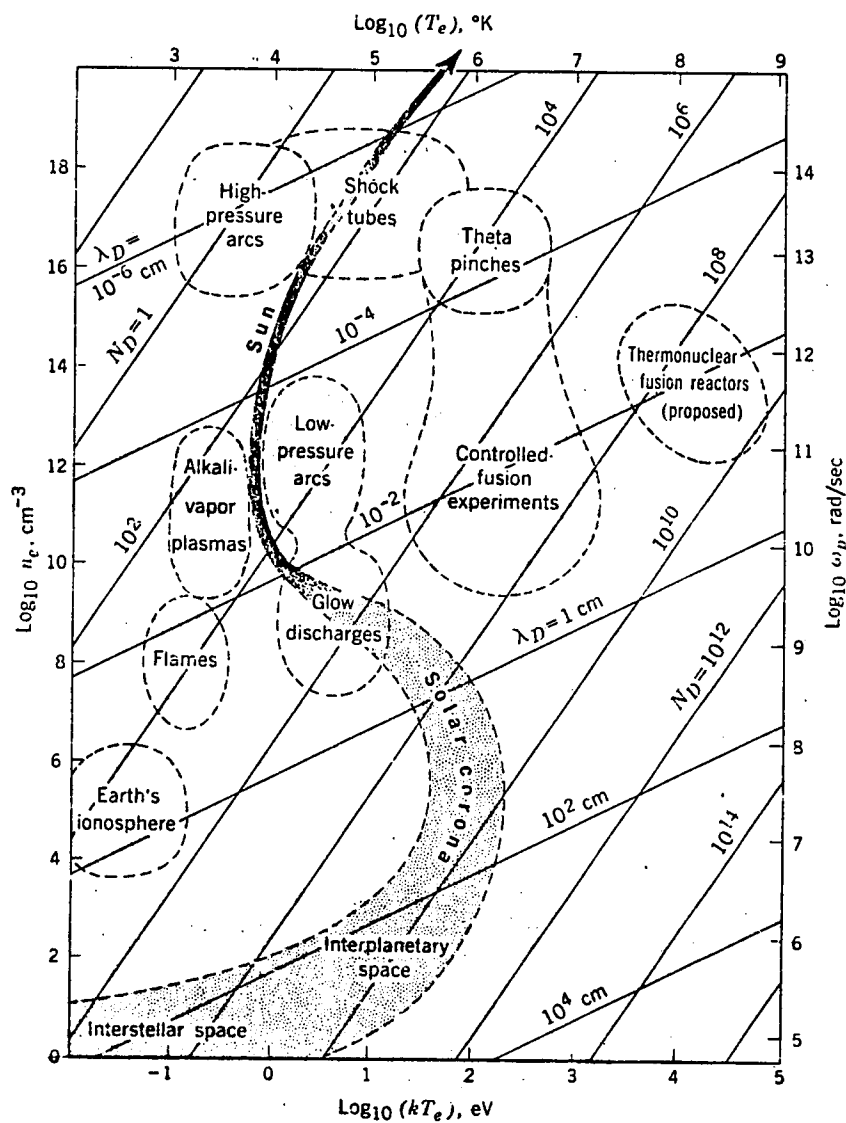


Figure 1.- Various approximate plasma domains; from Thompson (1962).

This last procedure has proved a fruitful one for two groups of researchers upon whose published works we can draw for pertinent experimental results. The first group is from the Culham Laboratory of the United Kingdom Atomic Energy Authority (UKAEA). This group has reported on MHD turbulence measurements on the ZETA Toroidal Z-pinch machine in three principal papers: Robinson, Rusbridge and Saunders (1968), Rusbridge (1969) and Robinson and Rusbridge (1971). The second group has performed experiments on the Macrotron Tokomak at UCLA; their results have been presented in two published articles: Zweben, Menyuk and Taylor (1979) and Zweben and Taylor (1981).

In order to get a better picture as to the nature of these two machines, Figure 2 is a reproduction of a figure from an article by Brickerton and Keen (1972). In this figure, the essential difference between the Zeta mode and Tokomak mode of a toroidal pinch system is illustrated.

#### ZETA Experimental Results

In the experimental measurements on the ZETA device electric and magnetic probes were inserted into a cool plasma (here we will only be concerned with the magnetic probes and their corresponding measurements). Pertinent information related to the experiments performed on ZETA have been drawn directly from the aforementioned papers related to ZETA, and are reproduced in Figures 3 through 6. This information will be drawn on as necessary in the following discussion.

The magnetic field configuration and total current density existing in ZETA during experimental measurements is shown in Figure 3. After an



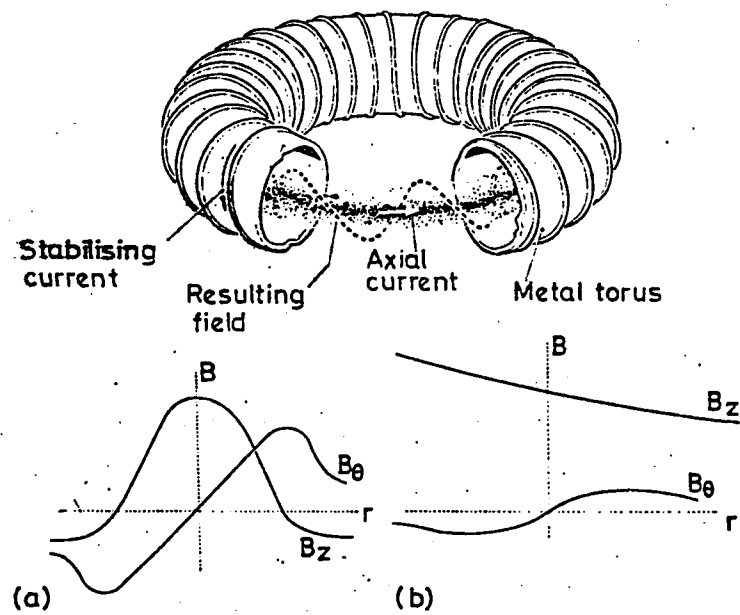
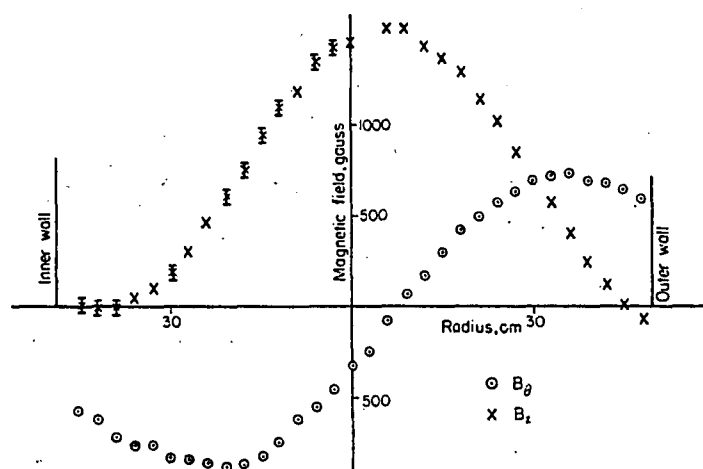
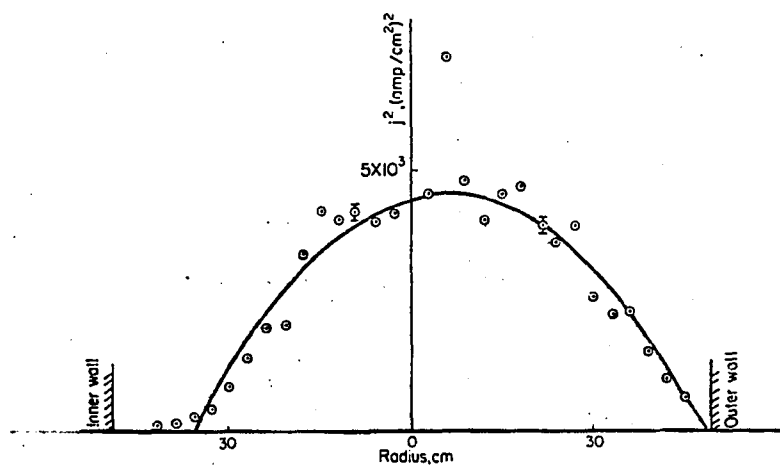


Figure 2.- Toroidal pinch systems: (a) zeta mode, and (b) Tokamak mode; from Brickerton and Keen (1974).



1.—Magnetic field configuration along a horizontal diameter. Gas current 150 kA. initial axial field 370 G, gas pressure 0.5 torr. Except where shown the errors are smaller than the diameters of the points.

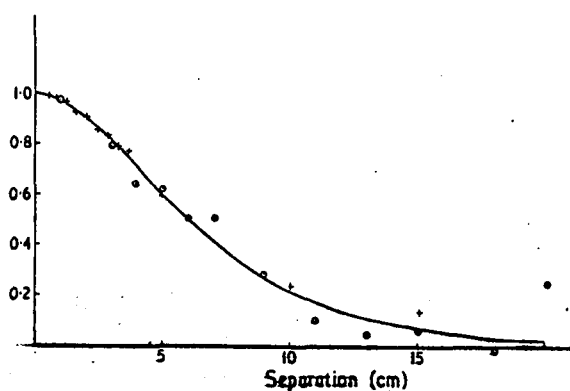


2.—Distribution of the square of the total current density in the horizontal plane. The solid curve is a parabolic form,  $j^2 = j_0^2 \left(1 - \frac{r^2}{r_0^2}\right)$ , centred near the point where  $B_\theta = 0$ .

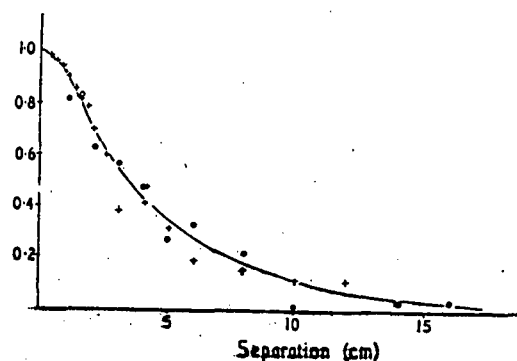
Figure 3.— Magnetic field configuration and current distribution for the ZETA discharge; from Rusbridge (1969).

Summary of experimental parameters.

Initial pressure	0.5 mTorr	5 mTorr
Density	$5 \times 10^{13} \text{ cm}^{-3}$	$4 \times 10^{14} \text{ cm}^{-3}$
Electron temperature	15 eV	6 eV
Mean magnetic field (at the center of the discharge)	1500 G	1500 G
rms turbulent velocity	$10^6 \text{ cm/sec}$	$1.5 \times 10^5 \text{ cm/sec}$
rms magnetic field fluctuations	10 G	4 G
Kinetic energy of velocity fluctuations	42 ergs/cm <sup>3</sup>	7.5 ergs/cm <sup>3</sup>
Ratio of energy in velocity fluctuations to magnetic field fluctuations	10	1.5
Input energy from capacitor bank, 125 KJ	$\sim 1.5 \times 10^5 \text{ ergs/cm}^3$	$\sim 1.5 \times 10^5 \text{ ergs/cm}^3$



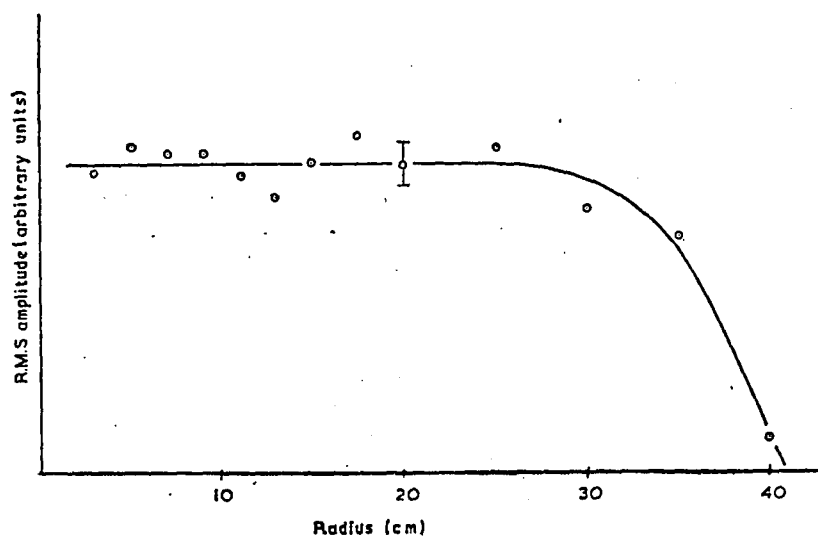
(a)



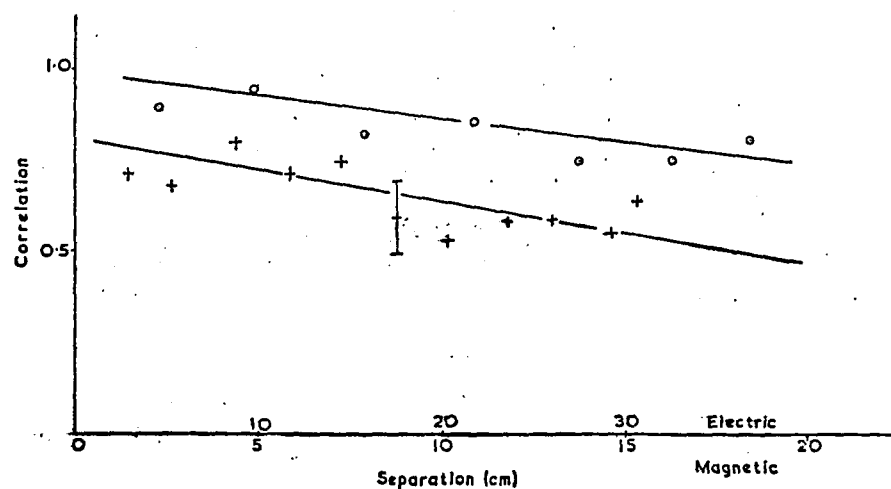
(b)

Correlation function of magnetic-field fluctuations  $\langle b, b, \rangle_r$ ; (a) filling pressure 5-mTorr D<sub>2</sub>; (b) filling pressure 1-mTorr D<sub>2</sub>;  $\circ$  direct measurement,  $+$  derived from structure function measurement. Solid curves represent Eq. (1) with parameters given in Table II. Gas current 150 kA,  $\theta = 1.7$ .

Figure 4.- Experimental parameters and radial correlation function for the ZETA discharge; from Robinson and Rusbridge (1971).



R.M.S. radial magnetic field fluctuations as a function of radius, 0.5 mtorr  $D_2$ ,  
 $I = 150$  kA, applied axial field 290 G.



Magnetic and electric field correlations in the axial direction, ○ magnetic;  
 + electric.

Figure 5.- Radial magnetic field fluctuations and axial field correlations for the ZETA discharge; from Robinson, Rusbridge, and Saunders (1968).

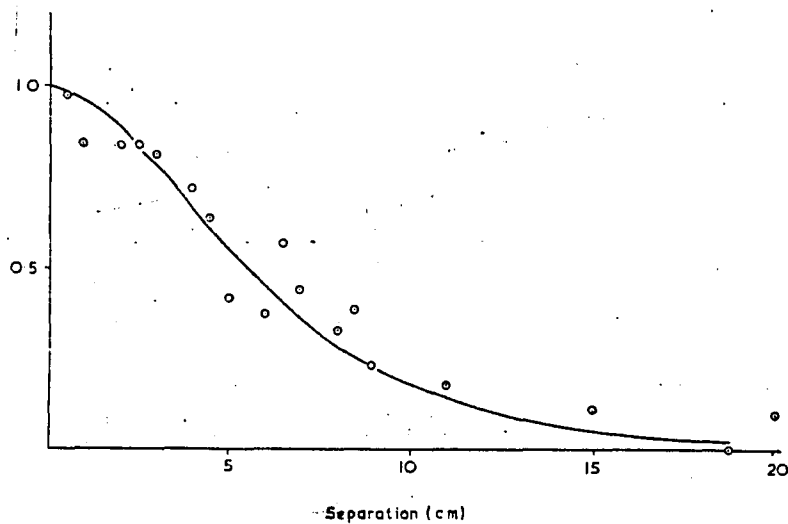


FIG. 3.—Radial magnetic field correlation  $\langle b_r b_r \rangle_r$ ,  $\frac{1}{2}$  mtorr  $D_2$ ,  $I = 150$  kA, applied axial field 370 G, —  $\text{sech}(x/4.2)$ .

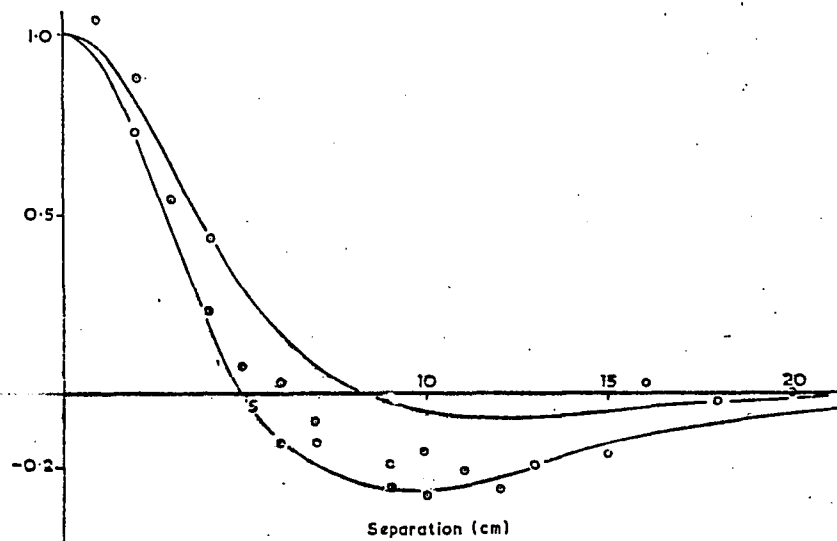


FIG. 4.—Magnetic field correlation  $\langle b_\theta b_\theta \rangle_r$ , 0.5 mtorr  $D_2$ ,  $I = 150$  kA, applied axial field 370 G, upper curve  $f + (r/2)(\partial f / \partial r)$  isotropic, lower  $f + r(\partial f / \partial r)$  two dimensional.

Figure 6.— Radial magnetic field correlations for the ZETA discharge; from Robinson, Rusbridge, and Saunders (1968).

initial concentration of plasma was created in ZETA it was lost to the torus walls in about 0.1 millisecond, while the current pulse lasted for 1-3 millisecc; this current pulse was sustained by reinjecting cold neutral gas. The measurements were thus not taken on a single long-lived concentration of plasma but instead on a sequence ( $\sim 20$ ) of short lived plasma configurations. The recorded measurements came from the central part of these short lifetimes, during which the plasma was in a "quasistationary state". These measurements were then combined and averaged to produce, for example, measures of correlation length of the radial part of the magnetic field, as are shown in Figure 4. In Figure 4 the critical parameters of the ZETA machine are also tabulated.

The measurements of magnetic fields were made by probes inserted into the plasma, at various distances. Since the presence of these probes could possibly affect the measurements, it was necessary to check the results with other modes of measurement to determine if any error was indeed introduced. This was done by comparison with spectroscopic and microwave measurements, with the conclusion that probe perturbation was not a serious problem for ZETA.

The magnetic probes themselves consisted of small pickup coils of 500 turns and 0.5 cm in diameter. Gradient measurements were made with two coaxial coils separated 0.3 to 15 cm apart. The coils were mounted in a quartz envelope 2 meters long, 2.5 cm in diameter, which narrowed to a 1 cm diameter tip. The upper limit on frequency response was 1 MHz and the spatial resolution of measured fluctuations was 1 cm.

The magnetic field measurements on ZETA, as shown in Figures 3 through 6, yield the following observations:

- 1) A fluctuating signal on a reproducible background (background is that part of signal below 7-10 kHz).
- 2) Dominant magnetic field fluctuations at 1-3 kHz correspond to helical distortions of whole current channel and were correlated over the whole discharge.
- 3) Fluctuations above  $\sim 7$  kHz were correlated only over 5-10 cm.
- 4) Necessary signal averaging time was 5 millisec (for a 5% error); needed to average over many discharges ( $\sim 20$ ).
- 5) The high pass filtered fluctuation ( $\sim 10$  Gauss) were constant in magnitude over the central region of the discharge (radius of  $\sim 20$  cm).
- 6) Axial correlation lengths for the turbulent field were  $\approx 60$  cm.

#### Macrotor

The Macrotor device is also a toroidal machine but it is a tokamak, as opposed to ZETA, which is a Z-pinch (see Fig. 2). (The difference in these toroidal pinch systems is illustrated in Figure 2; the essential difference is that the toroidal magnetic field in the Zeta mode is peaked at the center of the toroidal cross-section and reverses sign near the walls, while in the tokamak mode, the toroidal field maintains the same direction throughout the cross-section and is roughly constant.

The poloidal fields in both modes have the same qualitative shape, although the ratio of average toroidal field magnitude to average poloidal field magnitude is greater for the tokamak than the Zeta mode.) Pertinent tabular and graphical information related to magnetic measurements in Macrotor are taken from the aforementioned papers of Zweben and collaborators and presented in Figures 7 and 8.

Other than being run in a tokamak mode, Macrotor is physically very similar to ZETA. The plasma characteristics were slightly different, however. Zeta had a lower electron temperature ( $\sim 10$  eV) than Macrotor ( $\sim 100$  eV) while Macrotor had a lower electron density ( $\sim 4 \times 10^{12} \text{ cm}^{-3}$ ) than ZETA ( $5 \times 10^{13}$  to  $4 \times 10^{14} \text{ cm}^{-3}$ ). The mean axial field in Macrotor ( $\sim 2$  kG) also was higher than that in ZETA ( $\sim 1$  kG).

In Macrotor, glass, rather than quartz tubes, were inserted up to 15 cm into the plasma without damaging the tubes or perturbing the plasma too much. These glass tubes contained magnetic pickup coils, whose construction is shown in Figure 7; checks were also run on these probes to ascertain that the experimental measurements were not unduly affected. The insertion of the probes did not affect the plasma current, voltage, density or ultraviolet light emission in their vicinity. The magnetic spectrum and correlation length was the same when observed with coils inside both 2 cm and 0.5 cm diameter tubes. The presence of a second probe as close as 1 cm away from the first did not affect signals from that probe. Finally, a pair of coils inside a single tube gave the same magnetic structure as did two coils, each in a separate tube. (These checks were done for frequencies less than 100 kHz.)

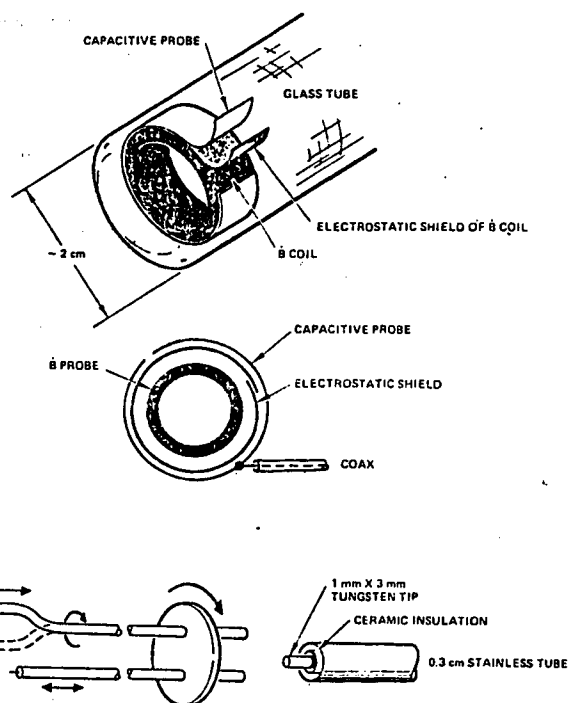


## MACROTOR PARAMETERS

---

$R$	$= 90 \text{ cm}$
$a$	$= 45 \text{ cm (chamber)}$
$I$	$= 60 \text{ kA}$
pulse length $> 50 \text{ ms}$	
$B_T$	$= 2-3 \text{ kG}$
$q(a)$	$= 3-4$
$V_{\text{loop}}$	$= 1-2$
$Z_{\text{eff}}$	$\cong 1$
$T_{e0}$	$\cong 100 \text{ eV}$
$\Gamma_{i0}$	$\cong 50 \text{ eV}$
$n_e$	$\cong 10^{12}-10^{13} \text{ cm}^{-3}$
$\tau_E$	$\cong 0.5-5 \text{ ms (accords with } na^2 \text{ empirical scaling)}$
$\beta_{\text{peak}}$	$= 0.1-1\%$
$\rho_i$	$= 0.3 \text{ cm}$
$\lambda_D$	$= 3 \times 10^{-3} \text{ cm}$
$\lambda_B$	$= c/\omega_p \cong 0.3 \text{ cm}$

---



*Probe construction: The  $B$  coil is 1 cm X 0.3 cm and 20 turns, surrounded by a thin aluminium-foil electrostatic shield which itself is nearly covered by a thin copper (broken) ring electrode of the capacitive probe. The  $B$  signal is differentially amplified X 100, and the capacitive probe signal is monitored with 1 M $\Omega$  to ground by a voltage follower.*

Figure 7.- Macrotor parameters and magnetic probe characteristics; from Zweben and Taylor (1981).

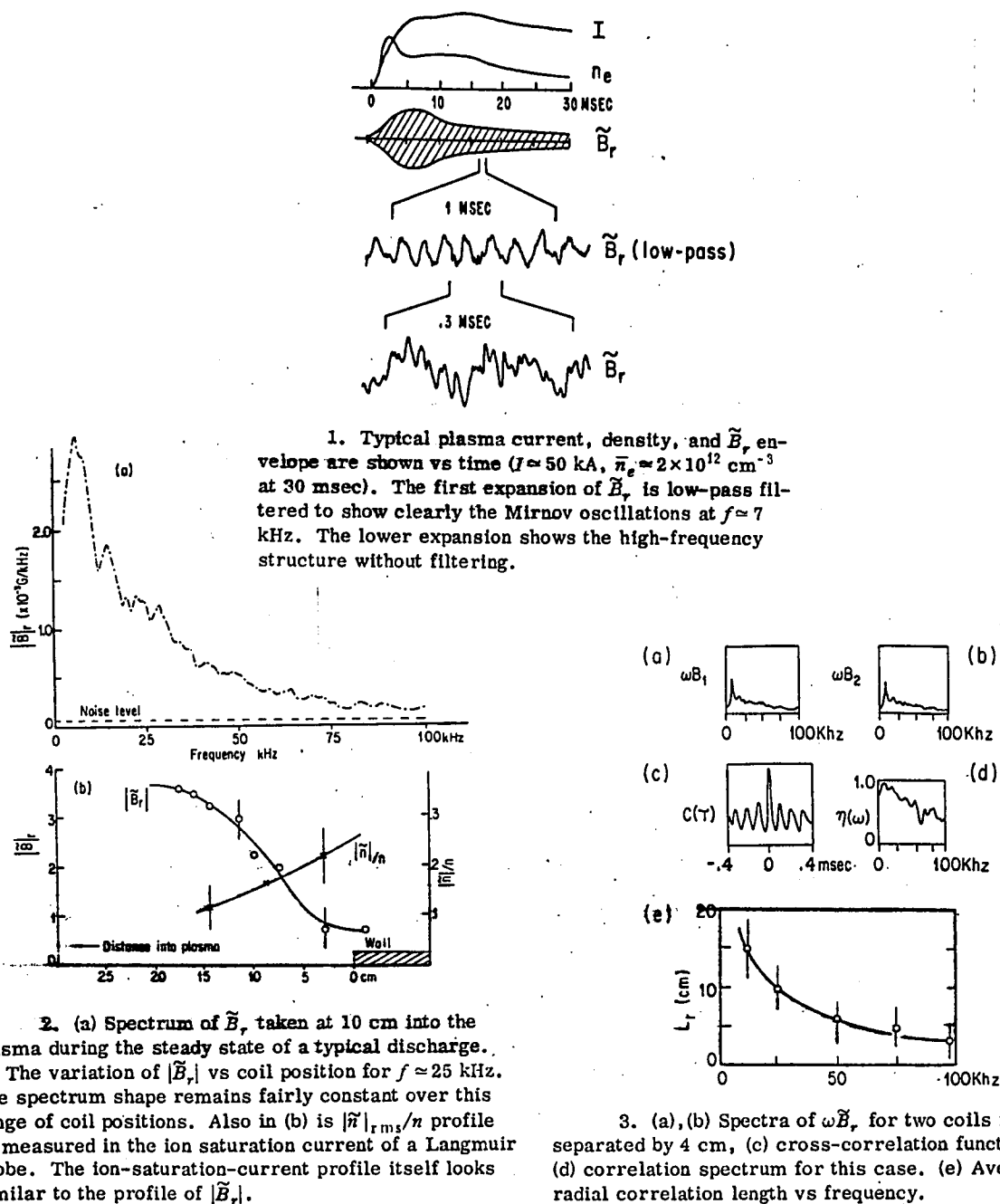


Figure 8.- Typical plasma characteristics and radial magnetic field structure for the Macrotor Tokamak; from Zweben, Menyuk, and Taylor (1979).

In Macrotor, the time-dependence of the radial component of the magnetic field (i.e.,  $\dot{B}_r$ ) was measured by a coil located 10 cm inside the limiting aperture of the torus near the equatorial plane. The signal (similar to that seen in ZETA) was seen to consist of two parts: 1) low frequency ( $\approx 7$  kHz) coherent oscillations (termed "Mirnov oscillations"), and 2) high frequency, broadband, incoherent structure. This signal structure was seen in all Macrotor observations.

The  $B_r$  spectrum shown in Figure 8 was derived from data taken over 15-20 millisec and slide-averaged over  $\sim 3$  kHz. As seen in Figure 8, the spectrum slopes down relatively smoothly from the coherent, energetic low frequency part to the high frequency region, which is broadband with no excessive peaks. (This spectrum was "derived" because what the probes actually measured was  $\dot{B}_r$ , which has a spectrum differing in magnitude from that of  $B_r$  by a factor of  $\omega$ ; the  $|B_r|$  spectrum is thus derived by dividing the  $|\dot{B}_r|$  spectra by  $\omega$ .)

In the Macrotor articles, Zweben, et al., define the cross correlation between two time signals  $S_1(t)$  and  $S_2(t)$  to be

$$C(\tau) \equiv T^{-1} \int_0^T S_1(t) S_2(t-\tau) dt$$

They also define the correlation spectrum to be

$$\eta(\omega) \equiv \langle \eta(\omega) \rangle_{\Delta\omega} = \frac{| \langle F_1^*(\omega) F_2(\omega) \rangle |}{[ \langle F_1^2(\omega) \rangle \langle F_2^2(\omega) \rangle ]^{1/2}}$$

where

$\langle \rangle$  : average over  $\Delta\omega \sim 3$  kHz

$F_1, F_2$  are Fourier transforms of  $S_1, S_2$  .

They then define the correlation length as

$$L : 2 \times \text{coil separation for } \eta(\omega) = 70\%.$$

Using these definitions, Zweben, et al., determine the following results for correlation lengths of the radial part of the magnetic field:

Radial Correlation:

$$L_r(\omega) \lesssim 10 \text{ cm for } \omega > 25 \text{ kHz}$$

Poloidal Correlation:

$$L_p(\omega) \sim L_r(\omega)$$

Toroidal Correlation:

$$L_T(\omega) \gg L_r(\omega) .$$

These results are, though taken from a device operating under a different toroidal mode, consistent with those of the ZETA group.

#### Experimental Result Summary

The basic result of these two sets of experiments is that the turbulent (high frequency) part of the magnetic field associated with a toroidally confined plasma has a correlation length of  $\sim 5$  cm perpendicular to the mean axial field and a longer correlation length of  $\sim 60$  cm parallel to the axial field. In addition, the turbulent spectra were broad band with a notable absence of excessive spikes or peaks. (In fact, the ZETA group described the observed plasma turbulence as occurring in long convective rolls.)

These results are pertinent to the theoretical and numerical investigation to be described in the remaining portion of this dissertation in the following regards. The observed MHD turbulence (the high frequency part of the experimental measurements) is homogeneous, as evidenced by the flatness of the rms turbulent fluctuations in the central part of the discharge; it is (quasi-) stationary, since the results are derived from measurements taken during relatively stationary time segments; and anisotropic, since the turbulence is occurring in the presence of a large mean magnetic field. These three assumptions - homogeneity, stationarity and anisotropy - are central to the analysis that follows.

This analysis is predicated on the assumption that the plasma discharges of Zeta and Macrotor can be modelled in terms of magnetohydrodynamics. This assumption is valid if the processes under observation occur primarily at frequencies considerably lower than the plasma frequency  $\omega_p$ , at length scales considerably longer than the Debye length  $\lambda_D$  and at velocities such that  $(v/c)^2 \ll 1$ . Here,  $\omega_p \approx 10 - 100$  GHz,  $\lambda_D \approx 3$  microns and the rms turbulent velocity fluctuations are  $\sim 10^6$  cm/sec; since the observed frequencies are less than 1 MHz and the spatial resolution is no smaller than 1 cm and  $(v/c)^2 \lesssim 10^{-9} \ll 1$ , the applicability of MHD is strongly indicated.

#### IV. PRELIMINARY THEORETICAL AND NUMERICAL RESULTS

The subject of MHD turbulence, though not as intensely investigated as the linear theory associated with research into the nature and control of plasma instabilities, has still had a long and interesting development. Along with the general upsurge of plasma research that began during and after WWII, came efforts to understand MHD turbulence. These efforts were directed by some, such as Chandrasekhar (1951a), Cowling (1957), Kovasznay (1960) and Tatsumi (1960), to understanding the turbulent plasmas which occur in the astro-and geophysical realm. Others concentrated on MHD turbulence as it appears in plasma fusion machines; many of the results connected with these efforts are contained in the text by Kadomtsev (1965).

The reason for this interest was, of course, the fact that turbulence is the means by which energy is transferred from large length scales to smaller and smaller ones in a plasma or MHD system, finally to wind up as heat. This turbulent decay, with its myriad of large and small "eddies", all interacting with one another, naturally inspired researchers to seek a statistical description. Attempts to understand the statistics of MHD turbulence was begun by many people: Batchelor (1950), Chandrasekhar (1951 a,b) and Kraichnan (1958), among others. These individuals sought to understand the nature of homogeneous, isotropic (and stationary) turbulence. Building on these beginnings, statistical theories concerning

turbulence were formulated by Edwards (1964, 1965), Herring (1965) and especially Kraichnan (1957, 1958, 1964a, 1964b, 1964c, 1965, 1966, 1971a, 1971b, 1972).

Concurrent with the development of isotropic statistical theories of turbulence was the investigation of certain aspects of MHD turbulence in the presence of a mean field. The studies of Lehnert (1955), Moffatt (1961) and Nihoul (1963, 1965) suggested that turbulent motion along the mean field direction would be damped and tend toward a limit of two-dimensional turbulence. These suggestions are, of course, compatible with the experimental observations on ZETA and Macrotor, as discussed in the previous chapter.

Toward the end of the 1960's the development of computers was reaching a point at which they would be sufficiently powerful to allow numerical studies of MHD turbulence to be done. In conjunction with hardware development came software development, i.e., numerical techniques, through which the systematic study of simulated MHD turbulence was finally within grasp. Thus the pioneering work of Orszag (1971) and Patterson and Orszag (1971) and others, resulted in the creation of highly accurate and rapid de-aliased, fast-Fourier transform based "spectral" method techniques.

The code utilized in the numerical studies in the present work is a direct descendant of a code inspired by the work of Orszag. This earlier code (i.e., various versions of it) was used by Fyfe, Joyce and Montgomery (1977 a,b) and Matthaeus and Montgomery (1980, 1981) to study forced dissipative turbulence, selective decay processes, and the evolution

of the sheet pinch (all in the presence of periodic boundary conditions). A similar code was used by Orszag and Tang (1979) to study small scale effects in two dimensions and Pouquet (1978) has published closure calculations for the same geometry. A general review of two-dimensional (isotropic) turbulence has been given by Kraichnan and Montgomery (1980), while details of the numerical procedure can be found in the cited works of Orszag as well as in the Ph.D. dissertation of Matthaeus (1979).

In spite of the large amount of work in MHD turbulence, very little has been done systematically to study such turbulence in the presence of a mean magnetic field. Such an anisotropic situation is assumed to be present, in one form or another, to derive the so-called Strauss equations (Strauss (1976), Montgomery (1982)). These equations are a reduced set of MHD equations (weak dependence in the direction along the mean field) intermediate in dimension between two and three. Although they have found wide applicability to the dynamics of toroidal fusion machines, particularly tokamaks, it is not clear how to proceed in their derivation if a strong anisotropy is not initially present.

This is one of the questions that this work will attempt to answer: does an initially isotropic spectrum evolve into an anisotropic one in the presence of a mean field? It will be shown that for a two-dimensional magnetofluid in the presence of a mean field and dissipation, this does indeed occur. It would have been preferable to have shown this for a fully three dimensional magnetofluid; this, however, was (far) beyond our computational resources, so that the only real alternative was to consider the (non-reduced) dynamics of a two-dimensional magnetofluid.



In the following chapters the results of the present work will be detailed. The dynamical equations will be described and the computational technique discussed briefly. Computational results will then be presented and these will show the development of the strong anisotropy from initially isotropic conditions. These will be seen to correlate well with the ZETA and Macrotor observations.

The dependence of anisotropic development on mean field strength and Reynolds number will then be discussed in the concluding chapter, where a summary of results will be presented. In addition, there are two appendices; in the first, the absolute equilibrium ensemble theory of an anisotropic, homogeneous, stationary (non-dissipative) magnetofluid is given. In the second, the ergodicity and randomness of the MHD model system dynamics are briefly commented on.

## V. DYNAMICAL EQUATIONS

The incompressible, dissipative MHD equations in two dimensions are used. The magnetic field consists of a constant mean field part  $\vec{B}_0 = B_0 \hat{e}_x$ , plus a time-dependent zero-mean turbulent  $\vec{B} = (B_x, B_y, 0) = \nabla x(\hat{e}_z a)$ . The magnetic vector potential is  $\hat{e}_z a(x, y, t)$  so that the Coulomb gauge is employed. For all variables,  $\partial/\partial z \equiv 0$ . The velocity field  $\vec{v} = (v_x, v_y, 0) = \nabla x(\hat{e}_z \psi)$  is expressed in terms of a stream function  $\psi = \psi(x, y, t)$  and has zero mean. In what has become a standard set of dimensionless variables, the vorticity  $\vec{\omega} = \omega \hat{e}_z = \nabla x \vec{v}$ , so that  $\omega = -\nabla^2 \psi$ . Similarly, the electric current  $\vec{j} = j \hat{e}_z$ , with  $\nabla^2 a = -j$ .

Magnetic fields are measured in terms of the initial root mean square turbulent field strength  $B$ . Velocities are measured in units of the Alfvén speed corresponding to  $B$ . The dimensionless viscosity and resistivity  $\nu$  and  $\eta$  are the reciprocals of mechanical and magnetic Reynolds numbers, respectively. The simplest form of the dynamical equations is, in the two-dimensional geometry,

$$\frac{\partial \omega}{\partial t} + \vec{v} \cdot \nabla \omega = \vec{B} \cdot \nabla j + \nu \nabla^2 \omega + \beta_0 \frac{\partial j}{\partial x} \quad (1)$$

and

$$\frac{\partial a}{\partial t} + \vec{v} \cdot \nabla a = \eta \nabla^2 a + \beta_0 \frac{\partial \psi}{\partial x} \quad (2)$$

A brief digression on the origin of (1) and (2) is in order here. For a full, three dimensional treatment, four sets of equations are

required: 1) Maxwell's equations; 2) the equation of magnetofluid motion (extended Navier-Stokes equation); 3) the equation of continuity; 4) the appropriate thermodynamic equations. Let us consider each of these in turn and see how they reduce for the case of two dimensional, incompressible, dissipative flow. (A complete discussion of these equations may be found in Ferraro and Plumpton (1966).)

Maxwell's equations are

$$\begin{aligned}
 (i) \quad \nabla \cdot \vec{D} &= \rho_e & (ii) \quad \nabla \cdot \vec{B} &= 0 \\
 (iii) \quad \nabla \times \vec{H} &= \vec{j} + \frac{\partial \vec{D}}{\partial t} & (iv) \quad \nabla \times \vec{E} &= - \frac{\partial \vec{B}}{\partial t}
 \end{aligned} \tag{3}$$

where  $\vec{D}$  is the electric displacement,  $\vec{H}$  the magnetic field,  $\vec{E}$  the electric field and  $\vec{B}$  the magnetic induction; also,  $\rho_e$  : charge density and  $\vec{j}$  : current. The classical MHD approximation is to neglect the displacement current in (ii) i.e., assume  $\partial \vec{D} / \partial t \approx 0$ ; this is equivalent to ignoring terms of order  $(v/c)^2$  or higher. Then, using (ii), (iii) (neglecting the displacement current) and (iv) along with Ohm's Law,  $\vec{j} = \sigma (\vec{E} + \vec{v} \times \vec{B})$  produces

$$\frac{\partial \vec{B}}{\partial t} = \nabla \times (\vec{v} \times \vec{B}) + \eta \nabla^2 \vec{B} \tag{4}$$

where

$$\eta = (\mu \sigma)^{-1} \quad , \quad \begin{array}{l} \sigma : \text{conductivity} \\ \mu : \text{magnetic permeability} \end{array}$$

Since  $\nabla \cdot \vec{B} = 0$  implies  $\vec{B} = \nabla \times \vec{A}$ , this equation can be "uncurled" to give

$$\frac{\partial \vec{A}}{\partial t} = \vec{v} \times \vec{B} + \eta \nabla^2 \vec{A} + \nabla \varphi \tag{5}$$

If we assume  $\vec{B} \cdot \hat{e}_z = 0$  (i.e. that  $B$  is two-dimensional) and that  $\vec{B}$  has a constant external part in the  $x$  direction,  $\vec{B} = B_0 \hat{e}_x + \nabla x(a \hat{e}_z)$  then  $\vec{A} = (yB_0 + a) \hat{e}_z$ . Placing this in equation (5) yields (2) (here  $\nabla \varphi = 0$ ). Since  $a = a(x,y)$ , the Coulomb gauge condition  $\nabla \cdot \vec{A} = 0$  is automatically satisfied.

The extended Navier-Stokes equation (Navier-Stokes + electromagnetic and gravitational body forces) is, for constant density (incompressibility),

$$\rho \left( \frac{\partial \vec{v}}{\partial t} + \vec{v} \cdot \nabla \vec{v} \right) = -\nabla(p + \rho \Phi) + \vec{j} \times \vec{B} + \rho \nu \nabla^2 \vec{v}$$

$\rho$  : density

$p$  : pressure

(6)

$\Phi$  : gravitational potential

$\nu$  : viscosity

Helmholz's theorem tells us that if we know the curl and divergence of a reasonably well behaved vector field, we can determine the vector field uniquely (see Arfken, 1972). Thus we can study the extended Navier-Stokes equation by taking its curl and divergence. Taking the curl, and assuming  $\vec{v} = \nabla x(\psi(x,y) \hat{e}_z)$  (i.e.,  $\vec{v}$  is two-dimensional and solenoidal) yields equation (1). Taking the divergence eliminates the time derivative term and yields a Poisson's equation for the pressure field. The equations (1) and (2) are now self contained and self consistent and we do not have to explicitly consider the thermodynamic equation (the heat equation and equation of state). The equation of continuity, because  $\vec{v}$  is solenoidal, reduces to  $d\rho/dt = 0$ , i.e.  $\rho$  is constant.

Without the  $B_0$  terms, eqs. (1) and (2) become those considered previously. In a recent derivation (Montgomery, 1982), the Strauss (1976) equations were re-derived using a perturbation expansion of the full set of incompressible MHD equations in three dimensions, in powers of  $B/B_0$ . It was necessary to assume in the derivation that the time derivatives  $\partial / \partial t$  remained of  $O(1)$ , or that no zeroth-order population of Alfvén waves was present. (The linearized solutions for the three-dimensional case, as for eqs. (1) and (2), is just a superposition of Alfvén waves with angular frequencies  $\omega(\vec{k}) = \pm \vec{k} \cdot \vec{B}_0$ , where  $\vec{k}$  is the wavenumber.) An objective of the present computation is to see how a spectrum evolves which does contain an initially isotropic spectrum of Alfvén waves. It will be shown that the spatial dependence of such a spectrum on the parallel spatial coordinate  $x$  becomes progressively relatively weaker with time.

## VI. COMPUTATIONAL TECHNIQUE

The essence of the computational method is that all physical fields are expanded in truncated Fourier series. The Fourier coefficients are stepped forward in time and are saved at predetermined time steps to provide a history of the dynamical evolution of the field variables. To be explicit, Fourier representations of  $\omega$  and  $a$  (for example) are (see, e.g., Fyfe et al, 1977a,b):

$$\omega(\vec{x}, t) = \sum_{\vec{k}} \omega(\vec{k}, t) \exp(i\vec{k} \cdot \vec{x}) \quad (7)$$

$$a(\vec{x}, t) = \sum_{\vec{k}} a(\vec{k}, t) \exp(i\vec{k} \cdot \vec{x}) \quad (8)$$

where  $\vec{k} = (k_x, k_y)$  and  $k_x$  and  $k_y$  are integers. Thus the dimension of the square box is chosen for convenience to be  $2\pi$ . The Fourier coefficients retained lie in the range  $k_{\min} = 1 \leq |\vec{k}| \leq k_{\max}$ , where  $k_{\max}$  is essentially limited by available computer time. Limitations on the Reynolds numbers are provided by the requirements that  $\nu$  and  $\eta$  be large enough so that the Fourier coefficients for  $|\vec{k}| \geq k_{\max}$  are suppressed.

The numerical code is a fully de-aliased, isotropically truncated (Galerkin) spectral method; please see Orszag (1971) and Patterson and Orszag (1971) for specific detail. The equations which the code solves are obtained if (7) and (8) are placed in (1) and (2); the result is similar to that of Kraichnan and Montgomery (1980):

$$\left(\frac{\partial}{\partial \tau} + \nu k^2\right) \omega(\vec{k}) = \sum_{\vec{p} + \vec{q} = \vec{k}} M_1(\vec{q}, \vec{p}) [\omega(\vec{q}) \omega(\vec{p}) - j(\vec{q}) j(\vec{p})] + i B_0 k_x j(\vec{k}) \quad (9)$$

$$\left(\frac{\partial}{\partial \tau} + \eta k^2\right) j(\vec{k}) = \sum_{\vec{p} + \vec{q} = \vec{k}} M_2(\vec{q}, \vec{p}) [j(\vec{q}) \omega(\vec{p}) - \omega(\vec{q}) j(\vec{p})] + i B_0 k_x \omega(\vec{k}) \quad (10)$$

where

$$M_1(\vec{q}, \vec{p}) = \frac{1}{2} \hat{e}_z \cdot (\vec{q} \times \vec{p}) (p^{-2} - q^{-2})$$

$$M_2(\vec{q}, \vec{p}) = \frac{1}{2} \hat{e}_z \cdot (\vec{q} \times \vec{p}) |\vec{p} + \vec{q}|^2 p^{-2} q^{-2}$$

The essence of the code is to solve the nonlinear terms by transformation to x space, evaluation of simple products and transformation back to k space, rather than direct evaluation of the k space convolution sums. The time-stepping is done by a second-order predictor-corrector method.

The first test of the code was to run it with the dissipative terms removed. Conservation laws can then be tested and comparisons can be made between the computed behavior of the Fourier coefficients and the predictions of the (unphysical) absolute equilibrium ensemble theory (see, e.g., Kraichnan and Montgomery, 1980).

The second step was to compare dissipative results from two runs, one having twice the other's value of  $k_{\max}$ , and thus having twice the spatial resolution. The third step was to run several cases with varying values for  $\nu$  and  $\eta$  at a particular value of  $B_0$ , to determine the influence of the Reynolds numbers. Finally, the last step was to run a number of cases which differed only in the value of  $B_0$ , thereby investigating the effect that varying mean magnetic field strength has on the dynamics.

Initial Fourier coefficients were chosen so that they would be non-zero only within a given annulus in  $\vec{k}$ -space. The  $\omega(k,t)$  were initially non-zero only for  $k_1 \leq k \leq k_2$ , and the  $a(k,t)$  were non-zero only for  $k_3 \leq k \leq k_4$ . Within their respective annuli, the values of the  $\omega(\vec{k},0)$  were chosen so that all  $|\vec{v}(\vec{k},0)| = |\omega(\vec{k},0)|/k$  were equal, and the  $a(\vec{k},0)$  were chosen so that all  $|\vec{B}(\vec{k},0)| = k|a(\vec{k},0)|$  were equal. The phases of the  $a(\vec{k},0)$  and  $\omega(\vec{k},0)$  were assigned randomly. The specification of the initial Fourier coefficients was completed by giving values for the magnetic energy  $E_B \equiv \sum_{\vec{k}} |\vec{B}(\vec{k},t)|^2/2$  and the kinetic energy  $E_v \equiv \sum_{\vec{k}} |\vec{v}(\vec{k},t)|^2/2$  at  $t = 0$ .

The total energy is  $E \equiv E_B + E_v$ , the "cross helicity" is  $P \equiv \sum_{\vec{k}} \vec{v}(\vec{k},t) \cdot \vec{B}^*(\vec{k},t)/2$ . The mean square vector potential is  $A \equiv \sum_{\vec{k}} |a(\vec{k},t)|^2/2$ .  $E$ ,  $P$ , and  $A$  are significant quantities in the theory of two dimensional MHD turbulence in the absence of a mean field: they are the only known non-dissipative invariants which remain invariant under truncation of the Fourier-expanded ( $\nu = 0 = \eta$ ) version of eqs. (1) and (2) with  $B_0 = 0$ . If  $B_0 \neq 0$ ,  $E$  and  $P$  still have this status, but  $A$  does not. We may define  $R \equiv E_B/E_v$  as the ratio of the energies.

About a dozen different sets of initial Fourier coefficients have been used for various runs. Many of the sets exhibited similar behavior. The number of different sets of initial conditions presented in this paper has been kept to a minimum, but for the runs discussed, there are others unreported for which the behavior was similar. Details of the runs explicitly discussed here are collected in Tables 1 and 2.



## VII. NON-DISSIPATIVE TESTS

To test the spectral code, several cases were run with  $\nu = \eta = 0$ , and the results compared with absolute equilibrium ensemble theory. Such results are, of course, unphysical, and should be regarded as preliminary to the dissipative results presented in Chapter 8.

Equilibrium ensemble theory for the  $B_0 = 0$  case was given by Fyfe and Montgomery (1976); the case  $B_0 \neq 0$  is recovered by simply deleting the third "rugged" constant of the motion A. The prediction is a simple equipartition,  $\langle |\vec{v}(\vec{k})|^2 \rangle = \langle |\vec{B}(\vec{k})|^2 \rangle = \text{const.}$ , independently of  $\vec{k}$ . This is true for all realizable values of  $\langle E \rangle$  and  $\langle P \rangle$ . The ratio  $\langle R \rangle \equiv \langle E_B \rangle / \langle E_v \rangle = 1$ , in sharp contrast to the  $B_0 = 0$  case. There is no crowding to the long wavelengths as  $k_{\max} \rightarrow \infty$ , as there is when  $B_0 = 0$ .

Non-dissipative computations were carried out with  $B_0 = 0$  and  $B_0 = 1$  for different sets of initial coefficients. Time averages were made of phase functions of the Fourier coefficients and these were compared with ensemble averages. The two should be equal to the extent that the system is ergodic.

The results of a single set of Fourier coefficients will be presented here, call it set A. For run A1,  $B_0 = 0$ , and for run A2,  $B_0 = 1$ . For both runs,  $k_{\max} = 16$ ,  $E = 1.0$ , the time step was  $(256)^{-1}$ . The total number of time steps was 12,800. For these conditions,  $k_1 = k_3 = 3$  and  $k_2 = k_4 = 5$ . Time averages were performed over the last 11,520 time steps.

Table 1a. Non-dissipative runs ( $\nu = 0 = \eta$ ) for comparison with absolute equilibrium ensemble theory [Time step:  $(256)^{-1}$ . Total no. of time steps: 12,800. Averages taken over last 11,520 time steps.]

	<u>Initial</u>	<u>Final</u>	<u>Time Average</u>	<u>% Change (Initial-Final)</u>
A1( $B_0 = 0$ )				
E	1.000	0.9714	0.9782	2.9
P	0.2354	0.2167	0.2227	7.9
A	0.03288	0.03286	0.03288	0.06
A2( $B_0 = 1$ )				
E	1.0000	1.0150	1.0062	1.5
P	0.2354	0.2277	0.2313	3.3
A	0.03288	0.01497	0.01489	54.5

Table 1b.

$R = E_B/E_V$				
	<u>Initial</u>	<u>Final</u>	<u>Time Average</u>	<u>Theoretical</u>
A1	1.0000	1.0058	1.0608	1.0484
A2	1.0000	0.9825	1.0004	1.0000

The comparison between the numerical results and the ensemble predictions is given in Table 1 and in Figures 9 through 12. In Table 1, the behavior of  $E$ ,  $P$ ,  $A$ , and the evolving ratio  $R_t \equiv E_B/E_V$  is shown as a function of time. The invariants  $E$ ,  $P$ , and  $A$  for  $B_0 = 0$  and  $E$  and  $P$  for  $B_0 = 1$  are conserved to a few percent in all cases. Non-dissipative runs for initial conditions "B" ( $E_B = E_V = \frac{1}{2}$ ,  $k_1^2 = 5$ ,  $k_2^2 = 8$ ,  $k_3^2 = 10$ ,  $k_4^2 = 13$ ) will not be reported in detail.

In figures 9 through 12, the directionally averaged magnetic and kinetic modal energies are presented for time averaged data. (Directional averaging means averaging over all values of  $\vec{k}$  corresponding to a particular  $k^2$ .) At the lower values of  $k$ , where the number of degenerate  $\vec{k}$ 's is sparse, occasionally large anisotropies necessarily appear, but no systematic directionality was observed. An explicit comparison of these runs with corresponding dissipative runs will be presented in the next section, after suitable measures of anisotropy are defined. It will be seen that the non-dissipative runs, in contrast to the dissipative ones, show no anisotropy when averaged over long times.

In Figures 9 through 12, the spectral predictions of the absolute equilibrium ensemble theory are shown as solid lines and the plotted points are the time-averaged results of the computations. No significant departures from the predictions of the absolute equilibrium ensemble theory have been observed in these runs, and in others not reported here (except, perhaps, for the presence of certain spikes, which will be briefly commented on in Appendix B). Typical behavior for almost all the individual Fourier modes (those with  $k_x \neq 0$ ) is that of the Alfvén wave of angular

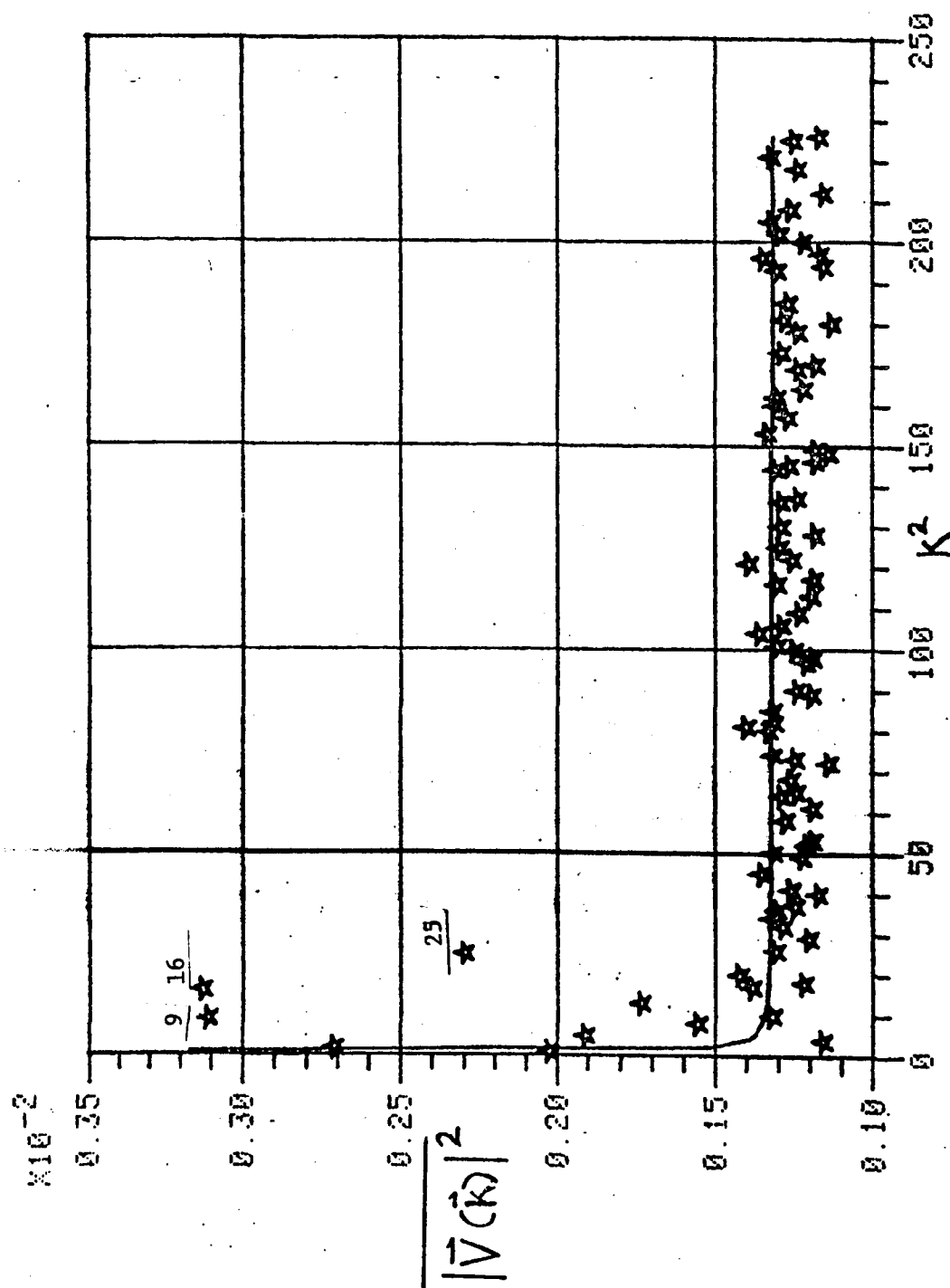


Figure 9. Directionally averaged kinetic energy spectra for run A1:

$B_0 = 0$ ,  $\nu = \eta = 0$ ,  $k_{\max} = 16$ . Solid line is theoretical prediction.

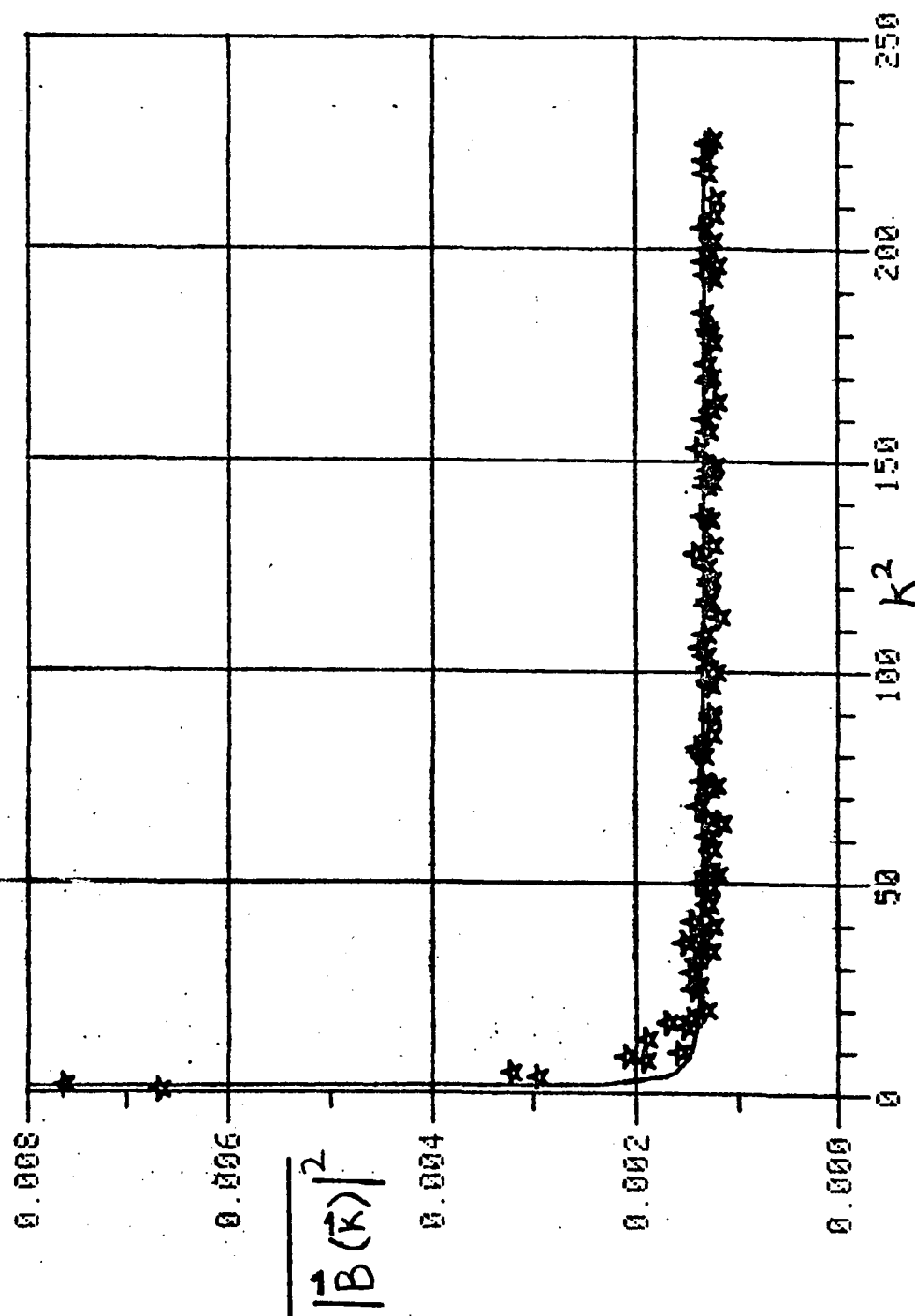


Figure 10. Directionally averaged magnetic energy spectra for run Al:

$B_0 = 0$ ,  $\nu = \eta = 0$ ,  $k_{\max} = 16$ . Solid line is theoretical prediction.

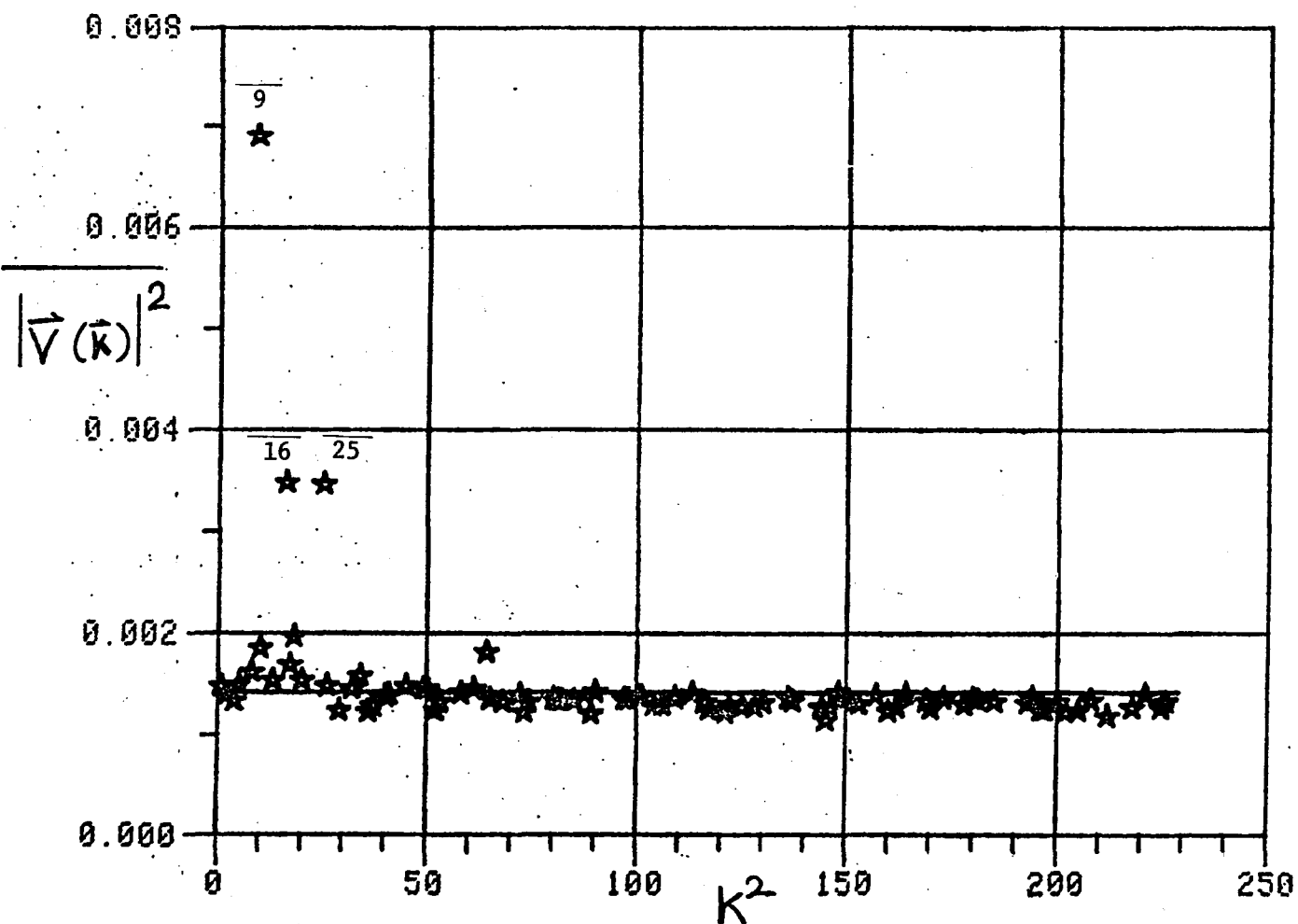


Figure 11. Directionally averaged kinetic energy spectra for run A2:

$B_0 = 1$ ,  $\nu = \eta = 0$ ,  $k_{\max} = 16$ . Solid line is theoretical prediction.

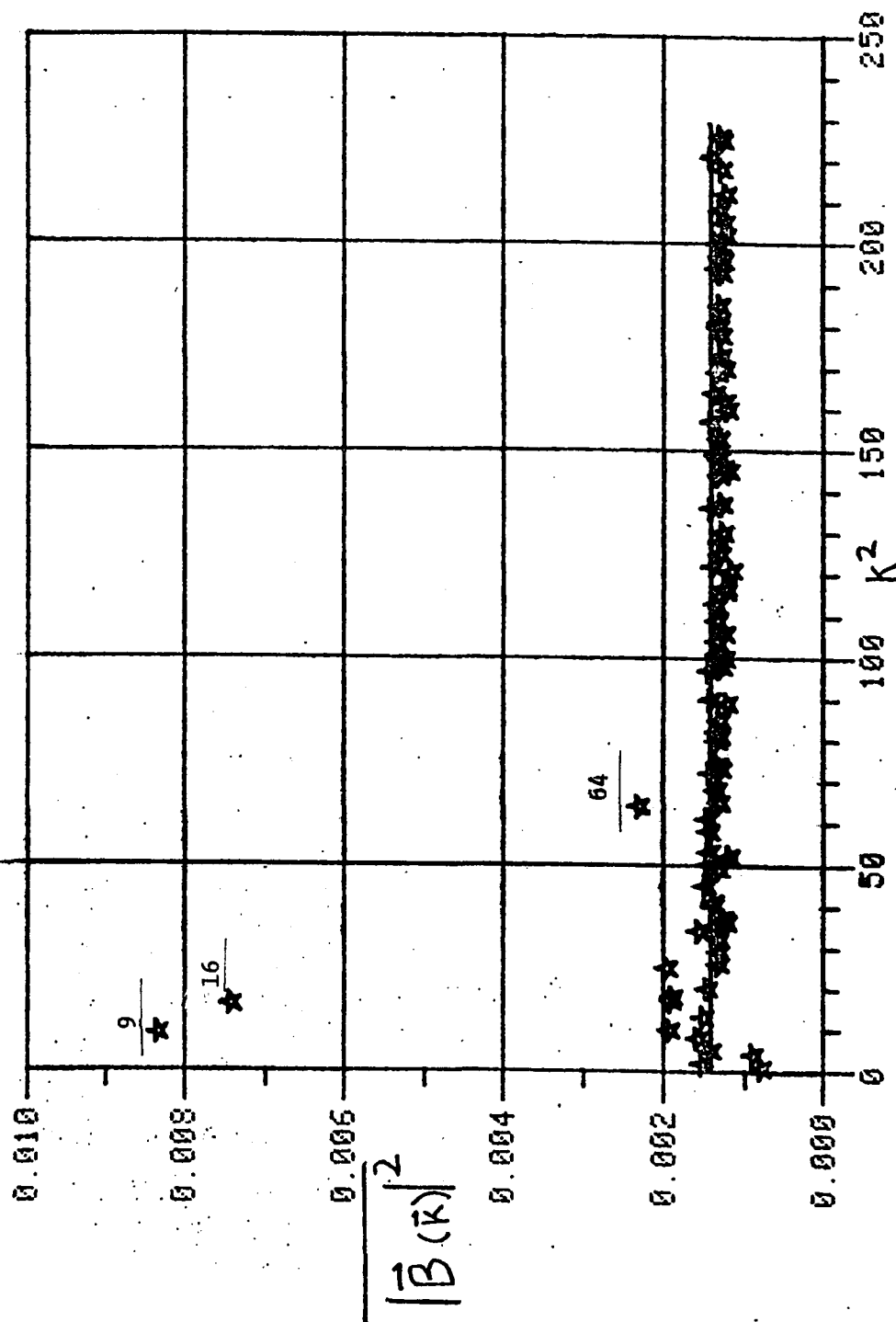


Figure 12. Directionally averaged magnetic energy spectra for run A2:

$B_0 = 1$ ,  $v = \eta = 0$ ,  $k_{\max} = 16$ . Solid line is theoretical prediction.

frequency  $\omega(\vec{k}) = \vec{k} \cdot \vec{B}_0$ . This is the principal qualitative difference in the time behavior observed between the  $B_0 = 0$  and  $B_0 \neq 0$  cases. Superposed on the Alfvén-wave oscillations is a slower transfer of excitation between the Fourier modes.

In the next few sections, we pass to a consideration of the dissipative cases. In order to maintain a common thread throughout the discussion, we will primarily use set A as the initial conditions for the dissipative runs to be presented. The principal quantities to be varied are the spatial resolution  $k_{\max}$ , the values of the dissipation coefficients  $\nu$  and  $\eta$ , and the external field strength  $B_0$ .



VIII. APPEARANCE OF ANISOTROPY: EFFECTS OF VISCOSITY,  
RESISTIVITY, AND SPATIAL RESOLUTION

In this section, we describe dissipative runs. The presence of dissipation is always central in the evolution of any real turbulent field.

We use primarily the same initial Fourier coefficients as those in Chapter 7. The most striking effect we have observed is that when both dissipation and a mean  $B_0$  are present, anisotropy appears. The  $\vec{k}$  spectrum evolves into one peaked perpendicularly to the mean field  $\vec{B}_0$ . We describe the dependence of this anisotropy on the dissipation coefficients and the mean  $B_0$ , after first remarking upon some considerations of necessary spatial resolution.

For an accurate solution to eqs. (1) and (2), we must resolve the smallest dynamically significant spatial scales that  $\nu$  and  $\eta$  permit. An estimate for these is provided by the Kolmogoroff "dissipation wave number", constructed by dimensional analysis based on the rate of dissipation of energy. For MHD in two dimensions, it is

$$k_d = [\eta^{-3} |dE_B/dt| + \nu^{-3} |dE_V/dt|]^{1/4} \quad (11)$$

where  $|dE_B/dt|$  and  $|dE_V/dt|$  are the ohmic and viscous energy dissipation rates, respectively. Ideally,  $k_d$  should be less than  $k_{\max}$  for accurate solution of eqs. (1) and (2) and this provides at present the most severe limitation on turbulence computations, both Navier-Stokes and MHD. For some purposes, it may be that when the smallest scales are

dynamically insignificant,  $k_d$  somewhat larger than  $k_{\max}$  may be tolerated, but  $k_d \gg k_{\max}$  must always signal uselessness in a turbulence computation. Other measures of mean length scales for the turbulent field, such as those of Pao and Taylor (see, e.g., Leslie 1973) may be used to characterize turbulent activity, but the Kolmogoroff scale is the one most widely accepted and we shall use it hereafter.

The dissipation wave number may be adjusted empirically, for a given set of initial Fourier coefficients, by raising  $\nu$  and  $\eta$  until the computed  $k_d$  remains no greater than  $k_{\max}$ . We consider here only the case  $\nu = \eta$  (unit magnetic Prandtl number).

In the initial set of dissipative cases, there are six runs (A3 through A8, see Table 2), having  $B_0 = 0$  and  $B_0 = 1$  for  $\nu = \eta = 0.005$ , 0.01 and 0.02. The following characteristics were common to these six runs:  $k_{\max} = 32$ , time step =  $(256)^{-1}$ , total number of time steps = 1280, initial Fourier coefficients: set A. The temporal evolution of the variables  $E$ ,  $P$ ,  $A$ , and  $R_t$  for the runs with  $\nu = \eta = 0.01$  are shown in Figures 13 and 14. (Qualitatively similar behavior was observed for  $\nu = \eta = 0.005$  and 0.02, the decay times simply increased and decreased, respectively.)

When  $B_0 = 0$ , roughly twice as much magnetic as kinetic energy develops; when  $B_0 = 1$ , the ratio remains approximately unity.  $E$ ,  $P$ ,  $A$  all monotonically decay for  $B_0 = 0$ , but when  $B_0 = 1$ ,  $A$  actually increases at times, but overall decays.

To measure anisotropy in the  $\vec{k}$  spectrum, a set of angles were defined for each Fourier-decomposable field.

$$\theta_Q \equiv \tan^{-1} \left\{ \left[ \sum_{\vec{k}} k_y^2 |Q(\vec{k}, t)|^2 / \sum_{\vec{k}} k_x^2 |Q(\vec{k}, t)|^2 \right]^{1/2} \right\} \quad (12)$$

Table 2. Run Parameters

<u>Run</u>	<u>k<sub>max</sub></u>	<u>v<sub>z</sub>η</u>	<u>B<sub>0</sub></u>	<u>Time Step Size</u>	<u>Total # of Time Steps</u>
A1	16	0	0	1/256	12800
A2	16	0	1	1/256	12800
A3	32	.005	0	1/256	1280
A4	32	.005	1	1/256	1280
A5	32	.01	0	1/256	1280
A6	32	.01	1	1/256	1280
A7	32	.02	0	1/256	1280
A8	32	.02	1	1/256	1280
A9	16	.01	0	1/128	640
A10	16	.01	1	1/128	640
A11	16	.01	1/16	1/128	640
A12	16	.01	1/8	1/128	640
A13	16	.01	1/4	1/128	640
A14	16	.01	1/2	1/128	640
A15	16	.01	2	1/256	1280
A16	16	.01	4	1/512	2560
A17	16	.01	8	1/1024	5120
A18	16	.01	16	1/2048	10240
B1	16	0	1	1/128	3200
B2	16	.0025	1	1/128	3200

Set A: initial equipartition of energy in Fourier modes such that  $9 \leq k^2 \leq 25$ ; Fourier modes outside the annulus initially set to zero.

Set B: initial equipartition of kinetic energy in Fourier modes such that  $5 \leq k^2 \leq 8$ , and magnetic such that  $10 \leq k^2 \leq 13$ ; Fourier modes outside these annuli initially set to zero.

Initial rms values of  $B^2$  and  $v^2$  were both equal to one for Sets A and B.

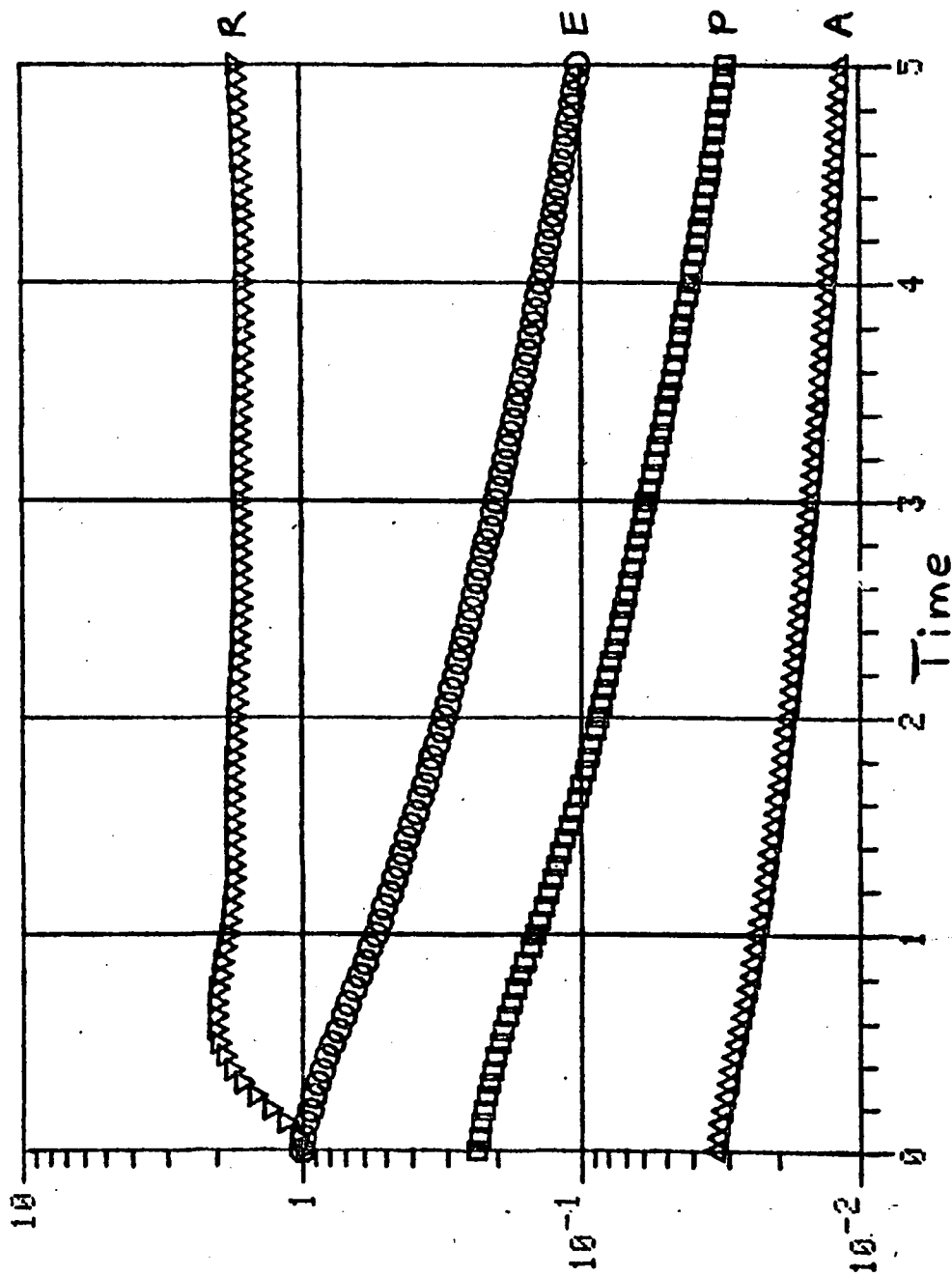


Figure 13. The quantities E, P, A, and R for run A5:  $B_0 = 0$ ,  $v = \eta = 0.01$ ,

$$k_{\max} = 32.$$

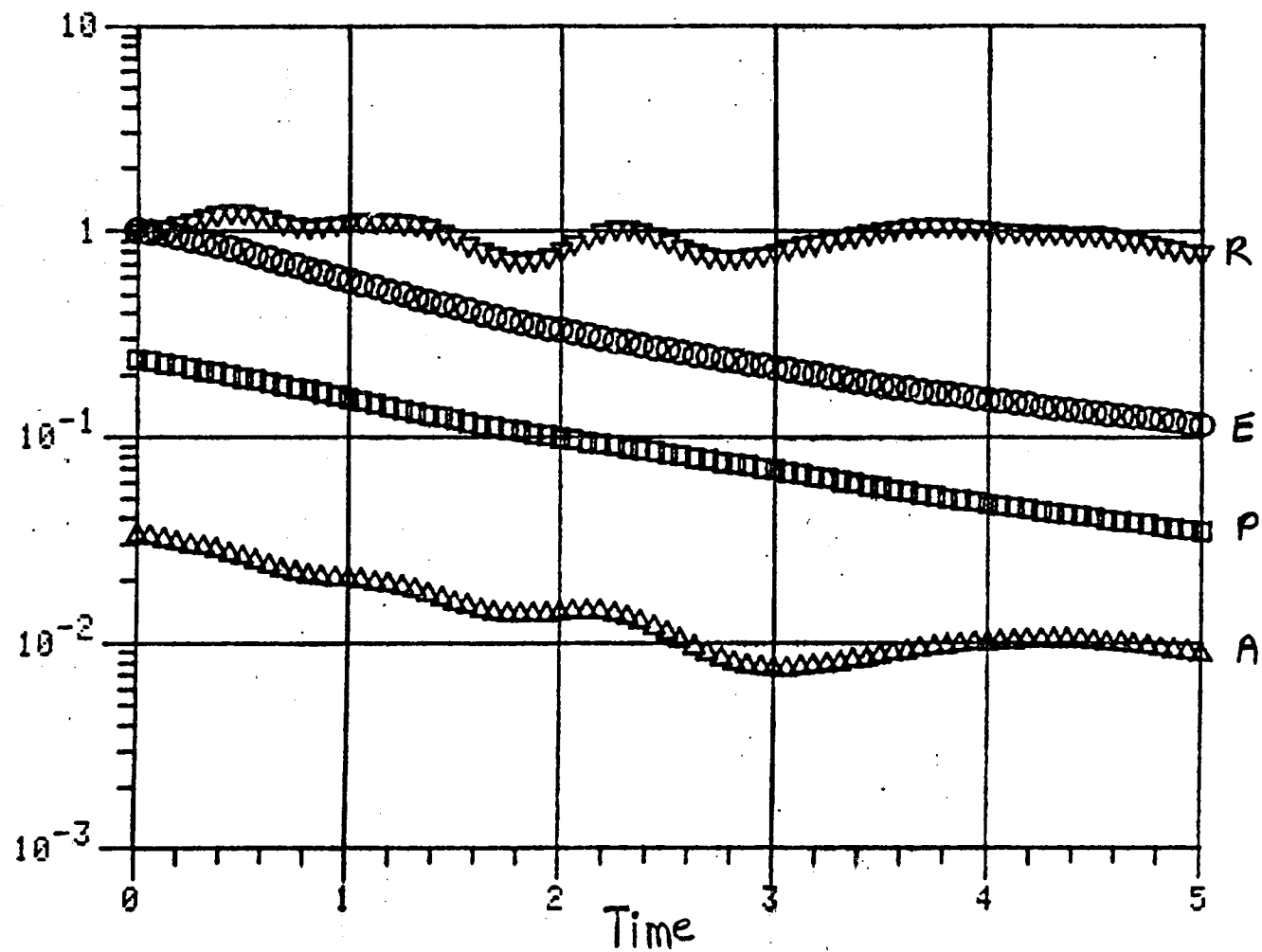


Figure 14. The quantities E, P, A, and R for run A6:  $B_0 = 1$ ,  $\nu = \eta = 0.01$ ,

$$k_{\max} = 32.$$

where  $Q$  is any one of the fields  $\mathcal{V}$ ,  $\vec{v}$ ,  $\omega$ ,  $a$ ,  $\vec{B}$ , or  $j$ . For a  $\vec{k}$  spectrum purely normal to  $\vec{B}_0$ ,  $\theta_Q$  is  $90^\circ$ , and for an isotropic spectrum,  $45^\circ$ .

Temporal evolution of the angles for  $B_0 = 0$  and  $B_0 = 1$  is illustrated, for runs A5 and A6, in Figures 15 and 16, which both refer to  $\nu = \eta = 0.01$ . For  $B_0 = 0$ , the angles roam unsystematically about  $45^\circ$ , indicating isotropic development. The anisotropy in Figure 16, for  $B_0 = 1$ , is typical. Notice that the angles tend to increase in the following order:  $\theta_{\mathcal{V}} < \theta_v < \theta_\omega$ , and  $\theta_a < \theta_B < \theta_j$ : the anisotropy is most pronounced at the shorter wavelengths. Also, when we consider  $\nu = \eta = 0.005$  and 0.02 as well, we see that the degree of anisotropy tends to decrease with increasing  $\nu$  and  $\eta$ . The results are summarized in Table 3, which displays averages of the  $\theta_Q$  for  $\nu = \eta = 0.005$ , 0.01, and 0.02 between times 1.5 and 5.0.

Also calculated were the dissipation wave number  $k_d$  (eq. (11)), mean square vorticity  $\Omega = \sum_{\vec{k}} |\omega(\vec{k}, t)|^2$ , and mean square current  $J = \sum_{\vec{k}} |j(\vec{k}, t)|^2$ ; the latter two quantities are required to evaluate eq. (11). The temporal evolution of  $\Omega$  and  $J$  for runs A5 and A6 ( $\nu = \eta = 0.01$ ) is shown in Figure 17. Table 4 displays the maximum values of  $k_d$ ,  $\Omega$ , and  $J$  for the six runs A3 through A8. In Table 4, it is apparent that the maximum dissipation wave number decreases with increasing  $\nu$  and  $\eta$ , as do the maxima of  $J$  and  $\Omega$ . The presence of a finite  $B_0$  also apparently enforces a more nearly equal partition of dissipation between  $\Omega$  and  $J$ .

From the foregoing results, it is clear that the maximum  $k_d$  which will fit inside the resolution  $k_{\max} = 32$  occurs for runs A5, A6,

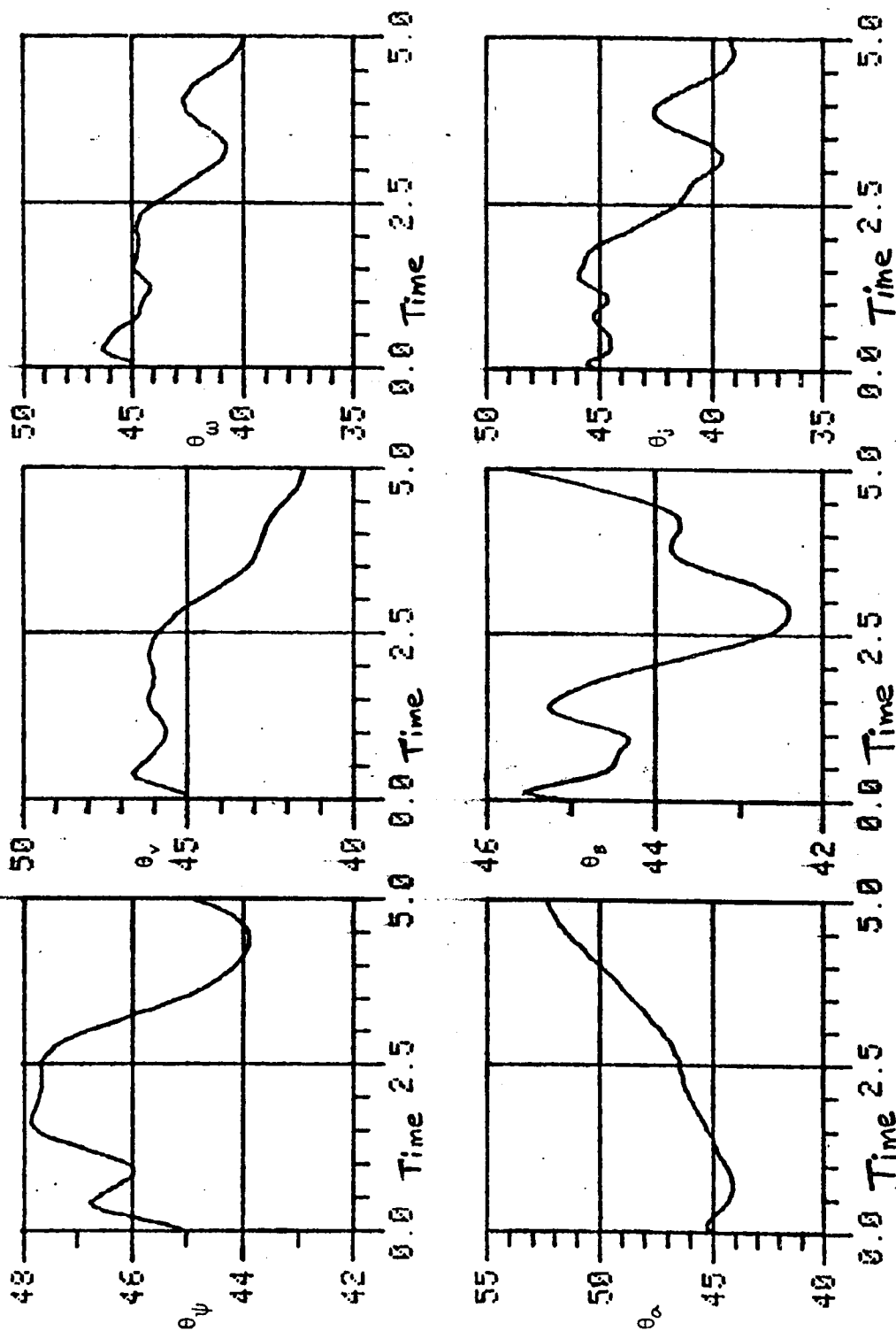


Figure 15. Measures of anisotropy for run A5:  $B_0 = 0$ ,  $v = \eta = 0.01$ ,  $k_{\max} = 32$ .

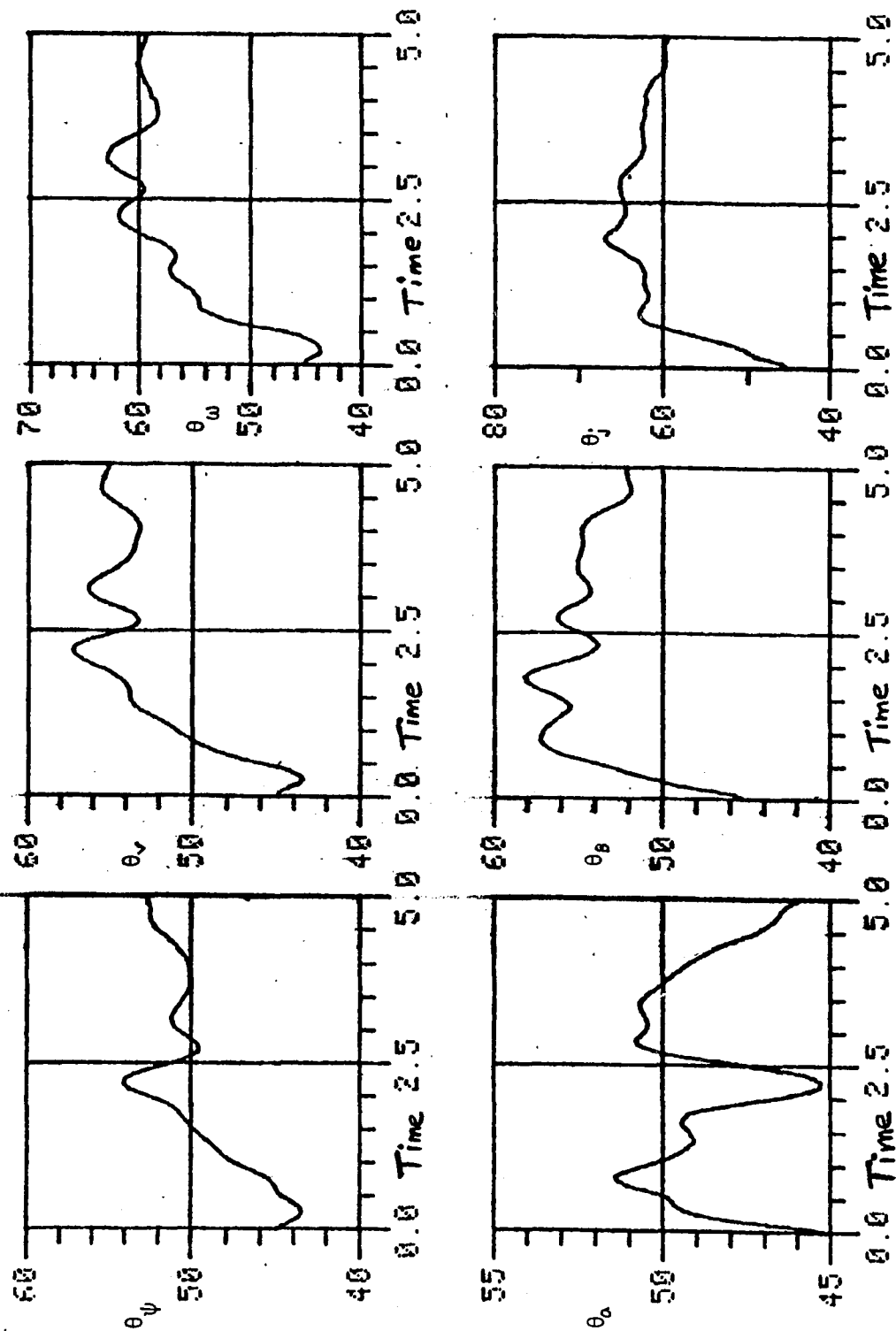


Figure 16. Measures of anisotropy for run A6:  $B_0 = 1$ ,  $v = \eta = 0.01$ ,  $k_{\max} = 32$ .



Table 3. Average Angles between  $t = 1.5$  and  $5.0$ 

<u><math>v, \eta</math></u>	<u><math>\theta_\psi</math></u>	<u><math>\theta_a</math></u>	<u><math>\theta_v</math></u>	<u><math>\theta_B</math></u>	<u><math>\theta_\omega</math></u>	<u><math>\theta_j</math></u>
.005	53.4	50.6	58.2	59.3	64.0	67.5
.01	51.6	48.5	54.8	55.0	60.5	64.0
.02	48.7	46.5	50.8	50.2	53.6	56.6

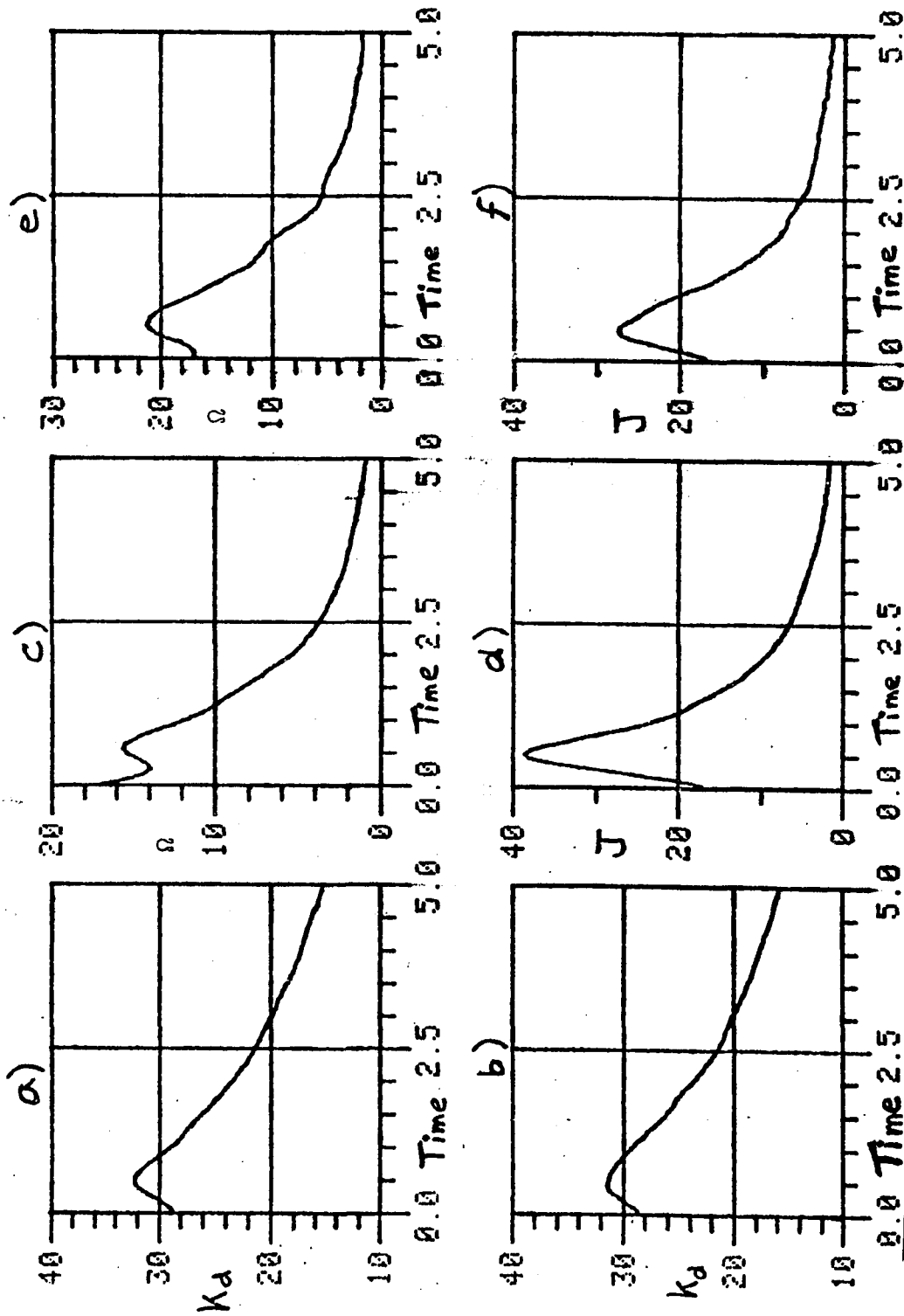


Figure 17. a) Dissipation wave number for run A5; b) dissipation wave number for run A6; c) mean square vorticity for run A5; d) mean square current for run A6; e) mean square vorticity for run A6; f) mean square current for run A6.

Table 4. Maximum Values of  $k_d$ ,  $\Omega$  and J for runs A3 through A8

<u>Run</u>	<u><math>v, \eta</math></u>	<u><math>B_0</math></u>	<u>Max <math>k_d</math></u>	<u>Max <math>\Omega</math></u>	<u>Max J</u>
A3	.005	0	49.6	25.0	51.8
A4	.005	1	48.3	30.6	38.0
A5	.01	0	32.2	17.0	39.0
A6	.01	1	31.4	21.4	27.8
A7	.02	0	21.0	17.0	26.8
A8	.02	1	20.8	17.0	20.3

where  $\nu = \eta = 0.01$ . To test the effect of lowering the resolution below  $k_{\max}$  on the results of runs A5 and A6, runs A9 and A10 were made with identical parameters to A5 and A6, but with  $k_{\max} = 16$ . (We also showed that halving  $k_{\max}$  allowed doubling the time step.) In runs A9 and A10, the time histories of the angles  $\theta_Q$  and the quantities  $k_d, \Omega$ , and  $J$  were essentially the same as those for A5 and A6. This insensitivity to halving the spatial resolution, so that  $k_{\max}$  falls well inside  $k_d$ , gives us some confidence in the validity of the results of such runs at the higher Reynolds numbers, such as runs A3 and A4, where  $k_{\max}$  lies outside  $k_d$ .

We should remark at this point on the question of the anisotropy of the non-dissipative runs. In Figure 18, we display the evolution of the angles  $\theta_v$  and  $\theta_B$  for a non-dissipative run B1 and a dissipative run B2 ( $\nu = \eta = 0.0025$ ). Both runs have the same initial Fourier coefficients with  $k_1^2 = 5$ ,  $k_2^2 = 9$ ,  $k_3^2 = 10$ ,  $k_4^2 = 13$ ;  $E_B = E_v$  for both runs, and the non-vanishing Fourier coefficients have equal amplitudes within their respective annuli, and random phases. (See Table 2.)

Referring to Figure 18, we can see that for B1, although  $\theta_v$  and  $\theta_B$  initially rise to about  $51^\circ$  and  $55^\circ$  respectively, they subsequently fall and oscillate about  $45^\circ$ . Run B2, however, shows  $\theta_v$  and  $\theta_B$  rising to maxima of approximately  $66^\circ$  and  $68^\circ$ , respectively, and then oscillating near those values. At the beginning of the dissipationless run, there apparently is a tendency toward anisotropy which cannot maintain itself; the  $\nu = \eta = 0.0025$  run remains strongly

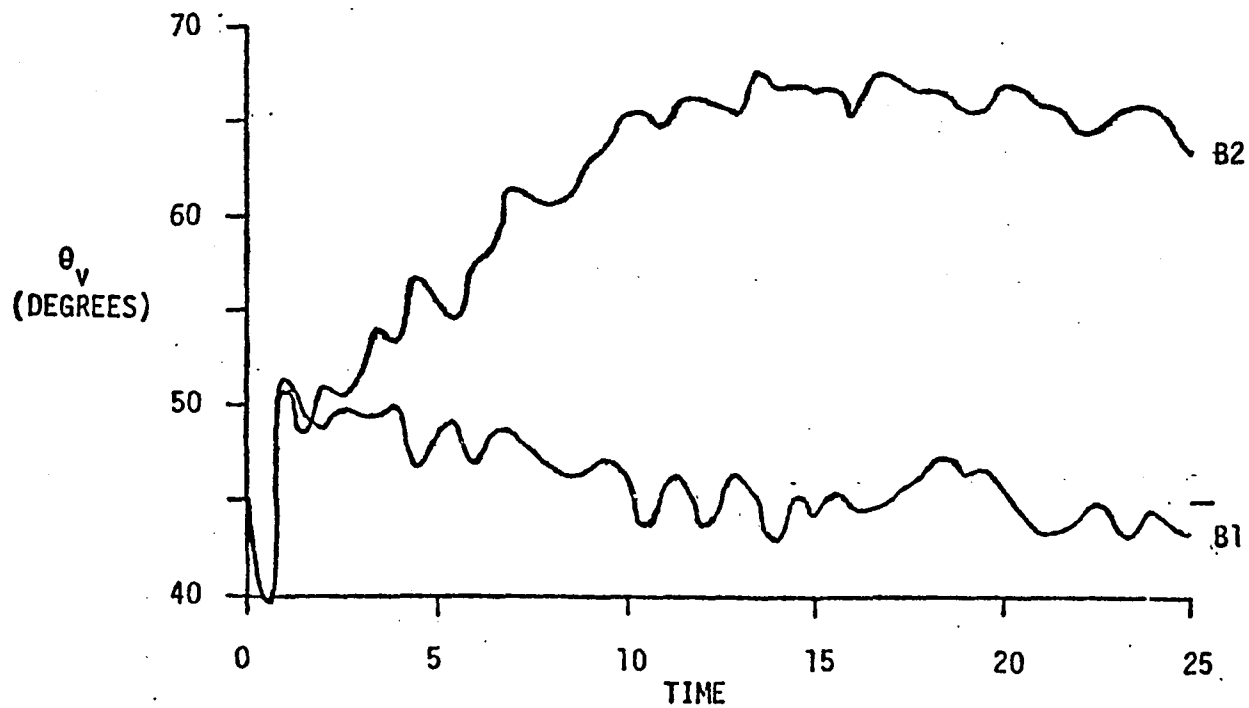
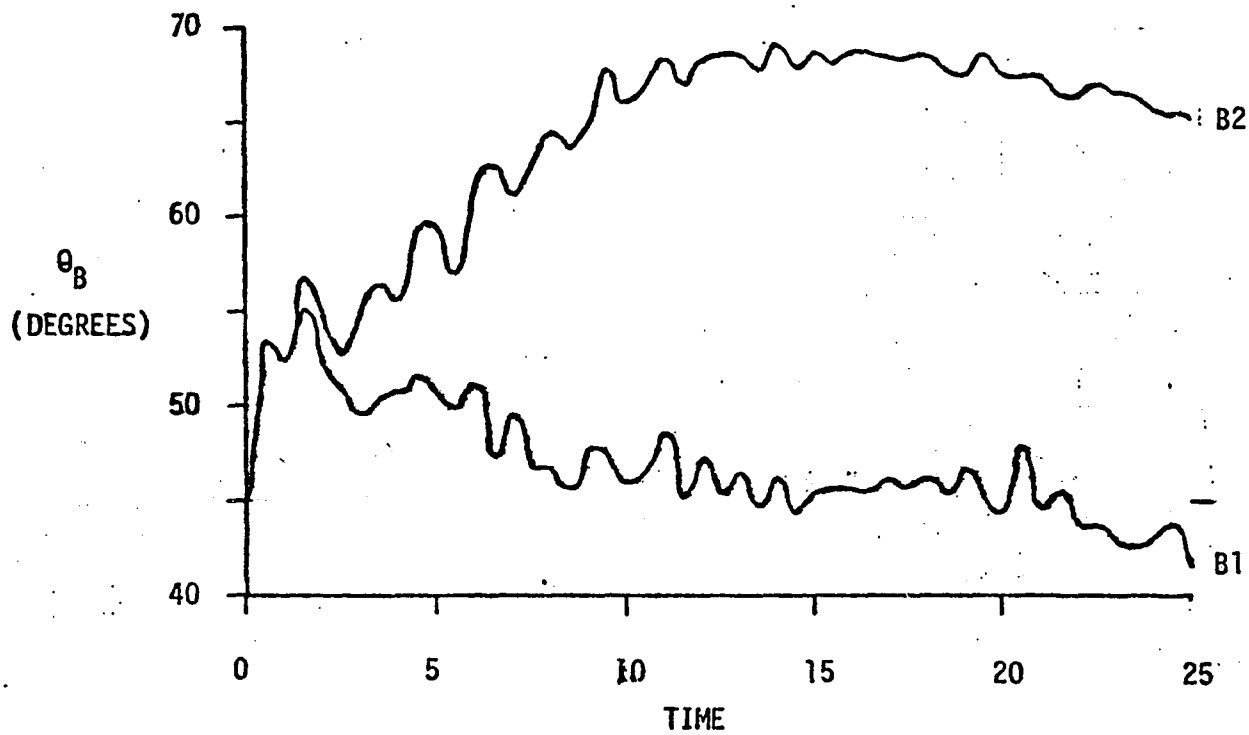


Figure 18. The angles  $\theta_v$  and  $\theta_B$  for runs B1 ( $B_0 = 1$ ,  $\nu = \eta = 0$ ) and B2 ( $B_0 = 1$ ,  $\nu = \eta = 0.0025$ ).

anisotropic, however. This behavior, involving the necessity of small but finite dissipation in the maintenance of anisotropy, corresponds, to a simple physical effect which is discussed in Chapter 10. It is our belief that no long-time anisotropy is to be expected without the presence of dissipation, and (for reasons given in Chapter 10) that the smaller the dissipation coefficients, the greater the degree of anisotropy is likely to be. A computation which could afford the spatial resolution to resolve significantly higher values of  $k_d$  than we can resolve would see proportionately higher degrees of anisotropy.

## IX. EFFECTS OF VARIABLE MEAN FIELD STRENGTH

Having discussed the effects of the spatial resolution  $k_{\max}$  and the dissipation coefficients  $\nu$  and  $\eta$  on the results, we pass to a consideration of the effects of varying the mean field  $B_0$ . Set A is chosen for the initial Fourier coefficients, and  $k_{\max} = 16$ . Thus the runs in this section are initially similar to A9 and A10, except that  $B_0$  takes on the values  $1/16, 1/8, 1/4, 1/2, 2, 4, 8$ , and  $16$ . These values correspond to runs A11 through A18, respectively. (Parameters for all runs considered appear in Table 2.)

Rather than display a multitude of graphs similar to those presented for runs A9 and A10, we display mainly graphs of time averaged angles  $\theta_Q$ . In Figure 19, we show  $\theta_Q$ , averaged over times 1.5 to 5.0, as functions of  $B_0$ . In Figure 20, we show, as functions of  $B_0$ , the maximum value of  $k_d$ , the time when this maximum occurs, the maximum enstrophy  $\Omega$ , and the maximum mean square current  $J$ .

Figure 19 and 20 illustrate a number of interesting effects. First, there is anisotropy which develops as  $B_0$  increases from zero. Second, the effect saturates: beyond a value of  $B_0$  of about 2, further increase in  $B_0$  results in no further increase in anisotropy, for these values of  $k_{\max}$ ,  $\nu$ , and  $\eta$ . Third, the values of  $\Omega$  and  $J$  approach each other as  $B_0$  increases, reflecting a progressively more Alfvén-wave-like behavior at the dissipation scales. The anisotropy continued to be

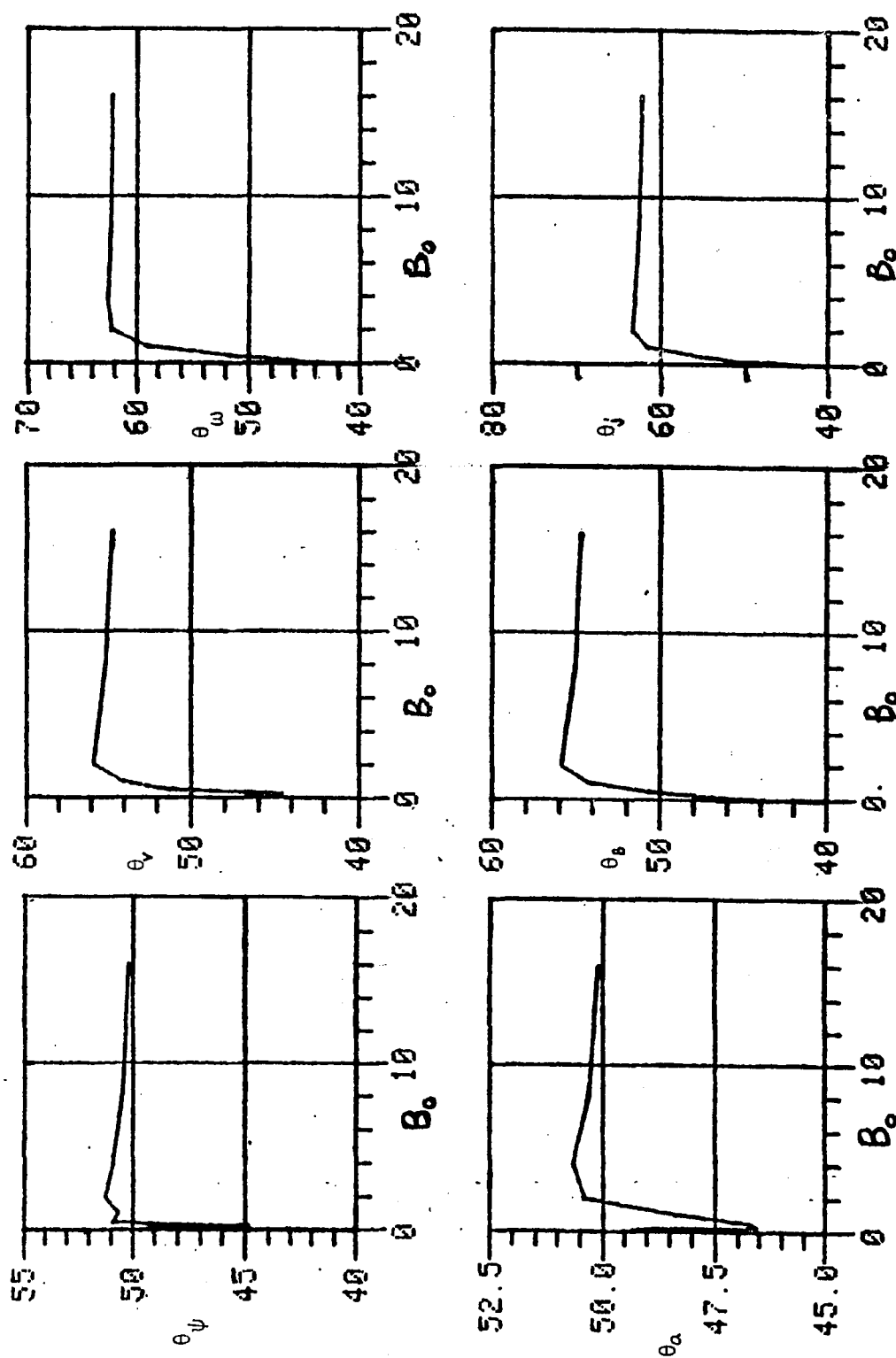


Figure 19. Measures of anisotropy as a function of mean field strength  $B_0$ .



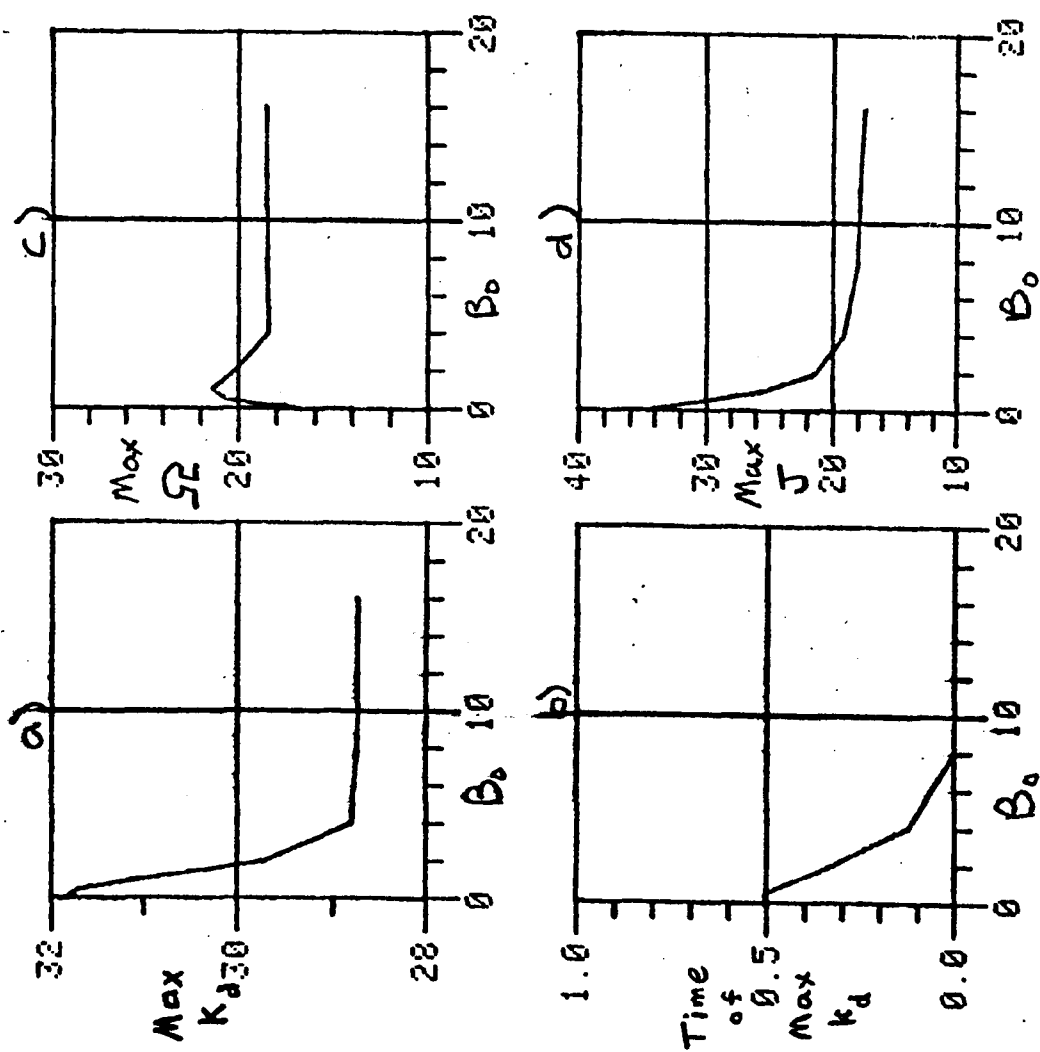


Figure 20. a) Maximum  $k_d$  as a function of  $B_0$ ; b) time of max  $k_d$ ; c) maximum mean square vorticity as a function of  $B_0$ ; d) maximum mean square current as a function of  $B_0$ .

most pronounced at the highest wave numbers:  $\theta_\omega$  and  $\theta_j$  were larger than the other angles.

A physical feeling for the configuration-space manifestations of the anisotropy may be obtained from Figure 21. There, contour plots are given for the vorticity  $\omega(x,t)$  and current  $j(x,t)$  at various times with a zero and a non-zero value of  $B_0$ . For the plot in which  $B_0 = 2$  it is clear that, at time  $t = 2.0$ , the vorticity and current contours have elongated in the direction of the mean field, reminiscent of the elongations, that were reported in the ZETA and Macrotor devices. In addition, Figure 22 shows the difference in spectral development for dissipative runs with and without a mean field. (In this figure it must be kept in mind that the spectra are slightly elongated vertically, due to printer characteristics; small tic marks signify  $45^\circ$ ,  $-45^\circ$ ,  $135^\circ$  and  $-135^\circ$ .)

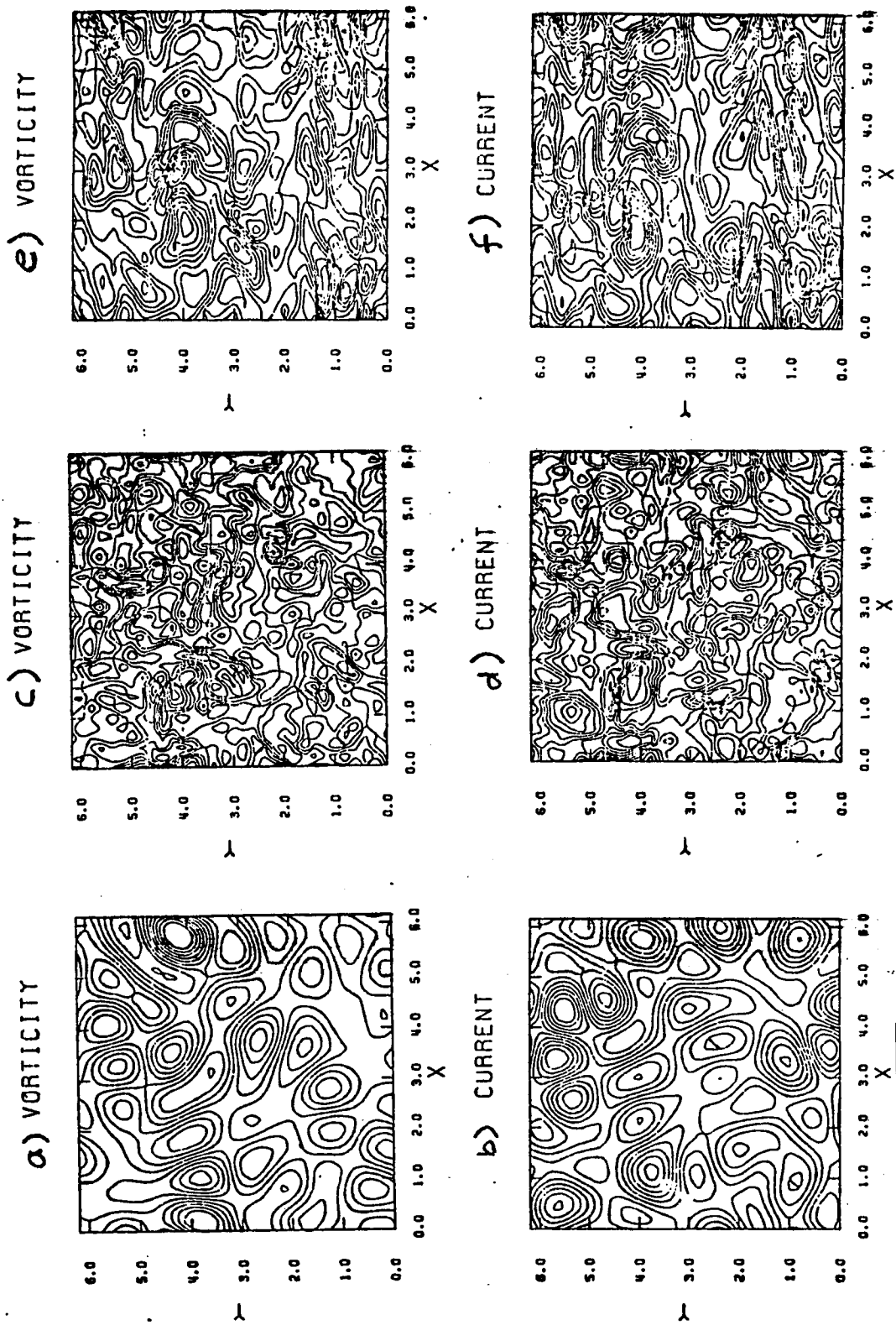


Figure 21. a) Vorticity of set A at  $t = 0$ ; b) current of set A at  $t = 0$ ;

c) vorticity of run A9 ( $B_0 = 0$ ,  $v = \eta = .01$ ,  $k_{\max} = 16$ ) at  $t = 2.0$ ;

d) current of run A9 at  $t = 0$ ; e) vorticity of run A15 ( $B_0 = 2$ ,

$v = \eta = .01$ ,  $k_{\max} = 16$ ) at  $t = 2.0$ ; f) current of run A15 at  $t = 2.0$ .

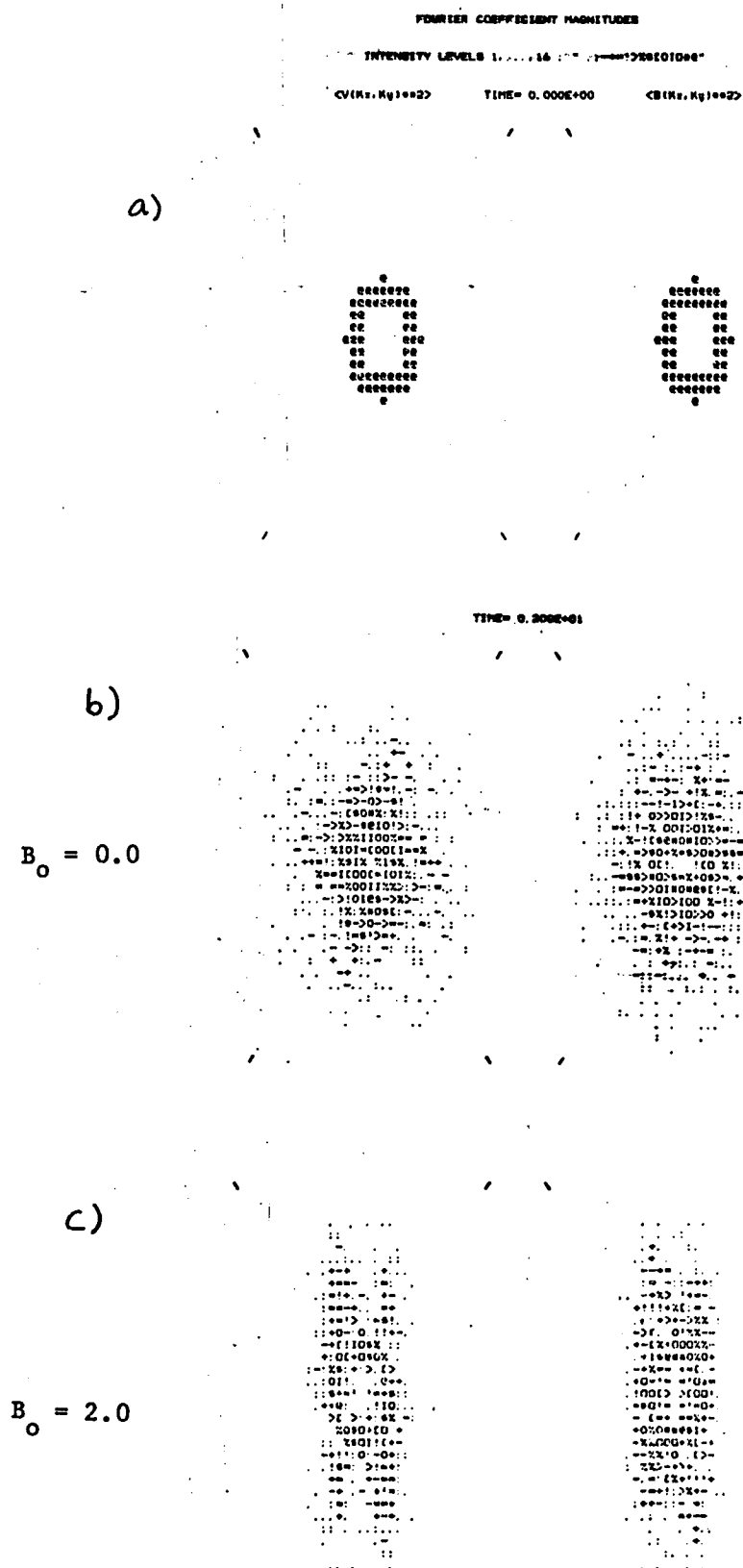


Figure 22.- Fourier coefficient magnitudes: (a) for runs A9 and A15 initially; (b) for run A9 at  $T = 2$ ; (c) for run A15 at  $T = 2$ . (Please note slight vertical elongation.)

## X. DISCUSSION

The linearized MHD equations in two and three dimensions result from discarding the right hand sides of

$$\frac{\partial \vec{v}}{\partial t} - \vec{B}_0 \cdot \nabla \vec{B} - \nu \nabla^2 \vec{v} = \vec{B} \cdot \nabla \vec{B} - \vec{v} \cdot \nabla \vec{v} - \nabla p \quad (13)$$

and

$$\frac{\partial \vec{B}}{\partial t} - \vec{B}_0 \cdot \nabla \vec{v} - \eta \nabla^2 \vec{B} = \vec{B} \cdot \nabla \vec{v} - \vec{v} \cdot \nabla \vec{B} \quad (14)$$

subject to  $\nabla \cdot \vec{v} = 0 = \nabla \cdot \vec{B}$ . Temporarily ignoring the dissipation and pressure gradient, (7) and (8) can alternately be added and subtracted to yield

$$\begin{aligned} \frac{\partial \vec{L}}{\partial t} - \vec{B}_0 \cdot \nabla \vec{L} &= \vec{L} \cdot \nabla \vec{R} \\ \frac{\partial \vec{R}}{\partial t} + \vec{B}_0 \cdot \nabla \vec{R} &= \vec{R} \cdot \nabla \vec{L} \end{aligned} \quad (15)$$

where  $\vec{R} = \vec{B} - \vec{v}$  and  $\vec{L} = \vec{B} + \vec{v}$ . If  $|\vec{B}_0|$  is assumed large with respect to  $|\vec{L}|$  and  $|\vec{R}|$ , then the nonlinear terms on the right hand sides in (9) can be ignored in a zeroth order approximation; then  $\vec{R}$  is simply a superposition of right-travelling (Alfvén) waves and  $\vec{L}$  is a superposition of left-travelling waves:

$$\begin{aligned} \vec{R} &= \sum_{\vec{k}} \vec{R}(\vec{k}) \exp[i \vec{k} \cdot (\vec{x} - \vec{B}_0 t)] \\ \vec{L} &= \sum_{\vec{k}} \vec{L}(\vec{k}) \exp[i \vec{k} \cdot (\vec{x} + \vec{B}_0 t)] \end{aligned} \quad (16)$$

where  $\vec{R}(\vec{k}) = \vec{R}^*(-\vec{k})$ ,  $\vec{L}(\vec{k}) = \vec{L}^*(-\vec{k})$ . Here, the frequency of the waves is  $\omega(\vec{k}) = \vec{k} \cdot \vec{B}_0$ .

Assuming that eqs. (16) are a satisfactory zeroth order solution to eqs. (13) and (14), we may inquire, within a perturbation-theoretic framework, about the effects of directionality on the modal transfer. We may substitute the linear solutions (16) into the right hand sides of eqs. (15) and proceed iteratively to calculate the first nonlinear correction to the linear fields. Inspection of (15) immediately shows that there is no net coupling between the right-travelling waves with each other or the left travelling waves with each other. The only non-zero couplings are between right and left travelling waves.

To resonate effectively with a third, initially-unexcited Fourier mode, there are matching conditions on both frequency and wavenumber which must be met. These are very restrictive when it is taken into consideration that one interacting wave must be right travelling and the other left travelling. If the two waves have wavenumbers  $\vec{k}_1$ ,  $\vec{k}_2$ , the conditions that they be able to excite a third wave resonantly with wavenumber  $\vec{k}_3$  are that  $\vec{k}_3 \cdot (\vec{x} + \vec{B}_0 t) = \vec{k}_1 \cdot (\vec{x} + \vec{B}_0 t) + \vec{k}_2 \cdot (\vec{x} - \vec{B}_0 t)$ , or

$$\begin{aligned} \vec{k}_3 &= \vec{k}_1 + \vec{k}_2 \\ \pm \omega(\vec{k}_3) &= \omega(\vec{k}_1) - \omega(\vec{k}_2) \end{aligned} \tag{17}$$

Since  $\omega(\vec{k}) = \vec{k} \cdot \vec{B}_0$ , eqs. (17) have a solution only if either  $\omega(\vec{k}_1) = 0$  or  $\omega(\vec{k}_2) = 0$ , so that either  $\vec{k}_1$  or  $\vec{k}_2$  has zero component along  $\vec{B}_0$ .

Thus, a three-wave resonant interaction can result in the excitation of a wave with a larger value of  $|k_y|$  than that of either of the other two, but never with a larger value of  $|k_x|$ . It is clear that excitations

may readily transfer energy by this process in the perpendicular direction in  $\vec{k}$  space but not in the parallel one.

An initially isotropic distribution in  $k$  space elongates in the perpendicular direction until something stops the migration to larger  $|k_y|$ . In the present computation, that is either  $k_d$  or, for the truncated non-dissipative model,  $k_{\max}$ . In the latter case, eventual isotropization occurs as a consequence of higher order processes. In the presence of finite dissipative decay, the anisotropy persists, as in Figure 18.

The above-described mechanism seems to be responsible for the observed anisotropy of magnetic fluctuations in toroidal devices. For a given level of excitations,  $k_d$  increases as  $\nu$  and  $\eta$  decrease, so the effect should be most pronounced at high Reynolds numbers. The independence of further increases in  $B_0$ , beyond a certain modest level, must simply mean that transfer in the parallel  $\vec{k}$ -space direction has been effectively frozen relative to the transfer perpendicular to  $\vec{B}$  beyond a value of  $B_0$  just a few times the mean fluctuating field strength.

The natural directions into which these investigations can be taken are to some degree obvious. First, considerably higher Reynolds numbers, with their necessarily higher spatial resolution, could be investigated. Second, spatially inhomogeneous vacuum fields could be added to ascertain the effects of mean field curvature on the anisotropy. Finally, the effects of the mean fields on the small scales need to be ascertained: how does  $B_0$  affect current filamentation, x-point behavior, and magnetic re-connection?

APPENDIX A  
ABSOLUTE EQUILIBRIUM ENSEMBLE THEORY

The equations of two-dimensional MHD flow in the presence of a mean magnetic field in the x direction are, again,

$$\frac{\partial \vec{\omega}}{\partial t} = \nabla \psi \times \nabla \omega + \nu \nabla^2 \vec{\omega} + \beta_0 \partial_x \vec{j} + \nabla j \times \nabla a \quad (A1)$$

$$\frac{\partial \vec{a}}{\partial t} = \nabla \psi \times \nabla a + \eta \nabla^2 \vec{a} + \beta_0 \partial_x \vec{\psi} \quad (A2)$$

Here, all dependent variables are functions of x and y, and the vector quantities in A1 and A2 are in the z direction, e.g.,  $\vec{a} = a\hat{z}$ .  $\nu$  and  $\eta$  are the inverses of the fluid and magnetic Reynolds numbers, respectively. Also,  $\nabla = (\partial/\partial x, \partial/\partial y) = (\partial_x, \partial_y)$  here.

In the system where the vorticity  $\omega (= -\nabla^2 \psi)$  and vector potential a (where the current  $j = -\nabla^2 a$ ) are periodic in a two-dimensional box of side length  $2\pi$ , there exist certain quantities which remain constant during the time evolution of the fields  $\omega$  and a (according to A1 and A2). To determine these constants of motion we define the spatial average of a quantity q to be  $[q]$  where

$$[q] = \frac{1}{(2\pi)^2} \iint q \, dx \, dy \quad (A3)$$

Since the fields  $\omega$  and a, as well as  $\psi$  and j and the velocity  $\vec{v} = -\hat{z} \times \nabla \psi$  and magnetic fields  $\vec{B} = -\hat{z} \times \nabla a$  are periodic over the box of side length  $2\pi$ , then the spatial average satisfies the following



$$[q] = [q + \nabla R + \nabla \cdot \vec{S}] \quad (A4)$$

where  $R$  and  $\vec{S}$  are sums and products of the periodic fields and their derivatives. The  $[\nabla R]$  and  $[\nabla \cdot \vec{S}]$  terms represent differences on parallel boundaries and are zero for periodic boundary conditions. They arise, for example, in integration by parts.

Using the relations A1 through A4 it can be shown (after much mathematical manipulation) that the following equations hold.

$$\frac{d}{dt} \left[ \frac{1}{2} (\vec{v}^2 + \vec{B}^2) \right] = -[\nu \omega^2 + \eta j^2] \quad (A5)$$

$$\frac{d}{dt} [\vec{a} \cdot \vec{\omega}] = -(\nu + \eta) [\vec{\omega} \cdot \vec{j}] \quad (A6)$$

$$\frac{d}{dt} \left[ \frac{1}{2} a^2 \right] = -\eta [\vec{B}^2] + B_0 [a \cdot \nabla \times \tau] \quad (A7)$$

The quantity  $[\frac{1}{2} (\vec{v}^2 + \vec{B}^2)] = E$ , is the total energy,  $\frac{1}{2} [\vec{a} \cdot \vec{\omega}] = P$ , is the "cross-helicity" and  $[\frac{1}{2} a^2] = A$  is one half the mean square vector potential. (These are the "rugged" invariants of 2-D MHD flow; for further discussion, please see Kraichnan and Montgomery, 1980. For a discussion of 3-D rugged invariants, see Matthaeus and Goldstein, 1982.)

It is apparent from A5, A6, and A7 that if our periodic system is inviscid (i.e.,  $\nu = \eta = 0$ ) then  $E$  and  $P$  are constants of the motion. Furthermore, if there is also no mean magnetic field ( $B_0 = 0$ ), then  $A$  is also a constant of the motion. When the periodic fields are represented by truncated Fourier expansions, an interesting statistical system

results. Using the expansions

$$\omega(\vec{x}, t) = \sum_{\vec{k}} \omega(\vec{k}, t) \exp(i\vec{k} \cdot \vec{x}) \quad (\text{A8})$$

$$a(\vec{x}, t) = \sum_{\vec{k}} a(\vec{k}, t) \exp(i\vec{k} \cdot \vec{x}) \quad (\text{A9})$$

The equations of motion A1 and A2 can be transformed to k-space forms, (similar to those of Kraichnan and Montgomery (1980)):

$$\dot{\omega}(\vec{k}) = \sum_{\vec{p}+\vec{q}=\vec{k}} M_1(\vec{q}, \vec{p}) [\omega(\vec{q})\omega(\vec{p}) - j(\vec{q})j(\vec{p})] - \nu k^2 \omega(\vec{k}) + i k_x B_0 j(\vec{k}) \quad (\text{A10})$$

$$\dot{j}(\vec{k}) = \sum_{\vec{p}+\vec{q}=\vec{k}} M_2(\vec{q}, \vec{p}) [j(\vec{q})\omega(\vec{p}) - j(\vec{p})\omega(\vec{q})] - \eta k^2 j(\vec{k}) + i k_x B_0 \omega(\vec{k}) \quad (\text{A11})$$

where

$$M_1(\vec{q}, \vec{p}) = \frac{1}{2} \hat{z} \cdot (\vec{q} \times \vec{p}) (\rho^{-2} - q^{-2})$$

$$M_2(\vec{q}, \vec{p}) = \frac{1}{2} \hat{z} \cdot (\vec{q} \times \vec{p}) |\vec{p} + \vec{q}|^2 \rho^{-2} q^{-2}$$

and  $j(\vec{k}) = k^2 a(\vec{k})$

It is obvious from A10 and A11 that  $\partial \dot{\omega}(\vec{k}) / \partial \omega(\vec{k}) = 0$  and  $\partial \dot{a}(\vec{k}) / \partial a(\vec{k}) = 0$ . The system thus satisfies a "detailed Liouville Theorem" when  $\nu = \eta = 0$ . Also, Fyfe and Montgomery (1976a) have shown that the various inviscid constants of the motion E, P, and A (if  $B_0 = 0$ ) are still conserved for a truncated system if the system equations and

expansions are properly de-aliased, i.e., if only  $\vec{k}$  such that the condition  $k_{\min} \leq |\vec{k}| \leq k_{\max}$  is constantly adhered to.

This system can be considered a quasi-closed statistical system (particularly the numerical modelling of such a system, since the model system is interacting weakly with the "outside" through round-off error, numerical approximation error, etc.). As discussed by Kraichnan (1975), Fyfe, et al., (1976 a & b) and Kraichnan and Montgomery (1980), the statistical properties of the model system can be described by a canonical distribution function, D,

$$D = C \exp(-\alpha E - \beta P - \gamma A) \quad (A12)$$

where C is a normalizing constant and  $\alpha$ ,  $\beta$  and  $\gamma$  are "inverse temperatures". For the case  $B_0 \neq 0$ , the term  $\gamma A$  does not appear in the exponent of A12.

In the truncated representation, the constants of the motion appear as

$$\begin{aligned} E &= \frac{1}{2} \sum_{\vec{k}} \frac{k \omega^2(\vec{k}) + |j|^2(\vec{k})}{k^2} \\ P &= \frac{1}{2} \sum_{\vec{k}} \omega^*(\vec{k}) j(\vec{k}) / k^2 \\ A &= \frac{1}{2} \sum_{\vec{k}} |j|^2(\vec{k}) / k^4 \end{aligned} \quad (A13)$$

Thus the canonical distribution D in (A12) is a distribution in a phase space whose dimensions correspond to the independent real and imaginary parts of the Fourier coefficients  $\omega(\vec{k})$  and  $j(\vec{k})$ . The normalizing coefficient C in (A12) is determined by requiring

$$\int D \, dV = 1 \quad (A14)$$

where  $dV$  is the hypervolume

$$dV = \prod_{\vec{k}} d\omega_r(\vec{k}) d\omega_i(\vec{k}) dj_r(\vec{k}) dj_i(\vec{k})$$

where the product, again, is over the independent coefficients (i.e., if  $\vec{k}$  is included,  $-\vec{k}$  is not, since  $\omega(\vec{k}) = \omega^*(-\vec{k})$ , etc.); also,  $\omega(\vec{k}) = \omega_r(\vec{k}) + i\omega_i(\vec{k})$ .

Rather than explicitly performing the integration (A14) here (it is essentially the integration of a gaussian distribution) we merely reproduce the result of Fyfe, et al. (1976a):

$$C = \prod_{\vec{k}} C_{\vec{k}} \quad (\text{A15})$$

where

$$C_{\vec{k}} = \frac{(\alpha^2 + \alpha\gamma/k^2 - \beta^2/4)}{\pi k^4} \quad (\text{A15a})$$

As Fyfe, et al (1976a) show, this form of  $C_{\vec{k}}$  allows for the calculation of expectation values of such quantities as  $B^2(\vec{k}) = |\vec{B}(\vec{k})|^2 = k^2 a^2(k) = j^2(k)/k^2$  in the following manner:

$$\begin{aligned} \langle B^2(\vec{k}) \rangle &= \int B^2(\vec{k}) D dV \\ &= \int \int_{-\infty}^{\infty} \frac{j^2(\vec{k})}{k^2} C_{\vec{k}}^{1/2} \exp\left[-\frac{(\alpha + \gamma/k^2 - \beta^2/4\alpha)j^2(\vec{k})}{k^2}\right] dj_r(\vec{k}) dj_i(\vec{k}) \quad (\text{A16}) \\ &= (\alpha + \gamma/k^2 - \beta^2/4\alpha)^{-1} \end{aligned}$$

Similarly, the expectation values of the other individual modal contributions to  $E$ ,  $P$ , and  $A$  (as given in A13) can be determined:

$$\begin{aligned}\langle v^2(\vec{k}) \rangle &= (\alpha + \gamma/k^2) (\alpha^2 + \alpha\gamma/k^2 - \beta^2/4)^{-1} \\ \langle \vec{B}(\vec{k}) \cdot \vec{V}(\vec{k}) \rangle &= -\frac{\beta}{2} (\alpha^2 + \frac{\alpha\gamma}{k^2} - \beta^2/4)^{-1}\end{aligned}\tag{A17}$$

Using A13, A16 and A17 yields the following expressions which relate the expectation values of E, P, and A to the inverse temperatures  $\alpha$ ,  $\beta$  and  $\gamma$ :

$$\begin{aligned}\langle E \rangle &= \frac{1}{2} \sum_{\vec{k}} \frac{(2\alpha + \gamma/k^2)}{(\alpha^2 + \alpha\gamma/k^2 - \beta^2/4)} \\ \langle P \rangle &= \frac{1}{2} \sum_{\vec{k}} \frac{-\beta/2}{(\alpha^2 + \alpha\gamma/k^2 - \beta^2/4)} \\ \langle A \rangle &= \frac{1}{2} \sum_{\vec{k}} \frac{\alpha/k^2}{(\alpha^2 + \alpha\gamma/k^2 - \beta^2/4)}\end{aligned}\tag{A18}$$

(sum over all available modes.) The expectation values for the kinetic and magnetic energies can also be given:

$$\begin{aligned}\langle E_v \rangle &= \frac{1}{2} \sum_{\vec{k}} \frac{\alpha + \gamma/k^2}{(\alpha^2 + \alpha\gamma/k^2 - \beta^2/4)} \\ \langle E_B \rangle &= \frac{1}{2} \sum_{\vec{k}} \frac{\alpha}{(\alpha^2 + \alpha\gamma/k^2 - \beta^2/4)}\end{aligned}\tag{A19}$$

Many interesting relationships can be derived from A18 and A19. For example, consider the following:

$$\begin{aligned}\alpha \langle E \rangle + \beta \langle P \rangle + \gamma \langle A \rangle &= \frac{1}{2} \sum_{\vec{k}} \frac{2\alpha^2 + \alpha\gamma/k^2 - \beta^2/2 + \gamma\alpha/k^2}{(\alpha^2 + \alpha\gamma/k^2 - \beta^2/4)} \\ &= \sum_{\vec{k}} 1 = N\end{aligned}\tag{A20}$$

where  $N$  is the total number of modes (both dependent and independent) in the range  $k_{\min} \leq |\vec{k}| \leq k_{\max}$ . Thus, the distribution function  $D$ , as given in A12, when evaluated at the expectation values of  $E$ ,  $P$ , and  $A$  can be written:

$$\begin{aligned} \bar{D} &= C \exp(-N) \\ &= \exp \left[ \sum_{\vec{k}} \ln(\alpha^2 + \alpha \gamma / k^2 - \beta^2 / 4) - \sum_{\vec{k}} \ln(\pi^2 k^4) - N \right] \end{aligned} \quad (\text{A21})$$

In A21 the sums are over only the independent modes, i.e., only over half the total number of  $k$ 's. The inverse temperatures  $\alpha$ ,  $\beta$  and  $\gamma$  appearing in (A21) are related to the expectation values of  $E$ ,  $P$ , and  $A$  through A18.

Suppose now that we wrote the distribution A12 with the values of  $E$ ,  $P$ , and  $A$  which we know to be constant (i.e., constants of the motion) for our model system. Call these constant values of  $E$ ,  $P$ , and  $A$   $\bar{E}$ ,  $\bar{P}$ , and  $\bar{A}$ , respectively. Then the distribution A12 can be written

$$\begin{aligned} D' &= C \exp[-\alpha \bar{E} - \beta \bar{P} - \gamma \bar{A}] \\ &= \exp [\ln C - \alpha \bar{E} - \beta \bar{P} - \gamma \bar{A}] \end{aligned} \quad (\text{A22})$$

Since this is the value of the distribution function of a system in equilibrium we expect the system to be in a state of maximum probability. Thus, we require  $D'$  in A22 to be at a maximum value for a given set of constants of the motion  $E$ ,  $P$ , and  $A$ . Since the free parameters in A22 are  $\alpha$ ,  $\beta$  and  $\gamma$ , we require that they be chosen so that  $D'$  is a maximum. This is the same as requiring that the argument of the exponential in A22 be a minimum with respect to  $\alpha$ ,  $\beta$ , and  $\gamma$ ; that is, the

partial derivatives (with respect to  $\alpha$ ,  $\beta$ ,  $\gamma$ ) of the argument of the exponential must be zero; which leads to the following relations:

$$\begin{aligned}\bar{E} &= \frac{\partial}{\partial \alpha} \ln C = \frac{1}{2} \sum_k \frac{2\alpha + \gamma/k^2}{(\alpha^2 + \alpha\gamma/k^2 - \beta^2/4)} \\ \bar{P} &= \frac{\partial}{\partial \beta} \ln C = \frac{1}{2} \sum_k \frac{-\beta/2}{(\alpha^2 + \alpha\gamma/k^2 - \beta^2/4)} \\ \bar{A} &= \frac{\partial}{\partial \gamma} \ln C = \frac{1}{2} \sum_k \frac{\alpha/k^2}{(\alpha^2 + \alpha\gamma/k^2 - \beta^2/4)}\end{aligned}\tag{A23}$$

Here the sums are again over all allowable modes. Comparing A23 with A18, we see that the inverse temperatures  $\alpha$ ,  $\beta$ , and  $\gamma$  determined from the expectation values of  $E$ ,  $P$ , and  $A$  are just those values of  $\alpha$ ,  $\beta$ , and  $\gamma$  corresponding to the most probable equilibrium state (or states), a result which is consistent with canonical distribution theory.

A useful quantity in the absolute equilibrium ensemble theory of two dimensional MHD systems is  $R$ , the ratio between the magnetic and kinetic energies:  $R = \langle E_B \rangle / \langle E_v \rangle$ . Since the total energy is  $\langle E \rangle = \langle E_B \rangle + \langle E_v \rangle$ ,  $\langle E_B \rangle$  and  $\langle E_v \rangle$  are related to  $\langle E \rangle$  through  $R$  as follows:

$$\begin{aligned}\langle E_B \rangle &= \frac{R}{1+R} \langle E \rangle \\ \langle E_v \rangle &= \frac{1}{1+R} \langle E \rangle\end{aligned}\tag{A24}$$

These relations can be used with A18 and A19 to produce the following relations among  $\langle E \rangle$ ,  $\langle P \rangle$ ,  $\langle A \rangle$ ,  $R$  and  $\alpha$ ,  $\beta$ , and  $\gamma$  (for some economy of notation  $\bar{E}$ ,  $\bar{P}$ , and  $\bar{A}$  will be utilized in place of  $\langle E \rangle$ ,  $\langle P \rangle$  and  $\langle A \rangle$ ):

$$\alpha \bar{E} + \beta \bar{P} + \gamma \bar{A} = N\tag{A25}$$

$$\alpha \bar{E} \left( \frac{1-R}{1+R} \right) - \gamma \bar{A} = 0 \quad (\text{A26})$$

$$\frac{\alpha \bar{E}}{1+R} \left( 1 - \beta^2 / 4 \alpha^2 \right) = \frac{N}{2} \quad (\text{A27})$$

here  $N$  is, again, the total number of  $\vec{k}$ 's in the range  $k_{\min} \leq |\vec{k}| \leq k_{\max}$ .

The set of equations A25, A26 and A27 can be solved for the inverse temperatures  $\alpha$ ,  $\beta$ , and  $\gamma$  in terms of the constants  $\bar{E}$ ,  $\bar{P}$ ,  $\bar{A}$  and  $N$ , and the parameter  $R$ . The result is

$$\begin{aligned} \alpha &= N(1+R) (2 \bar{E} Z)^{-1} \\ \beta &= -N \bar{P} (1+R)^2 (\bar{E}^2 R Z)^{-1} \\ \gamma &= N(1-R) (2 \bar{A} Z)^{-1} \end{aligned} \quad (\text{A28})$$

where  $Z$ , the common factor in the denominators of A28, is

$$Z = 1 - \frac{1}{R} \left[ \frac{\bar{P}(1+R)}{\bar{E}} \right]^2 \quad (\text{A29})$$

The expressions in A28 can also be inverted to give  $E$ ,  $P$ , and  $A$  in terms of  $\alpha$ ,  $\beta$ ,  $\gamma$ ,  $N$ ,  $R$ . These expressions are, for completeness,

$$\begin{aligned} \bar{E} &= N(1+R) (2 \alpha \delta)^{-1} \\ \bar{P} &= -N \beta (4 \alpha^2 \delta)^{-1} \\ \bar{A} &= N(1-R) (2 \gamma \delta)^{-1} \end{aligned} \quad (\text{A30})$$

where

$$\delta = 1 - \frac{\beta^2}{4 \alpha^2}$$

The results up to this point have primarily focused on the case when  $B_0 = 0$ . When  $B_0 \neq 0$ ,  $A$  is no longer a constant of the motion, so



that the term  $\gamma A$  no longer appears in the argument of the distribution function. Thus, all the formulas derived so far reduce to those for  $B_0 \neq 0$ , i.e., two constants of the motion by setting  $\gamma A = 0$  wherever it appears. Doing this in A28 yields the equilibrium inverse temperatures  $\alpha$  and  $\beta$  when  $B_0 \neq 0$ , as well as a requirement on the ratio  $R$ :

$$\begin{aligned} R &= 1 \\ \alpha &= \frac{N}{\bar{E}} [1 - 4(\bar{P}/\bar{E})^2]^{-1} \\ \beta &= -4N\bar{P} [\bar{E}^2 - 4\bar{P}^2]^{-1} \end{aligned} \tag{A31}$$

Also, when  $B_0 \neq 0$ , it is clear from A16 and A17 that when terms containing  $\gamma$  are removed from the individual modal expectation values, these values are all equal. Thus, the expected energy and cross-helicity spectra are equi-partitioned for  $B_0 \neq 0$ .

Now to calculate the equilibrium entropy. Using the classical definition, we have

$$\begin{aligned} S &= - \int D \ln D \, dV \\ &= \alpha \bar{E} + \beta \bar{P} + \gamma \bar{A} - \ln C \end{aligned} \tag{A32}$$

where A12, A14 and A15 have been utilized, and the multiplicative Boltzmann constant has been omitted. If we require the equilibrium entropy to be an extremum with respect to  $\alpha$ ,  $\beta$ , and  $\gamma$  we get the relations A23. (The extremum is, in fact, a minimum; Khinchin, 1949, discusses this procedure for the case when only  $E = \text{const.}$ )

These equations, however, were seen to result from requiring the value of the distribution function to be a maximum when the system

was in an equilibrium state. Indeed, Liouville's Theorem tells us that as the system point moves about in phase space, this value will remain constant. Thus, the system stays in those areas of its phase space where the density of states, and, hence, the entropy is greatest.

An interesting formal parameterization of the entropy in terms of the ratio between the magnetic and kinetic energies of the system can be effected through the use of  $\alpha(R)$ ,  $\beta(R)$  and  $\gamma(R)$ . It must be stressed, however, that this parameterization has no inherent physical meaning because the entropy is a time averaged quantity while the ratio  $R$  is a temporally evolving quantity which fluctuates about some average value.

When the expressions for the inverse temperatures  $\alpha$ ,  $\beta$ , and  $\gamma$  as given in (A28) are placed in the expression for the entropy (A32) through the use of (A15) and (A20) they yield an expression for the expected equilibrium value of the entropy in terms of  $R$ :

$$\begin{aligned} S(R) &= N - \ln C \\ &= N - \sum_{\vec{k}} \ln C_{\vec{k}} \end{aligned} \tag{A33}$$

where

$$C_{\vec{k}} = \frac{C_1^2 [R^2(1+R)^2 + C_3(1-R^2)R^2 - C_2(1+R)^4]}{\pi^2 k^4 [R - C_2(1+R)^2]^2}$$

and

$$C_1 = \frac{N}{2\bar{E}}, \quad C_2 = \frac{\bar{p}^2}{\bar{E}^2}, \quad C_3 = \frac{\bar{E}}{A k^2}$$

and the sum is over the independent  $\vec{k}$  modes only.

The inverse temperatures  $\alpha$ ,  $\beta$ , and  $\gamma$  can now be found by minimizing  $S(R)$ , i.e., by finding the real value of  $R$  so that

$$\frac{d}{dR} (S(R)) = 0 \quad (A34)$$

This is, of course equivalent to solving the equations (A23) (which do not contain  $R$  explicitly). The advantage of using (A33) is that it is a function of a single variable  $R$ . This allows  $S(R)$  to be quickly plotted by a computer graphics routine, revealing the approximate location of the value of  $R$  which minimizes the equilibrium entropy. If this value is not sufficiently accurate, it can be used as a very accurate initial value for use in an algorithm which numerically solves for a more accurate value. Once a suitably accurate value of  $R$  such that (A34) is solved sufficiently well,  $\alpha(R)$ ,  $\beta(R)$  and  $\gamma(R)$  can be determined. Then, by utilizing (A16) and (A17), theoretical values of the modal expectation values of the kinetic and magnetic energies can be calculated and compared with the numerically determined values (as is done in several of the directionally averaged modal spectra graphs presented in this paper).

The expression for the entropy given by (A33) is a rather complicated function of  $R$ . It would be nice to fully analyze the algebraic structure of the various parts of (A33) in order to fully characterize the solutions to (A34). To do this completely is beyond the scope of the present work. A simpler case of the general expression (A33) can be considered here, and this should hopefully illuminate general aspects of the complete solution.

Consider then the case where the cross-helicity  $\bar{P} = 0$ , i.e.,  $C_2 = 0$ . The entropy in this case is

$$S(R) = N - \sum_k \ln \left[ \frac{C_3^2 (1+R)}{\pi^2 k^4} \right] - \sum_k \ln [1+R+C_3(1-R)] \quad (A35)$$

Since the values of  $R$  are always non-negative, the first two terms in (A35) always remain real. The third term, however, becomes imaginary whenever  $R$  is such that

$$1 + R + C_3(1-R) < 0$$

which leads to the conditions for  $S(R)$  to be real:

$$R < \frac{C_3 + 1}{C_3 - 1} \quad (C_3 > 1) \quad (A36)$$

$$R > -\frac{1+C_3}{1-C_3} \quad (C_3 < 1) \quad (A37)$$

Since  $R \geq 0$ , (A37) is always satisfied and we need not concern ourselves with cases when  $C_3 < 1$ . For cases where  $C_3 > 1$ , i.e., for  $k^2 < \frac{\bar{E}}{\bar{A}}$ , we see that  $C_3 = \bar{E}/\bar{A}$ , ( $k^2 = 1$ ), puts a limit on the maximum value  $R$  can be before the entropy gains an imaginary part. Thus, for the case  $\bar{P} = 0$ , we must have

$$0 < R < \frac{\bar{E} + \bar{A}}{\bar{E} - \bar{A}} \quad (A38)$$

This limits us to only a bounded range of  $R$  to search through graphically for the minimum of  $S(R)$  (when  $\bar{P} = 0$ ). Since  $\bar{E} \gg \bar{A}$  in most of the cases studied herein (as determined by the initial conditions), the range of  $R$  to be considered is not very great.

For the case  $\bar{P} = 0$ , the condition (A34) takes the form

$$(C_3 = E/Ak^2)$$

$$\sum_{\vec{k}} \left[ 1 + \frac{\bar{E}}{A k^2} \frac{(1-R)}{(1+R)} \right]^{-1} = -N \quad (\text{A39})$$

(sum over all  $\vec{k}$  modes.)

For the general case when  $\bar{P} \neq 0$ , it is expected the qualitative features discussed in the  $\bar{P} = 0$  case remain. There should be a minimum value of  $R$  above which the equilibrium value of  $R$  will not lie. It is also expected that there will be only one real minimum in the allowed range of  $R$ . This has proved true for graphical analysis of all the runs specifically considered herein.

## APPENDIX B

### RANDOMNESS AND ERGODICITY IN MHD MODEL SYSTEMS

In this appendix, some interesting topics, whose systematic investigation is beyond the scope of the present work, will be touched upon briefly. Specifically, these topics are the extent to which randomness and ergodicity are to be found in two-dimensional models of MHD flows.

Kells and Orszag (1978) have investigated randomness in two dimensional models of inviscid Navier-Stokes turbulence and found that the behavior of model systems was random as long as the number of Fourier modes was large enough ( $\geq 20$ ) to insure that every mode was involved in non-trivial non-linear interactions. Here, the number of modes (716) is sufficiently high, so that the problem of too low an order is avoided. In addition, the absolute equilibrium (canonical) ensemble formulation presupposes the modal amplitudes to be random variables, with a particular distribution function. The fact that the numerical results match so well with the canonical ensemble predictions is again a strong indication that the assumption of randomness is a good one.

A qualitative appreciation of the randomness present in the model system used in this work can be seen in Figures 23 and 24. In these figures the real part of a complex mode is plotted versus its imaginary part, as a function of time; i.e., points corresponding to 0.5 units of time have been connected by straight line segments to show the

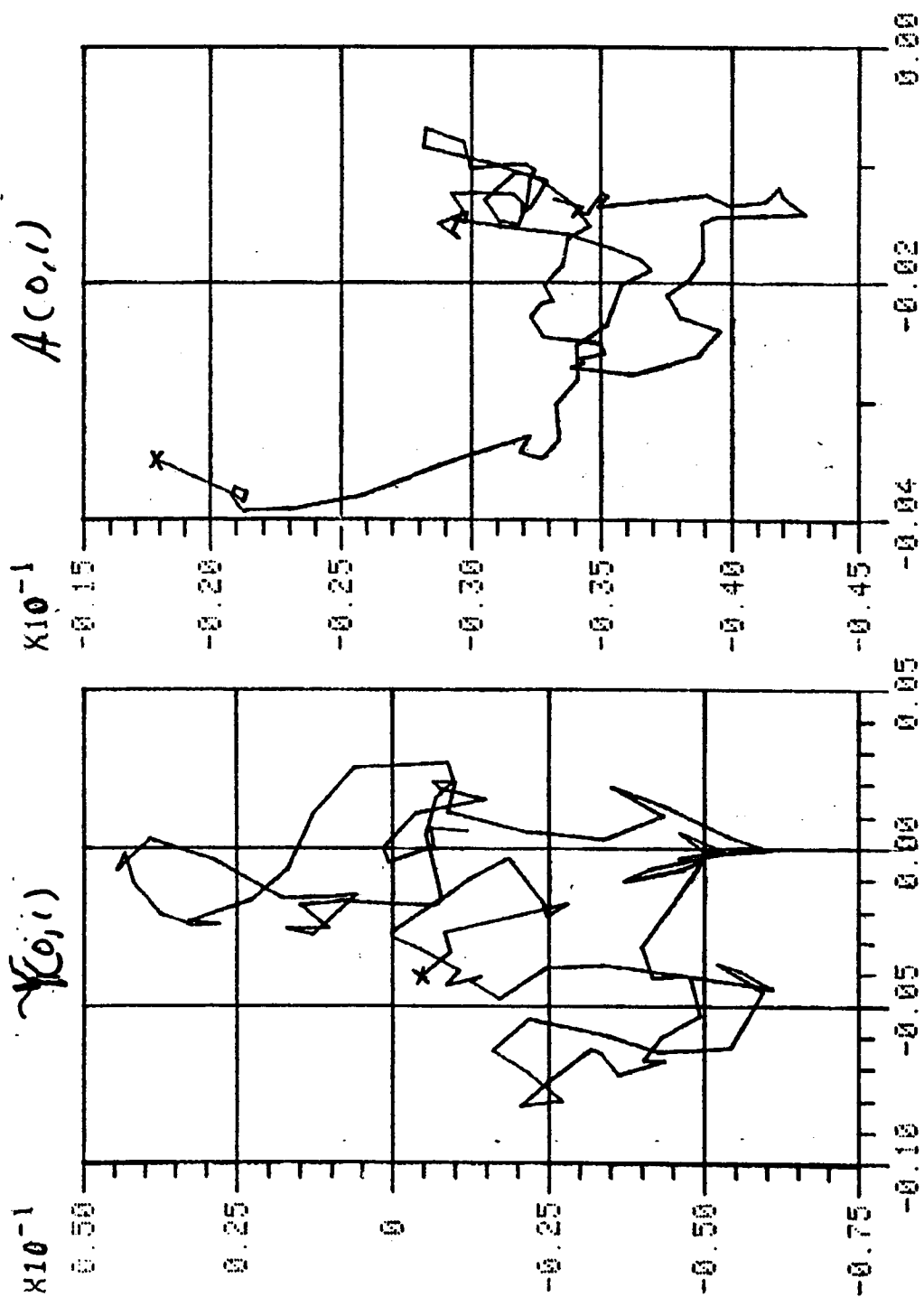


Figure 23.- Typical phase trajectories for  $\vec{k} = (0,1)$ ,  $B_0 = 0$ .

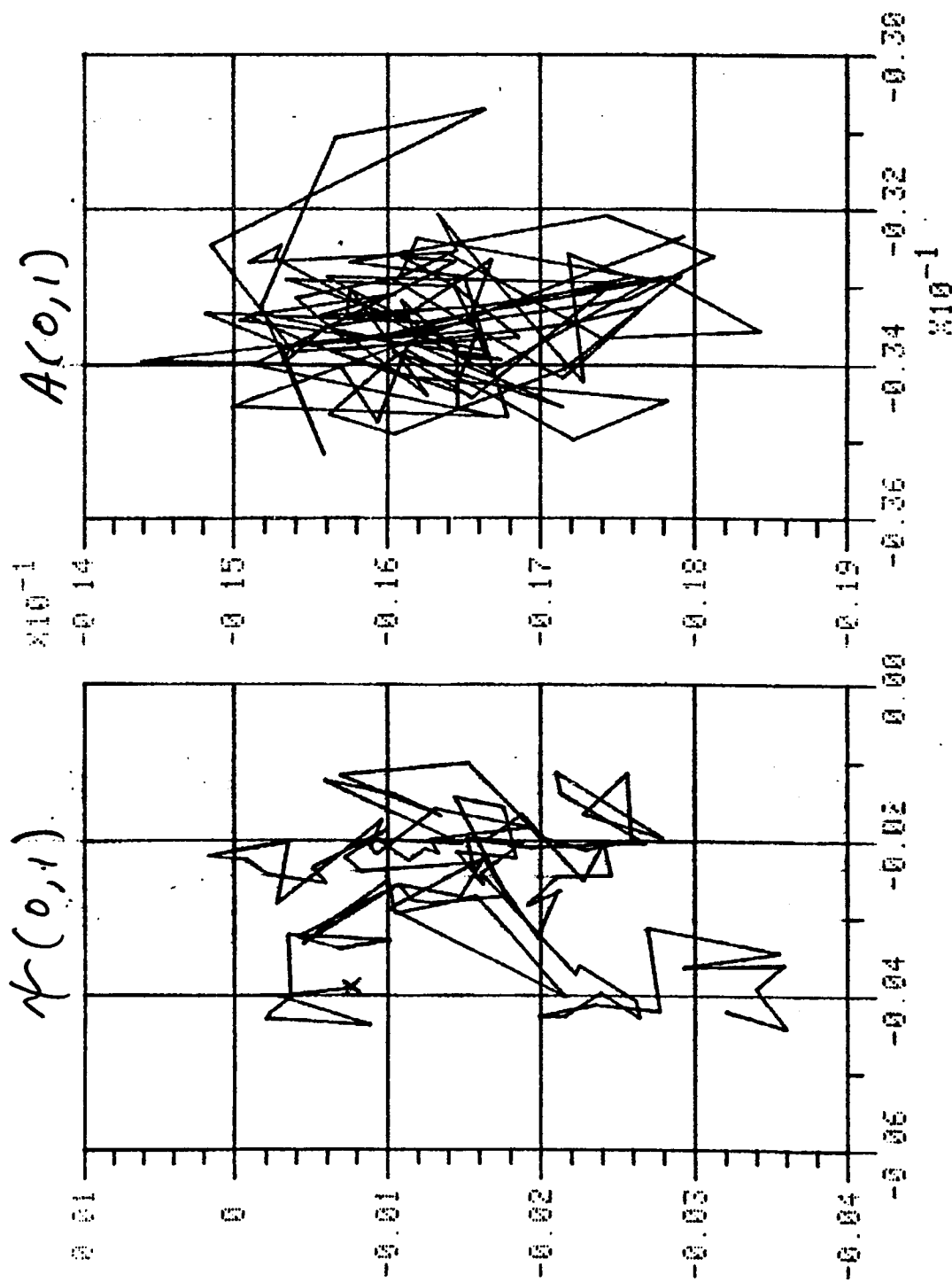


Figure 24.- Typical phase trajectories for  $\vec{k} = (0,1)$ ,  $B_0 = 1$ .



time behavior of the mode  $\vec{k} = (0,1)$ . Thus, the trajectories of both  $\Psi(\vec{k},0)$  and  $A(\vec{k})$  for  $\vec{k} = (0,1)$  are shown for 50 units of time. The starting points (when distinguishable) have been denoted by an "x". These modes are part of an inviscid run which had  $E = 1.0163$ ,  $P = .004144$ ,  $A = .01376$  and all the kinetic and magnetic modes initially equipartitioned with random phases; time step size =  $1/256$  total number of time steps = 12800, and  $k_{\max} = 16$ . For Figure 23,  $B_0 = 0$ ; for Figure 24,  $B_0 = 1.0$ . The phase point appears to be taking a random walk through phase space.

We may also inquire as to the amount or randomness during the evolution of a dissipative case. Again, a qualitative feel can be achieved by considering Figures 25 through 32, which correspond to runs A9 ( $B_0 = 0$ ) and A15 ( $B_0 = 2.0$ ; see Table 2 for more details). Although these trajectories are plotted for only 5 time units, the randomness is again apparent.

The ergodicity of the two dimensional system, i.e., the equivalence of time and ensemble averages, again seems to be a good assumption. This is clear from Figures 9 through 12, where a comparison between time and ensemble averages is made. There is one point here that needs further comment, however.

This point is that the time averages, although close to the ensemble averages, differ slightly from them, in that the time averages appear to contain "spikes". These spikes may arise because not enough time has been allowed for the time averaging (the averages were taken

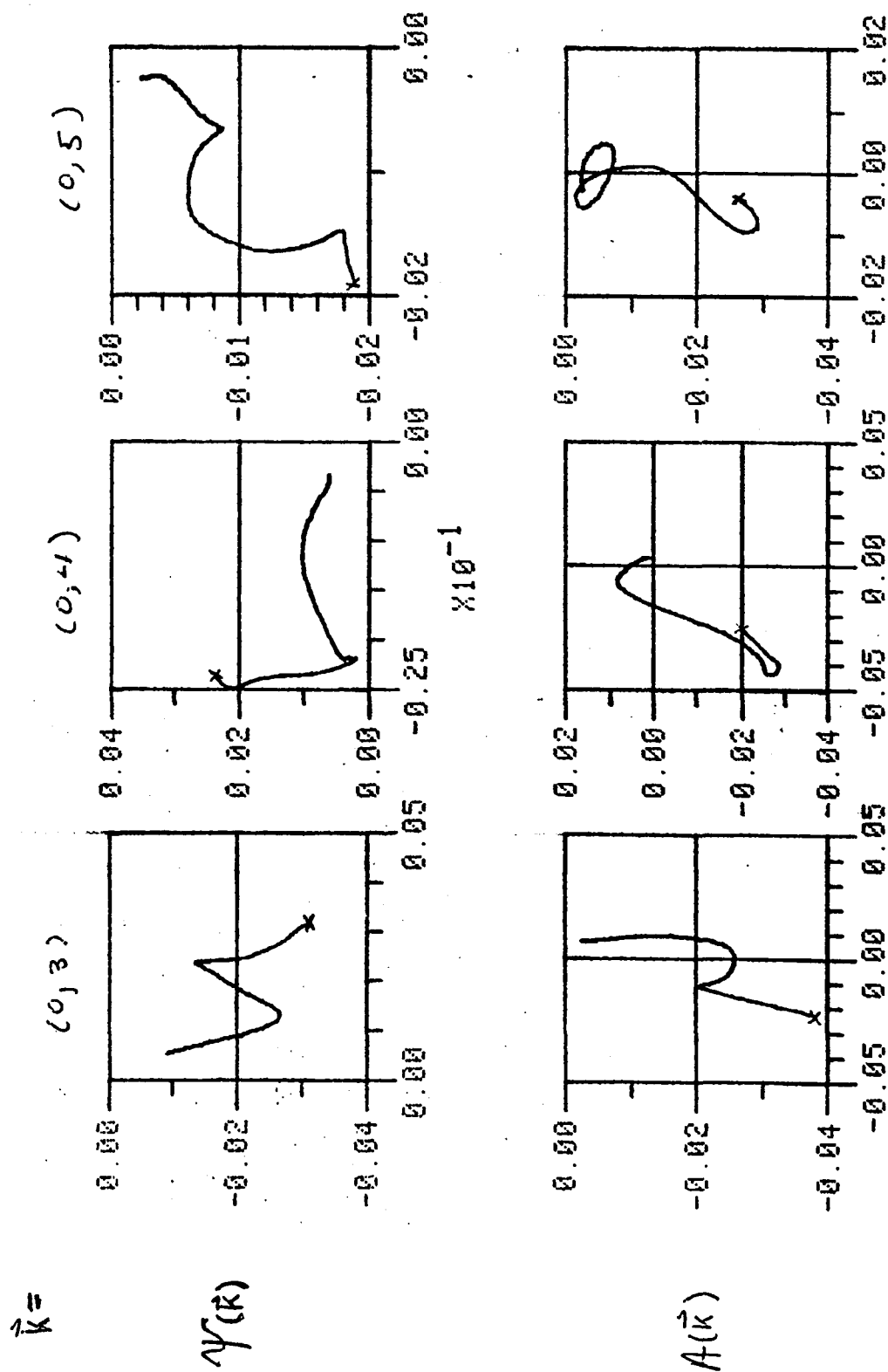


Figure 25.- Modal trajectories for run A9 ( $B_0 = 0$ ,  $\mu = \nu = .01$ ) for  $\vec{k} = (0,3)$ ,  $(0,4)$ ,  $(0,5)$ .

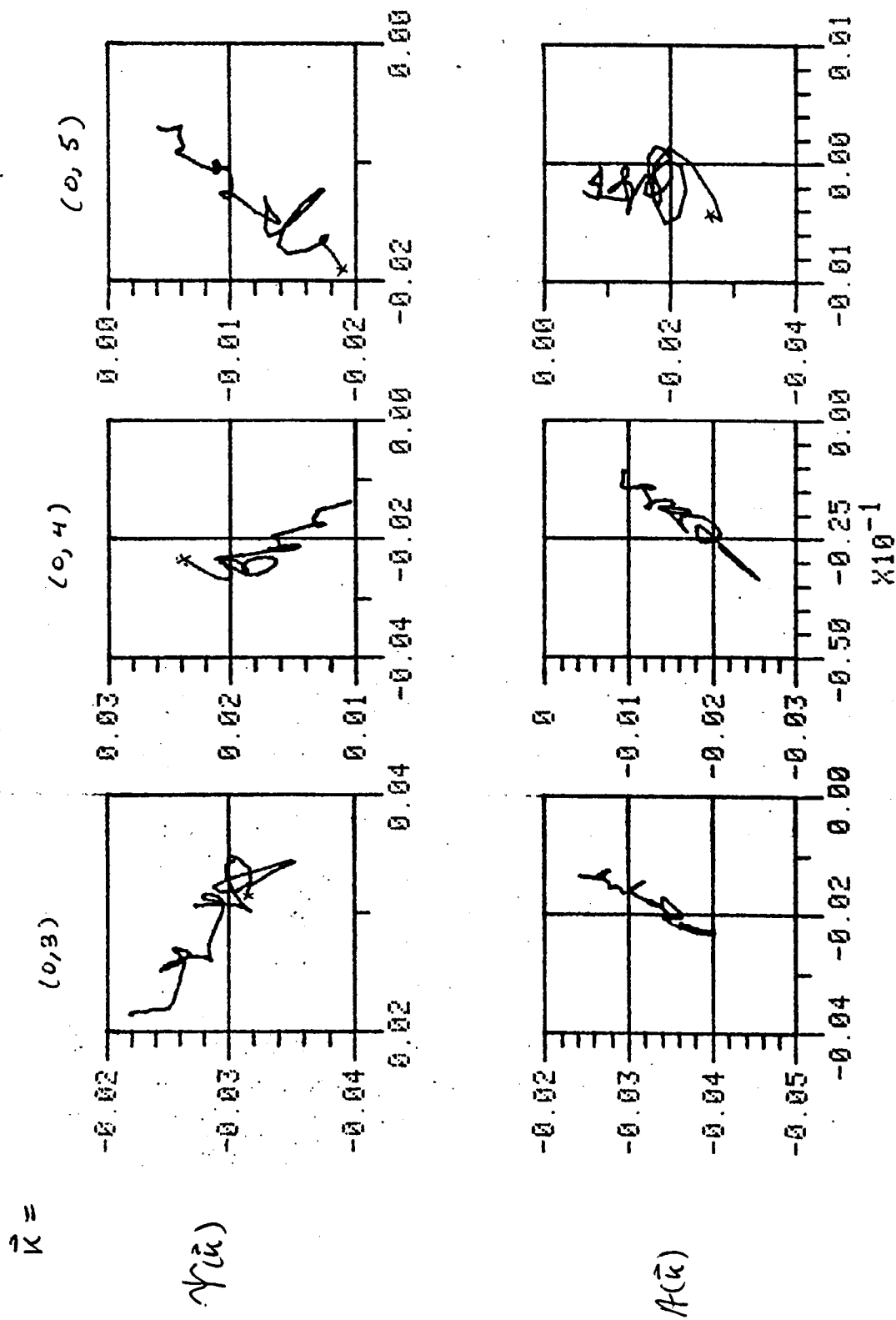


Figure 26.- Modal trajectories for run A15 ( $B_0 = 2$ ,  $\mu = \nu = .01$ ) for  $\vec{k} = (0,3), (0,4), (0,5)$ .

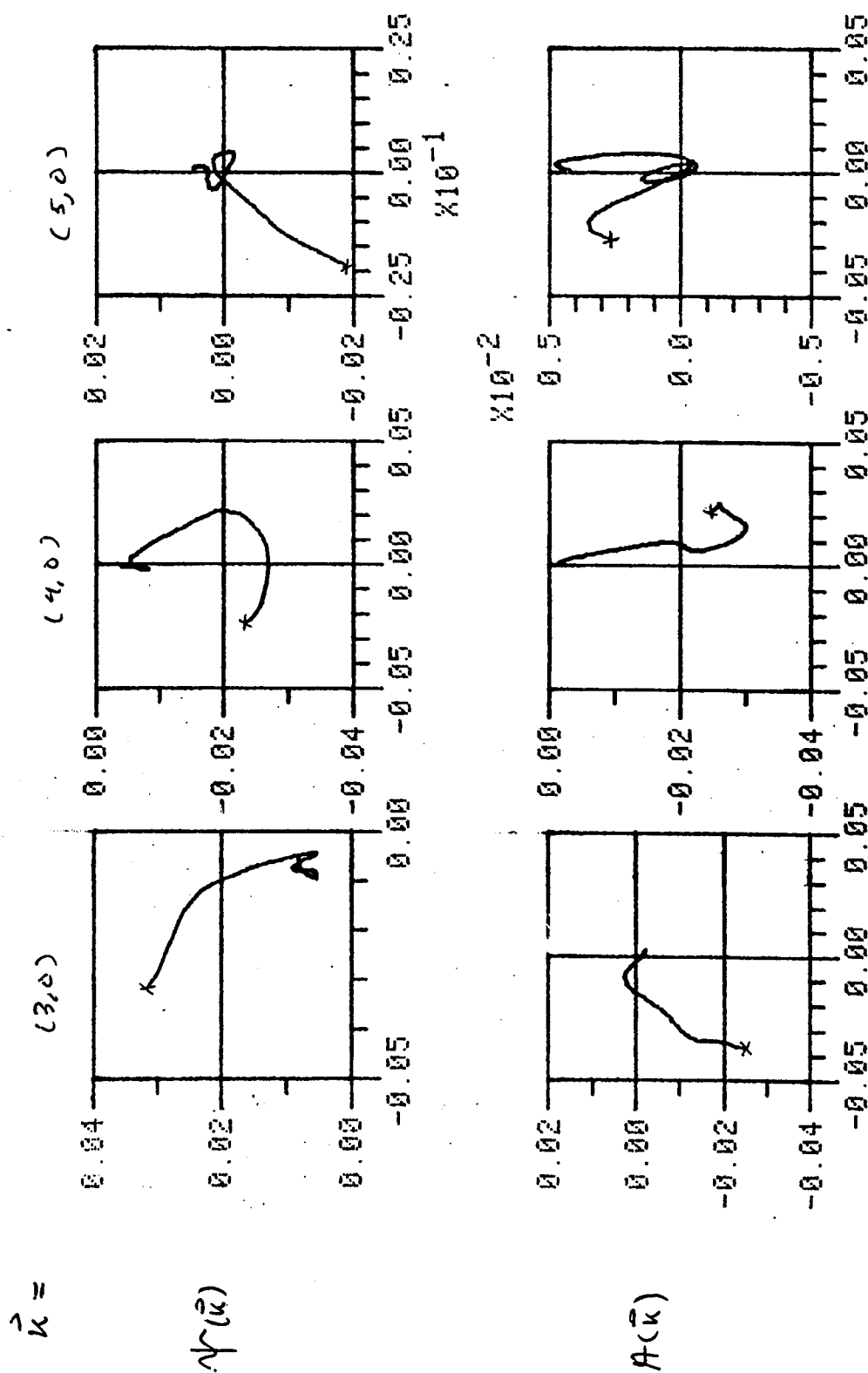


Figure 27.- Modal trajectories for run A9 ( $B_0 = 0$ ,  $\mu = \nu = .01$ ) for  $\vec{k} = (3,0)$ ,  $(4,0)$ ,  $(5,0)$ .

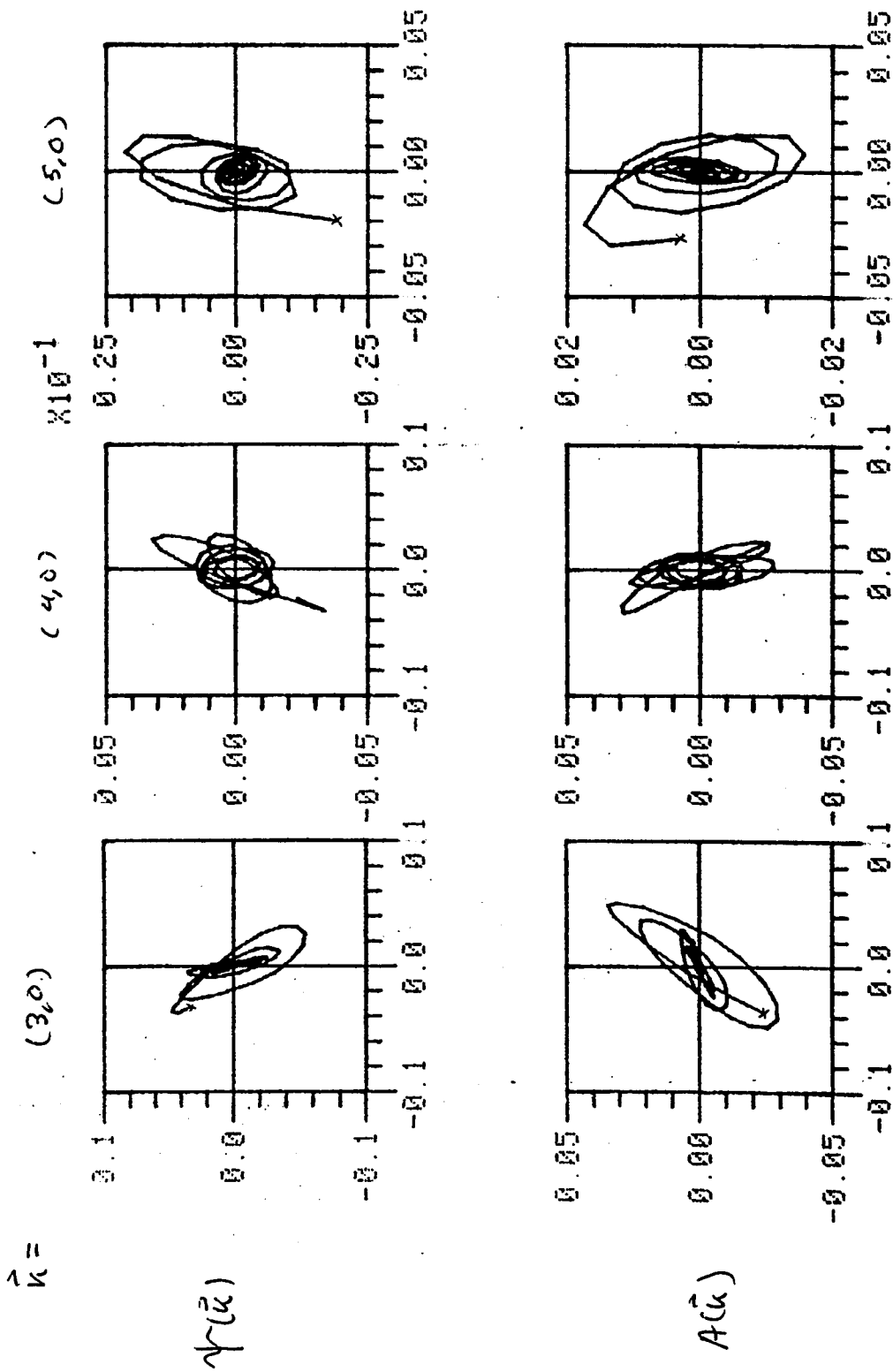


Figure 28.- Modal trajectories for run A15 ( $B_0 = 2$ ,  $\mu = \nu = .01$ ) for  $\vec{k} = (3,0), (4,0), (5,0)$ .

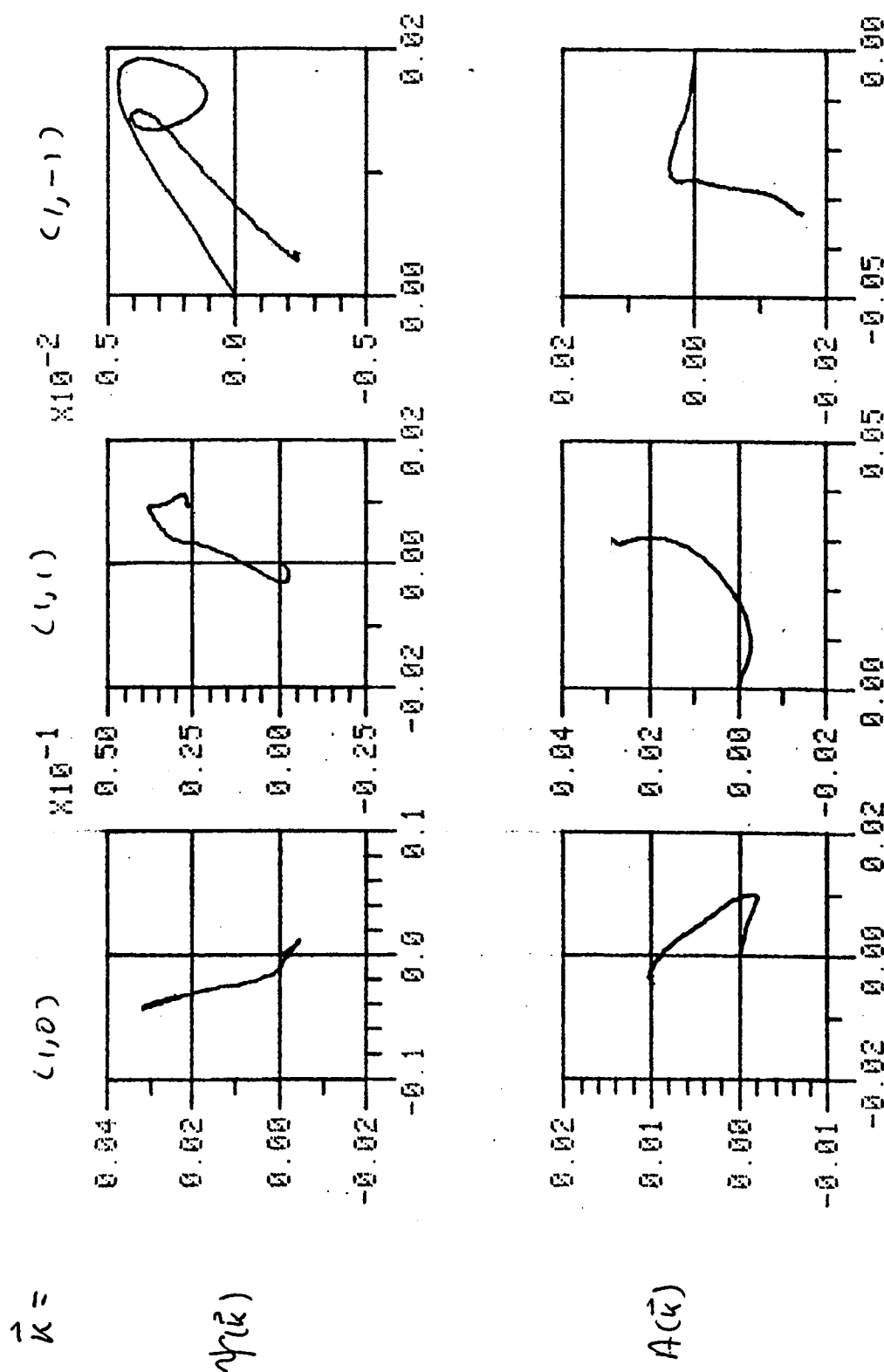


Figure 29.- Modal trajectories for run A9 ( $B_0 = 0$ ,  $\mu = \nu = .01$ ) for  $\vec{k} = (1,0), (1,1), (1,-1)$ .

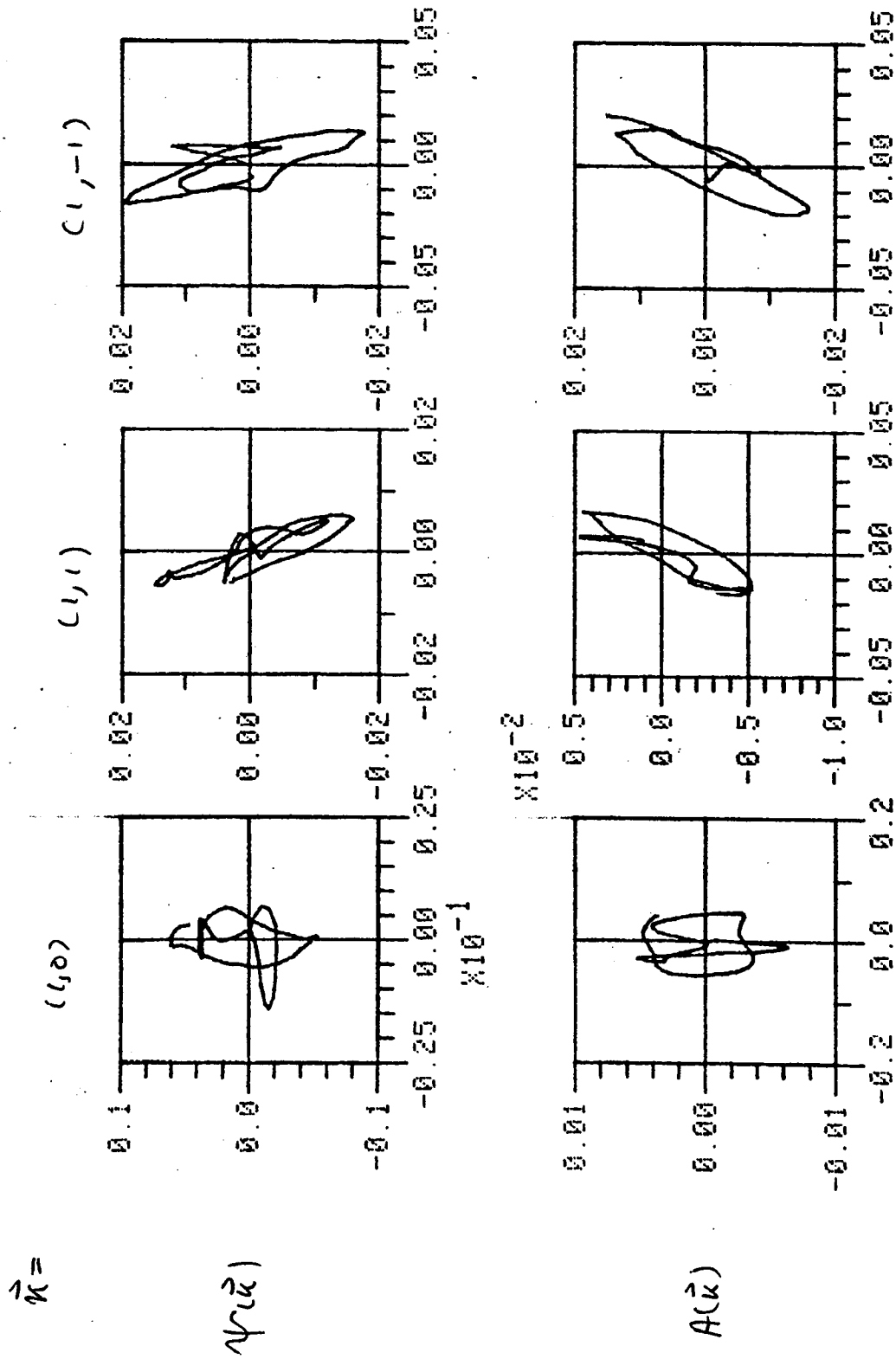


Figure 30.- Modal trajectories for run A15 ( $B_0 = 2$ ,  $\mu = \nu = .01$ ) for  $\vec{k} = (1,0)$ ,  $(1,1)$ ,  $(1,-1)$ .

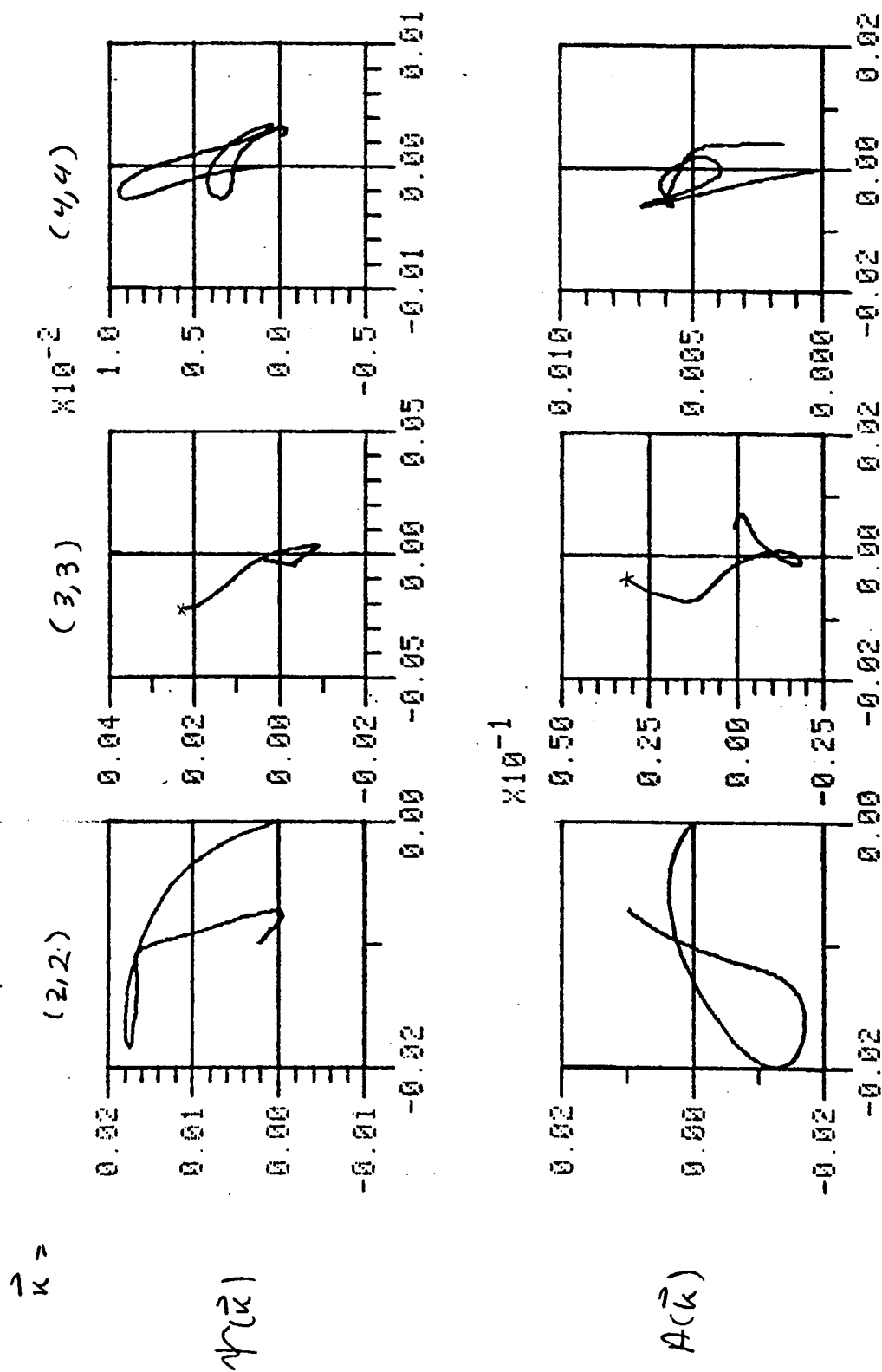


Figure 31.- Modal trajectories for run A9 ( $B_0 = 0$ ,  $\mu = \nu = .01$ ) for  $\vec{k} = (2,2), (3,3), (4,4)$ .



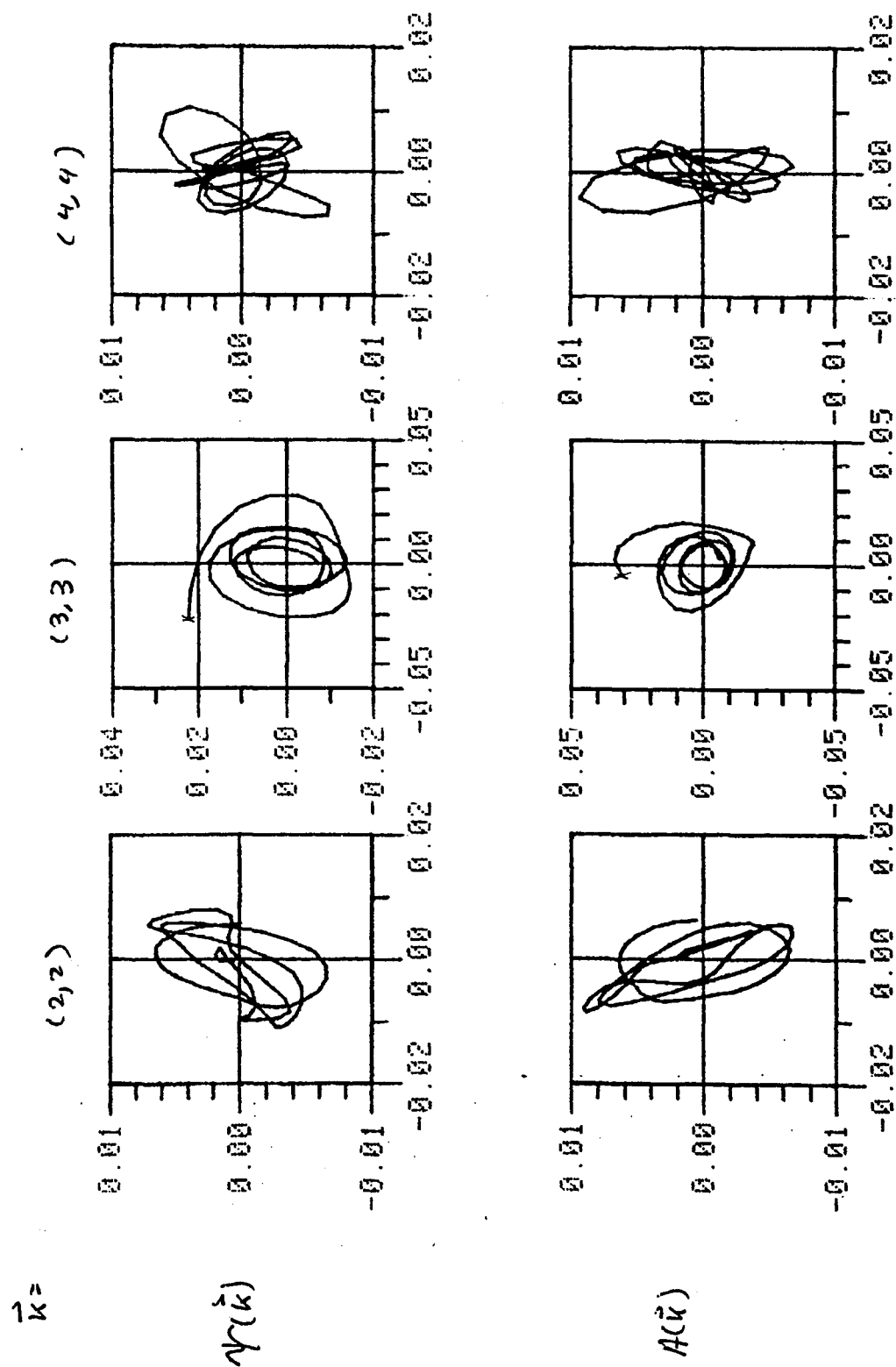


Figure 32.- Modal trajectories for run A15 ( $B_0 = 2$ ,  $\mu = \nu = .01$ ) for  $\vec{k} = (2,2)$ ,  $(3,3)$ ,  $(4,4)$ .

over the last 11520 time steps, i.e., the last 90% of the corresponding inviscid runs). The spikes may also have another origin, which we will now comment on.

In addition to recording the time averages of the directionally averaged magnetic and kinetic energy spectra (Figures 9 through 12), the means and standard deviations of all the individual complex modes  $j(\vec{k}) = k^2 a(\vec{k})$  and  $\omega(\vec{k}) = k^2 \chi(\vec{k})$  were also determined over the same time (the last 11520 time steps). In Figures 33 and 34, the relative magnitudes of the means and standard deviations of the modes associated with run A1 are presented in terms of ersatz three-dimensional plots. In Figure 33 the averages of  $\omega(\vec{k})$  and  $j(\vec{k})$  are represented by the magnitudes  $|\overline{\omega(\vec{k})}|^2 = |\overline{\omega(\vec{k})}|^2/k^2$  and  $|\overline{B(\vec{k})}|^2 = |\overline{j(\vec{k})}|^2/k^2$ , respectively. The standard deviations for run A1 are similarly represented in Figure 34. The means and standard deviations of run A2 ( $B_0 = 1$ ) are similarly shown in Figures 35 and 36. (In these figures, the empty mode (0,0) appears in the center of the plot, and the other modes can be found by counting the characters from this location: positive to the right and up, negative to the left and down. The characters are symmetric upon reflection through (0,0) since  $|j(\vec{k})| = |j(-\vec{k})|$ , etc.)

Several observations can be drawn from these figures. First, there is a strong correlation between the spikes in Figures 9 through 12 and the largest relative means in Figures 33 and 35. (The correspondence is: Figure 9 to Figure 33a, Figure 10 to Figure 33b, Figure 11 to Figure 35a and Figure 12 to 35b.) The specific values of some of these means and standard deviations are given in Table 5.

## FOURIER COEFFICIENT MAGNITUDES

INTENSITY LEVELS 1, ..., 16 : " .:-+==!&gt;%\$[OIO#@"

&lt;V(Kx,Ky)\*\*2&gt;

TIME= 0.115E+05

&lt;B(Kx,Ky)\*\*2&gt;



Figure 33.- Relative magnitude of mean values of modal coefficients for run A1 ( $B_0 = 0$ ,  $\mu = \nu = 0$ ).







Table 5. Comparison of means and standard deviations for some modes of runs A1 and A2, computed for last 11520 time steps. [Format: (mean  $\pm$  std. dev. of real part, mean  $\pm$  std. dev. of imaginary part)]

	<u>A1 (<math>B_0=0</math>)</u>	<u>A2 (<math>B_0=1</math>)</u>
$\omega(0,1)$	(0.014 $\pm$ .030, 0.005 $\pm$ .028)	(0.032 $\pm$ .004, -.004 $\pm$ .013)
$\omega(0,2)$	(0.006 $\pm$ .040, 0.015 $\pm$ .047)	(-.033 $\pm$ .042, -.003 $\pm$ .033)
$\omega(0,3)$	(0.123 $\pm$ .060, -.115 $\pm$ .107)	(0.134 $\pm$ .102, -.254 $\pm$ .070)
$\omega(0,4)$	(-.154 $\pm$ .113, 0.173 $\pm$ .102)	(-.258 $\pm$ .052, 0.125 $\pm$ .072)
$\omega(0,5)$	(-.248 $\pm$ .120, -.268 $\pm$ .139)	(-.427 $\pm$ .110, -.344 $\pm$ .076)
$\omega(1,0)$	(-.021 $\pm$ .021, -.032 $\pm$ .015)	(-.001 $\pm$ .023, -.003 $\pm$ .034)
$\omega(2,0)$	(0.013 $\pm$ .048, -.008 $\pm$ .052)	(-.001 $\pm$ .065, -.002 $\pm$ .048)
$\omega(3,0)$	(-.029 $\pm$ .076, 0.032 $\pm$ .070)	(0.000 $\pm$ .119, 0.002 $\pm$ .108)
$\omega(4,0)$	(-.028 $\pm$ .119, 0.002 $\pm$ .093)	(0.003 $\pm$ .103, -.003 $\pm$ .098)
$\omega(5,0)$	(-.006 $\pm$ .125, -.054 $\pm$ .130)	(0.009 $\pm$ .130, 0.000 $\pm$ .127)
$j(0,1)$	(-.022 $\pm$ .027, 0.032 $\pm$ .008)	(0.000 $\pm$ .001, 0.001 $\pm$ .002)
$j(0,2)$	(-.009 $\pm$ .061, 0.003 $\pm$ .094)	(-.013 $\pm$ .008, -.010 $\pm$ .006)
$j(0,3)$	(-.009 $\pm$ .085, 0.027 $\pm$ .105)	(-.140 $\pm$ .025, -.321 $\pm$ .021)
$j(0,4)$	(-.005 $\pm$ .106, 0.000 $\pm$ .103)	(-.266 $\pm$ .042, -.375 $\pm$ .051)
$j(0,5)$	(0.019 $\pm$ .133, 0.004 $\pm$ .139)	(-.239 $\pm$ .077, -.145 $\pm$ .060)
$j(1,0)$	(-.064 $\pm$ .034, -.065 $\pm$ .039)	(-.001 $\pm$ .033, -.001 $\pm$ .022)
$j(2,0)$	(-.011 $\pm$ .054, -.002 $\pm$ .088)	(0.001 $\pm$ .048, -.001 $\pm$ .065)
$j(3,0)$	(-.033 $\pm$ .060, 0.055 $\pm$ .102)	(-.001 $\pm$ .107, -.003 $\pm$ .117)
$j(4,0)$	(-.030 $\pm$ .131, -.004 $\pm$ .090)	(0.004 $\pm$ .097, -.004 $\pm$ .105)
$j(5,0)$	(-.015 $\pm$ .131, -.029 $\pm$ .108)	(0.005 $\pm$ .127, 0.001 $\pm$ .134)

Second, if we look at Figures 34 and 36, which represent the standard deviations, or fluctuations of the kinetic and magnetic modes, we see no apparent anisotropy for these inviscid runs. This is true for the run A1 ( $B_0 = 0$ ) as well as A2 ( $B_0 = 1$ ); this lack of anisotropy was also seen in Figure 18, for the inviscid runs B1 and B2.

These spikes and associated relatively large and stable mean values were also seen in numerous other inviscid runs (so that A1 and A2 may be taken as representative of a general type of phenomenon). The question is, where do they come from? One answer is that, perhaps the averaging times have not been long enough. Another is that the system of inviscid MHD modal equations possesses a fixed point, or attractor, about which the system point is orbiting in phase space. A third answer (perhaps related to the second) is connected to the fact that there are several constants of the motion.

In classical statistical mechanics there is only one constant of the motion, the energy, which cannot be transformed away. The system is resigned, effectively, to move about on a single closed surface, a hypersphere, in the phase space. Here, we have one or two additional constants of the motion; each of these prescribes another surface in phase space upon which the system point must move. The regions of phase space upon which the system point can move are determined by the intersection of the surfaces associated with each constant of the motion. It may well turn out that this intersection is composed of a union of disjoint sets; such a union is called "decomposable" by Arnold and Avez (1968) and the system is defined as non-ergodic.



The resolution of these questions is very pertinent to a full understanding of non-dissipative MHD turbulent systems (as well as dissipative systems). This resolution is beyond the scope of the present work, where we must be content with merely calling attention to the phenomena which give rise to these questions. In the future, hopefully, the opportunity will arise to investigate these problems in a more systematic and complete manner.

## REFERENCES

- Arfken, G., Mathematical Methods for Physicists, 2nd ed., Academic, New York, 1972.
- Arnold, V. I., and Avez, A., Ergodic Problems of Classical Mechanics, Benjamin, New York, 1968.
- Atkinson, R. E. and Houtermans, F. G., Z. Phys. 54, 9, 1928.
- Batchelor, G. K., Proc. R. Soc., A201, 406, 1950.
- Bennett, W. H., Phys. Rev. 45, 890, 1934.
- Bickerton, R. J., and Keen, B. E., "Plasma production, heating and confinement in fusion devices", in Plasma Physics, B. E. Keen, The Institute of Physics, London, 1974.
- Chandrasekhar, S., Proc. R. Soc. A204, 435, 1951a.
- Chandrasekhar, S., Proc. R. Soc. A207, 306, 1951b.
- Cowling, T. U., Magnetohydrodynamics, Interscience, NY, 1957.
- Edwards, S. F., Plasma Physics, I.A.E.A., STI/PUB/89, Vienna, 1964.
- Edwards, S. F., J. Fluid Mech., 18, 239, 1965.
- Fyfe, D. and Montgomery, D., J. Plasma Phys. 16, 181, 1976.
- Fyfe, D., Joyce, G. and Montgomery, D., J. Plasma Phys. 17, 317, 1977a.
- Fyfe, D., Montgomery, D. and Joyce, G., J. Plasma Phys. 17, 369, 1977b.
- Herring, J. R., Phys. Fluids, 8, 2219, 1964.
- Kadomstev, B. B., Plasma Turbulence, Academic Press, New York, 1965.
- Khinchin, A. E., Mathematical Foundations of Statistical Mechanics, p. 138, Dover, New York, 1949.

- Kovasznyay, L. S. G., Rev. Mod. Phys. 32, 815, 1960.
- Kraichnan, R. H., J. Fluid Mech. 5, 497, 1947.
- Kraichnan, R. H., Phys. Rev. 109, 1409, 1958.
- Kraichnan, R. H., Phys. Fluids 7, 1030, 1964a.
- Kraichnan, R. H., Phys. Fluids 7, 1048, 1964b.
- Kraichnan, R. H., Phys. Fluids 7, 1163, 1964c.
- Kraichnan, R. H., Phys. Fluids 8, 1385, 1965.
- Kraichnan, R. H., Phys. Fluids 9, 1728, 1966.
- Kraichnan, R. H., J. Fluid Mech., 47, 513, 1971a.
- Kraichnan, R. H., J. Fluid Mech., 47, 525, 1971b.
- Kraichnan, R. H., J. Fluid Mech., 56, 287, 1972.
- Kraichnan, R. H. and Montgomery, D., Rept. Prog. Phys. 43, 547, 1980.
- Langmuir, I., Proc. Natl. Acad. Sci., 14, 627, 1928.
- Lehnert, B., Q. Appl. Math., 12, 321, 1955.
- Leslie, D. C., Developments in the Theory of Turbulence (Oxford: Clarendon Press) 1973.
- Lundquist, S., Ark. Phys. 5, 338, 1952.
- Matthaeus, W. H. and Montgomery, D., Ann. N. Y. Acad. Sci., 357, 203, 1980, [Proc. Int. Conf. on Nonlinear Dynamics].
- Matthaeus, W. H. and Montgomery, D., J. Plasma Phys. 25, 11, 1981.
- Matthaeus, W. H. and Goldstein, M. L., J. Geophys. Res. 87, 6011, 1982.
- Moffatt, H.K., J. Fluid Mech., 11, 625, 1961.
- Montgomery, D., 1982 "Major Disruptions, Inverse Cascades, and the Strauss Equations", to appear in Physica Scripta [Proc. Int. Conf. on Plasma Physics, Göteborg, 1982].

- Nihoul, J. C. J., J. Mech., 2, 251, 1963.
- Nihoul, J. C. J., Physica, 31, 141, 1965.
- Orszag, S. A., Stud. Appl. Math. 50, 293, 1971.
- Orszag, S. A. and Tang, C.-M., J. Fluid Mech. 90, 129, 1979
- Patterson, G. S. and Orszag, S. A., Phys. Fluids 14, 2538, 1971.
- Plumpton, C. and Ferrarro, V. C. A., An Introduction to Magnetofluid Mechanics, Clarendon Press, Oxford, 1966.
- Pouquet, A., J. Fluid Mech. 88, 1, 1978.
- Robinson, D. C. Rusbridge, M. G., and Saunders, P. A. H., Plasma Phys. 10, 1005, 1968.
- Robinson, D. C. and Rusbridge, M. G., Phys. Fluids 14, 2499, 1971.
- Rusbridge, M. G., Plasma Phys. 11, 35, 1969.
- Strauss, H. R., Phys. Fluids 19, 134, 1976.
- Tatsumi, T., Rev. Mod. Phys., 32, 809, 1960.
- Thompson, W. B., An Introduction to Plasma Physics, Pergamon, London 1962.
- Tonks, L. and Langmuir, I., Phys. Rev. 33, 195, 1927.
- Tonks, L., Phys. Rev. 56, 360, 1939.
- Watson, C. J. H., "Introduction to Plasma Physics", in Plasma Physics, B. E. Keen, ed., The Institute of Physics, London 1974.
- Zweben, S. J., Menyuk, C. P., and Taylor, R. J., Phys. Rev. Lett. 42, 1270, 1979.
- Zweben, S. J. and Taylor, R. J., Nucl. Fusion 21, 193, 1981.